Improved catalytic performances for abatement of NO_x and PM from lean-burn engines

Kiyoshi Yamazaki

2017

Preface

Lean-burn engines, including diesel and lean-burn gasoline engines, have higher fuel economy, higher torque outputs and lower carbon dioxide (CO_2) emissions, compared to stoichiometric gasoline engines. On the other hand, they have some disadvantages, such as nitrogen oxides (NO_x ; NO + NO_2) and particulate matter (PM ; mainly soot) emissions. Since NO_x and PM emissions from the lean-burn engines are generally in the relationship of 'trade-off', the severity of new emission regulations requires solutions based on combination of engine control method to reduce one component and after-treatment technology to abate the other.

This thesis presents design concepts to improve the catalytic performances of the NSR catalyst and the PM oxidation catalyst for abatement of NO_x and PM from lean-burn engines.

The present studies were conducted in Toyota Central R&D Labs., Inc. (TCRDL) during 1992–2013. In this period the author worked on research and development of automotive catalysts, especially NO_x storage-reduction catalysts for gasoline lean-burn engines and diesel engines, PM oxidation catalysts and diesel oxidation catalysts.

The author is grateful to his supervisors, Dr. Haruo Doi, Dr. Masahiro Sugiura, Mr. Kouji Yokota, Mr. Hideo Sobukawa, Dr. Hirofumi Shinjoh, Dr. Naoki Takahashi, Dr. Toshitaka Tanabe, Mr. Takashi Kuzuya, the heads of catalyst laboratory at TCRDL for giving opportunity to work in the field of catalyst research. The author gives special gratitude to Dr. Toshiyuki Tanaka, who is the present head of the Sustainable Energy & Environment department, for his valuable discussions and encouragements to complete these studies.

The author thanks to his co-researchers of Mr. Seiji Okawara in Toyota Motor Corporation and Mr. Shigeki Daido in NIPPON SOKEN. The author also thanks to his co-researchers and great friends of Mr. Tadashi Suzuki, Mr. Tomoyuki Kayama, Dr. Fei Dong, Mr. Yuji Sakakibara and Dr. Yoshiyuki Sakamoto in TCRDL.

The author is deeply grateful to Prof. Atsushi Satsuma for the comments and clarifications regarding his present thesis. The author is also grateful to Prof. Takahiro Seki, Prof. Masahiro Hirasawa, Prof. Masakuni Ozawa and Prof. Kyoichi Sawabe for reviewing this thesis.

Finally, the author is extremely grateful to his father and mother for very kind and great supports for his life. The author gives heartfelt thanks to his loving wife Naomi for her very warmest help and his son Takuto, daughter Anju for their warm encouragements to complete this thesis.

2017
Aichi
Kiyoshi Yamazaki

Contents

Chapter 1
General Introduction

1. Background

Since its invention at the end of 19th century, the automobile with internal combustion engine (ICE) has become essential to our life and has greatly contributed to the development of industry and economy on an extensive scale in developed countries. In addition, the use of automobiles continues to spread rapidly throughout the world, especially in developing countries. Such popularization of the automobile, however, has some negative impacts; casualties in traffic accidents, air pollutions by harmful emissions in its exhaust and huge consumptions of petroleum. Recently carbon dioxide (CO_2) in its exhaust is also discussed widely as a greenhouse gas causing global warming. Research object of this thesis is catalytic technology for abatement of emissions which are harmful to human body. In this thesis, “emissions” is regarded as the substances in automotive exhaust which are harmful to human body and CO_2 is not dealed with as automotive emission.

The ICE is a heat engine where the combustion of a fuel occurs with an oxidizer (usually air) in a combustion chamber. The ICE mainly used for the automobile can be classified by fuel, ignition system, air to fuel (A/F) ratio introduced into the combustion chamber, and fuel injection method, as shown in Table 1. The A/F is generally determined in weight. The combustion of a fuel is an oxidation reaction of hydrocarbons with oxygen (O_2) to CO_2 and water (H_2O);

$$C_nH_m + (2n+m)O_2 \rightarrow nCO_2 + (m/2)H_2O$$

A/F ratio of 14.6 is a stoichiometric condition of this reaction. At this condition all fuel should be oxidized to CO_2 and H_2O, however, the combustion reaction in the ICE is not perfect. This imperfection brings about emissions of carbon oxide (CO) and unburned hydrocarbons (HC) from the ICE. Moreover, the combustion reaction elevates the temperature of the combustion chamber above 1700 ºC. This high temperature gives rise to emission of nitrogen oxides (NO_x: NO and NO_2) through some reactions between nitrogen (N_2) and O_2 in air as below;

$$N_2 + O_2 \rightarrow 2NO$$

$$2NO + O_2 \rightarrow 2NO_2$$

In the case of the ICE with fuel direct injection, the combustion of air-fuel mixture is heterogeneous in nature and then particulate matter (PM; mainly soot) is generated in fuel rich zone of diffusion flame in the chamber. Therefore, main emissions from the

ICE are NO_x, CO, HC and PM, which are harmful to human being.

Table 1. Classification of internal combustion engines.

Engine	Fuel	Ignition system	A/F ratio	Fuel injection method
Gasoline (normal gasoline)	gasoline	spark-ignition	14.6 (near-stoichiometry)	port injection
				diect injection
Gasoline lean-burn			mainly > 14.6 (fuel lean)	port injection
				diect injection
Diesel	diesel	compression-ignition	mainly > 14.6 (fuel lean)	diect injection

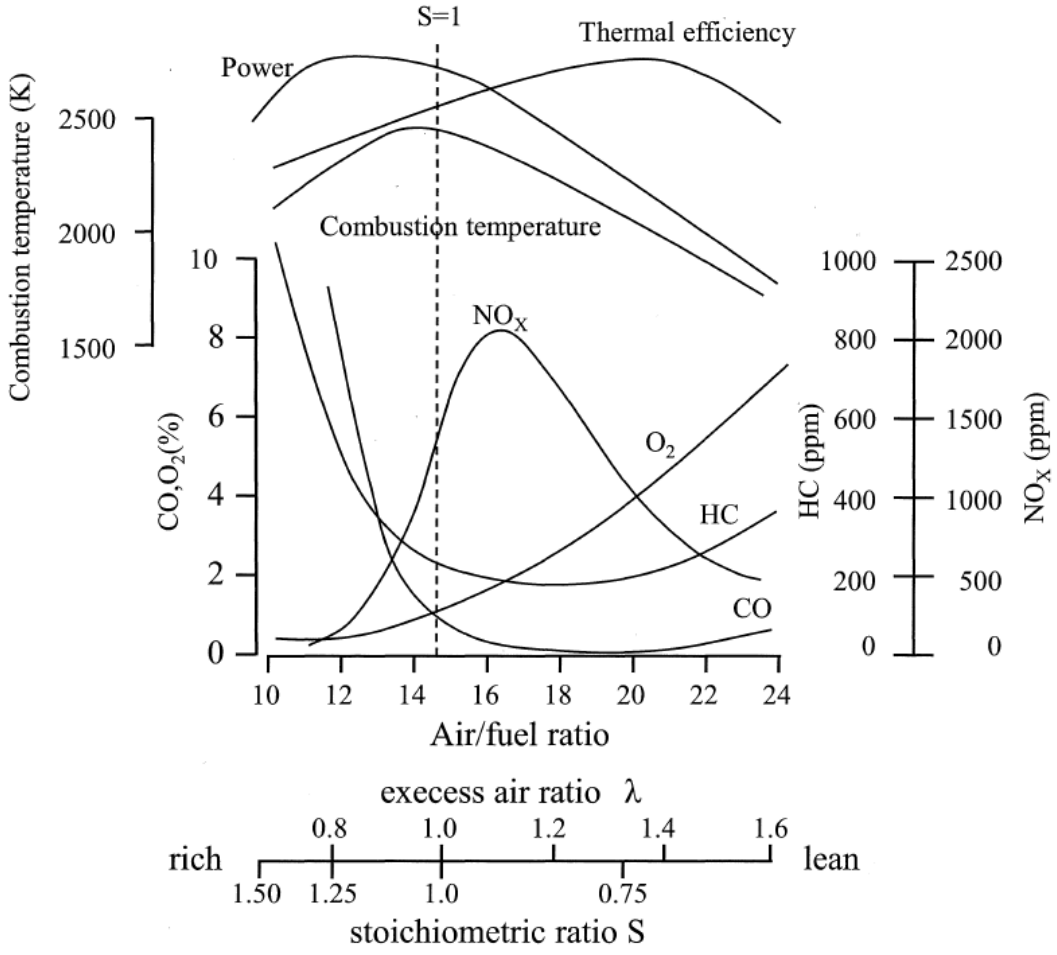

Fig. 1. Influence of Air/fuel (A/F) ratio on engine emissions and performance [1].

Fig. 1 shows the relationship between the A/F ratio and the concentrations of NO_x, CO and HC in exhaust from an ICE, in which it is seen that each substance is affected independently by the A/F ratio [1]. At fuel rich conditions (A/F lower than 14.6), CO and HC emissions are high due to a lack of oxygen. At fuel lean conditions (A/F higher than 14.6), CO and HC concentrations are low because of sufficient amount of the oxygen during the combustion. NO_x concentration reach a maximum at A/F = 16 before decreasing at very lean conditions. In addition, O_2 concentration in the exhaust increases gradually with the increase in A/F ratio.

Air pollution became a serious problem during the 1960s in large cities such as Los Angeles in the USA and Tokyo in Japan. There were some causes for the air pollution, such as emissions from stationary sources including electrical power plants, chemical plants and steel plants, and emissions from mobile sources including automobiles, trains, air planes and ships. Especially in Los Angeles, the emissions from automobiles were the primary causes. This situation caused the most severe California emission standard of automobile in the world. With growing need of emission control technology of automobiles in 1960s, the US Congress passed 1970 Clean Air Act. The Act required 90% reduction of CO and HC emissions of 1970 model year levels by 1975, and a 90% reduction of NO_x emissions of 1971 model year levels by 1976. In Japan, an emission control standard was introduced in 1978, which was similar to that of California. Emission standards in the USA and Japan are shown in Table 2 and 3, respectively. In 1992, the European Community passed strict legislation for passenger's car. Emission standard in Europe is shown in Table 4.

It was a very difficult problem to satisfy the emission standards in 1970s. A lot of technologies, such as improving combustion, exhaust gas recirculation (EGR), catalytic abatement of emissions, were carried out to resolve this problem. After struggling in research and development, 'three-way catalyst (TWC) system' was developed by utilizing both catalytic technology and electronic control technology [2–4], which was a breakthrough for abatement of emissions in automotive exhaust. The TWC is platinum (Pt), palladium (Pd), rhodium (Rh) supported catalyst on metal oxide supports. Pt and Pd are active components for CO and HC oxidation. Rh is an active component for NO_x reduction. Alumina (Al_2O_3) with high surface area is used as a typical support. As for catalyst form, monolithic catalysts are commonly used although pelletized catalysts are used in the early stage of commercialization.

Table 2. Passenger's car emission standard in the U.S.

year	Area, Category, Diesel(D) / Gasoline(G)	Level (g/mile)				Test
		CO	HC	NO_x	PM	
1970	Federal & California	23	2.2	–	–	7mode
1972	California	39	3.4	3.2	–	FTP-72
	Federal	39	3.4	–	–	
1975	California	9.0	0.9	2.0	–	
	Federal	15	1.5	2.0	–	
1977	California	9.0	0.41	1.5	–	
	Federal	15	1.5	2.0	–	
1980	California	8.0	0.39	1.0	–	
	Federal	7.0	0.41	2.0	–	
1981	Federal & California	3.4	0.41	1.0	–	
1993	California	3.7	0.26	0.4	–	
	Federal	7.0	0.41	1.0	–	
1994	California Tier 1	3.4	0.125	0.4	–	
	Federal Tier 1, D	3.4	0.25	1.0	0.08	
	Federal Tier 1, G	3.4	0.25	0.4	–	
1997	California 25% of the fleet	3.4	0.075	0.2	–	
	2% of the fleet	1.7	0.040	0.2	–	FTP-75
2004	California TLEV	3.4	0.125	0.40	0.08	
	California LEV	3.4	0.075	0.05	0.01	
	Federal Tier 2 bin 9, D	3.4	0.125	0.40	0.08	
	Federal Tier 2 bin 9, G	3.4	0.075	0.20	0.06	
2005	California LEV	3.4	0.075	0.40	0.08	
	California ULEV	1.7	0.040	0.05	0.01	
2006	California ULEV	1.7	0.040	0.20	0.04	
	California SULEV	1.0	0.010	0.02	0.01	
2009	Federal Tier 2 bin 5, D	3.4	0.075	0.05	0.01	
	Federal Tier 2 bin 5, G	3.4	0.075	0.05	0.01	
2016	California ULEV70	1.7	0.070		0.01	
	California SULEV30	1.0	0.030		0.01	
2017	Federal Tier 3	1.0	0.086		0.003	

Table 3. Passenger's car emission standard in Japan.

year	Diesel (D) / Gasoline, Vehicle Weight	Level (g/km); mean (max) CO	HC	NO_x	PM	Test
1978	Gasoline	2.1 (2.7)	0.25 (0.39)	0.60 (0.84)	–	10 mode
1986	D, < 1250 kg	2.1 (2.7)	0.40 (0.62)	0.70 (0.98)	–	10-15 mode
	D, > 1250 kg	2.1 (2.7)	0.40 (0.62)	0.90 (1.26)	–	
1990	D, < 1250 kg	2.1 (2.7)	0.40 (0.62)	0.50 (0.72)	–	
1991	Gasoline	2.1 (2.7)	0.25 (0.39)	0.25 (0.48)	–	
1992	D, > 1250 kg	2.1 (2.7)	0.40 (0.62)	0.60 (0.84)	–	
1994	D, < 1250 kg	2.1 (2.7)	0.40 (0.62)	0.50 (0.72)	0.20 (0.34)	
	D, > 1250 kg	2.1 (2.7)	0.40 (0.62)	0.60 (0.84)	0.20 (0.34)	
1997	D, < 1250 kg	2.1 (2.7)	0.40 (0.62)	0.40 (0.55)	0.08 (0.14)	
1998	D, > 1250 kg	2.1 (2.7)	0.40 (0.62)	0.40 (0.55)	0.08 (0.14)	
2002	D, < 1250 kg	0.63	0.12	0.28	0.052	
	D, > 1250 kg	0.63	0.12	0.30	0.056	
	Gasoline	0.37 (1.27)	0.08 (0.17)	0.08 (0.17)	0.005	
2005	D, < 1250 kg	0.63	0.024	0.14	0.013	JC08
	D, > 1250 kg	0.63	0.024	0.15	0.014	
2009	Diesel	0.63	0.024	0.08	0.005	
	Gasoline	1.15	0.05	0.05	0.005	
2018	Diesel	0.63	0.024	0.15	0.005	WLTP
	Gasoline	1.15	0.10	0.05	0.005	

Table 4. Passenger's car emission standard in European community.

Stage	year	Diesel / Gasoline	Level (g/km) CO	HC	HC + NO_x	NO_x	PM	(#/km) PN
Euro 1	1992	Diesel	2.72	–	0.97	–	0.14	–
		Gasoline	2.72	–	0.97	–	–	–
Euro 2	1996	Diesel IDI	1.0	–	0.70	–	0.08	–
		Diesel DI	1.0	–	0.90	–	0.10	–
		Gasoline	2.2	–	0.50	–	–	–
Euro 3	2000	Diesel	0.6	–	0.56	0.50	0.05	–
		Gasoline	2.3	0.20	–	0.15	–	–
Euro 4	2005	Diesel	0.5	–	0.30	0.25	0.025	–
		Gasoline	1.0	0.10	–	0.08	–	–
Euro 5	2009	Diesel	0.5	–	0.23	0.18	0.005	–
		Gasoline	1.0	0.10	–	0.06	0.005	–
Euro 5b	2011	Diesel	0.5	–	0.23	0.18	0.005	6.0×10^{11}
Euro 6	2014	Diesel	0.5	–	0.17	0.08	0.005	6.0×10^{11}
		Gasoline	1.0	0.10	–	0.06	0.005	6.0×10^{11}

The TWC system can purify NO_x, CO and HC in exhaust from the ICE simultaneously to N_2, CO_2 and H_2O at the stoichiometric or near-stoichiometric condition where CO and HC act as reducing gases and react with NO_x and O_2 as oxidizing gases. Typical conversion behaviors are shown in Fig. 2. CO and HC conversions are high in the fuel lean conditions and NO_x conversion is the high in fuel rich conditions. At exact stoichiometric condition, all NO_x, CO and HC conversions are high concurrently. Since the exact stoichiometric condition cannot be achieved technically in actual automobile implementation, the A/F ratio is controlled within so called "A/F window" to obtain sufficient NO_x, CO and HC conversions. Up to the present, many researchers have attempted to improve the TWC system by modifying the catalyst as well as by using oxygen storage-release materials and supports with higher thermal resistance.

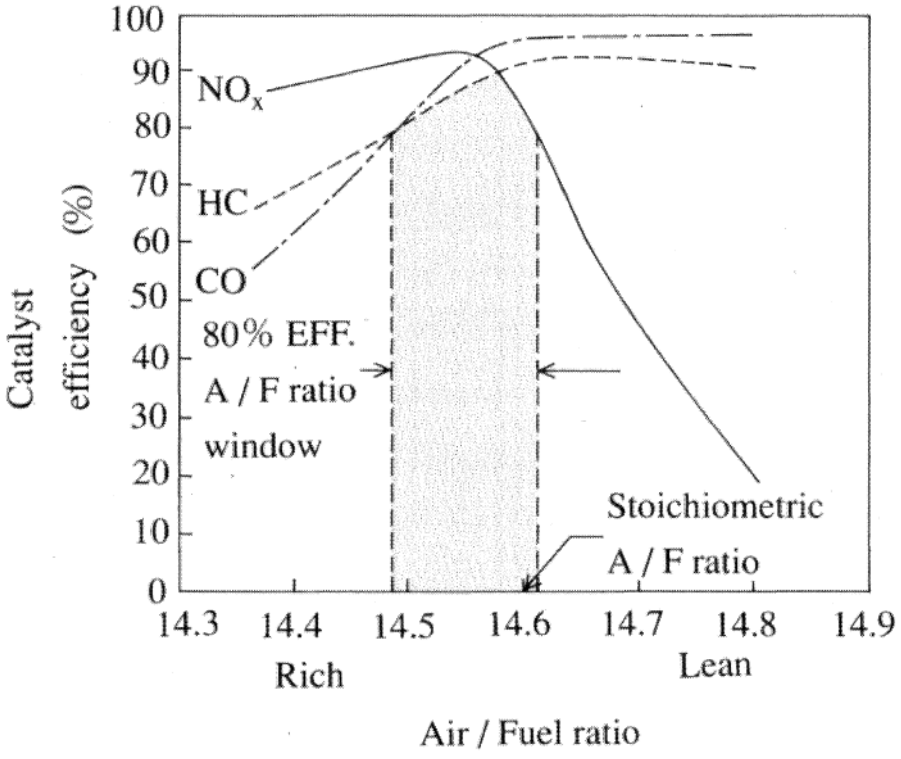

Fig. 2. NO_x, CO and HC conversion efficiencies as a function of Air/Fuel ratio [5].

Lean-burn engines, including diesel engines and lean-burn gasoline engines (Table 1), have higher thermal efficiency, higher torque outputs in a range of low speed rotation, and lower CO_2 emission, compared to stoichiometric gasoline engines with TWC system. Thermal efficiency reaches a maximum around A/F = 21, as shown in Fig.

1, and has increased by 20-25 % compared to that at A/F = 14.6 (stoichiometry). In addition, diesel engines have higher durability and reliability relative to gasoline engines and hence increased their share in the world automotive market as 'environmentally friendly engines'. On the other hand, Lean-burn engines have some disadvantages, such as NO_x and PM emissions. Lean-burning can reduce generation of NO_x, but due to excessive O_2, cannot achieve high NO_x conversion efficiency with TWC, which is known to exhibit non-selective catalytic reduction. PM generation is caused by direct fuel injection into the combustion chamber. This injection method, however, is an essential technology for combustion of lean air-fuel mixture. NO_x and PM emissions from the lean-burn engines are generally in the relationship of 'trade-off', in which PM burn-up is favored by high combustion temperatures, however, high combustion temperatures also favor the generation of NO_x in the engine cylinder, as shown in Fig. 3 [6, 7]. Therefore, the severity of new emission standard requires solutions based on combination of engine control method to reduce one component and after-treatment technology to abate the other. The purpose of this thesis is catalytic abatement of NO_x and PM respectively from lean-burn engines.

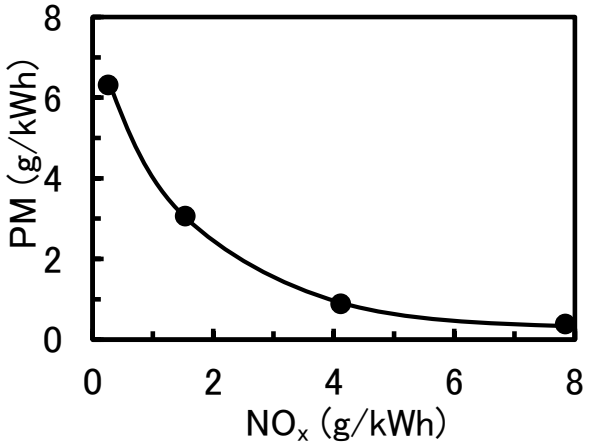

Fig. 3. Relationship between NO_x emission and PM emission during EGR [6].

2. Challenges of catalytic abatement of NO_x and PM from lean-burn engines

Significant efforts, such as exhaust gas recirculation (EGR), common rail type fuel injection system, turbo charger with inter-cooler, and modified combustion chamber shape, have been directed towards improving diesel and gasoline lean-burn engine systems to reduce NO_x and PM emissions. However, to achieve further reduction to meet emission standards which gets stricter year after year, advanced catalytic

technologies need to be adopted and therefore various catalyst systems are currently undergoing research and development to allow their practical application.

The catalyst or catalyst system for abatement of NO_x from lean-burn engines can be roughly divided into two groups: NO_x selective catalytic reduction (SCR) catalyst and NO_x storage-reduction (NSR) catalyst.

SCR systems have been actively researched since the discovery of NO direct decomposition over copper ion-exchanged ZSM-5 type zeolite by Iwamoto et al. [8]. From the early 1990s on, several types of catalyst systems have been explored as components of SCR systems using HC as a reducing gas [9–12]. These are composed of various metals, including the base metals and noble metals with support oxides such as zeolites and alumina. H_2, CO and NH_3 can be also used as reducing agents for SCR systems. In this SCR system, the reducing agent used to remove NO_x is supplied from gases normally present in the engine exhaust. SCR catalysts equipped with reducing agent dosing systems such as fuel injection and urea addition have also been developed for abatement of variable NO_x emissions. Although SCR systems using HC gases have an advantage through a perspective of space utilization, there are some problems with this approach, including the low activity of base metal catalysts at low temperatures and subgeneration of nitrous oxide (N_2O) when using noble metal catalysts such as Pt. Therefore, further improvements are demanded before such systems is put to practical applications.

At the moment, the most promising technology with SCR system is the urea-dosing SCR process applied primarily to large vehicles. In this system, ammonia generated by the decomposition of urea is introduced in front of a SCR catalyst such as Cu ion-exchanged zeolites. This method is based on the ammonia SCR system commonly used as denitrification plant in boilers within thermal power stations and first put into practical use in the 1970s. The urea SCR system can respond to changing NO_x emissions by controlling the dosing of urea to maintain the optimal NH_3 to NO_x ratio. However, several issues still need to be resolved, such as improving activity at low temperatures at which urea cannot be decomposed, suppression of NH_3 passing unreacted through the catalyst, improving thermal durability, optimizing the space required for the onboard urea tank and urea dosing unit, and refilling of the urea tank by each user. In order to improve activity at low temperatures of the urea-dosing SCR systems, it is needed to investigate the way to enhance the decomposition of urea to NH_3, the oxidation of NO to NO_2 and the decomposition of intermediates such as NH_4NO_3.

The NO_x storage-reduction catalyst (NSR catalyst) system is another practical

method for NO_x removal under excess oxygen conditions and is probably the most promising method for NO_x abatement from lean-burn engines especially in passenger automobiles. Many studies have been conducted for the purpose of improving this technology since it was initially developed and put into practical use by Toyota in 1994 [13,14]. The NSR catalyst consists of NO_x storage components based on alkaline earth or alkaline metal oxides, notably barium oxide (BaO), and precious metals, mainly Pt, dispersed on support materials, generally Al_2O_3. Its NO_x purification mechanism is, as shown in Fig. 4, to store NO_x under oxidizing conditions after which it is regenerated under reducing conditions, where NO_x is released and subsequently reduced with HC, CO and hydrogen (H_2) to form N_2, H_2O and CO_2.

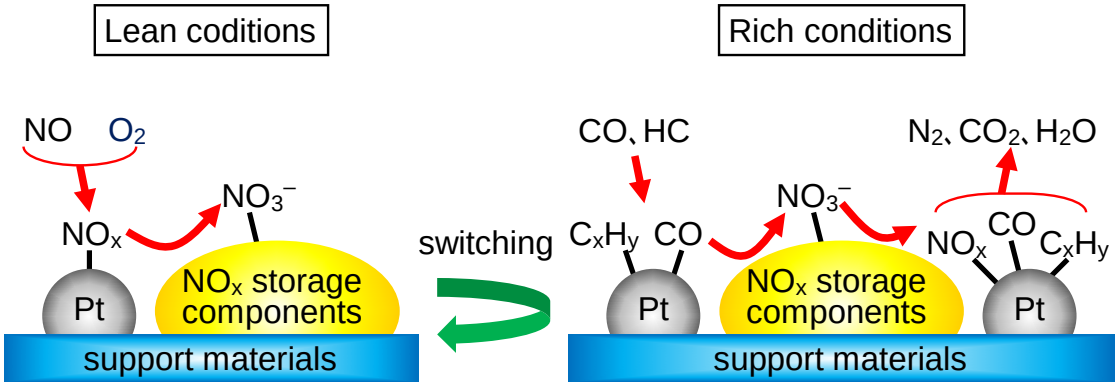

Fig. 4. NO_x storage and reduction mechanism of NSR catalysts.

The biggest issue with the NSR catalyst is the deactivation problem. There are two factors in the deactivation of the NSR catalyst, i.e., sulfur poisoning and thermal deterioration. The sulfur poisoning is caused by sulfate formation of NO_x storage components due to the reaction with sulfur dioxide (SO_2) in the exhaust gas, as shown in Fig. 5, and seems to be the most difficult problem to solve for the NSR catalyst. SO_2 is derived from the combustion of sulfur compounds in fuel. Sulfur content of fuel that strongly affects such a sulfur deactivation is decreasing in developed countries by the recent regulations for both gasoline and diesel fuels [15]. For example, in EU countries, USA and Japan, low level sulfur content under 10 ppm has already achieved since 2009. However, sulfur content in developing countries is still higher level, which is beyond 600 ppm. For the sulfur-poisoned NSR catalyst, a desulfation treatment for sulfate decomposition and sulfur desorption at high temperatures above 600 °C under rich conditions is necessary to recover the NSR activity periodically (Fig. 5). The desulfation

procedure, however, gives rise to thermal deactivation as well as a fuel penalty in cases where it is carried out at high temperature for long time periods. Accordingly, a method for the efficient regeneration of sulfur-poisoned NSR catalysts is needed to improve the performance of the NSR catalyst.

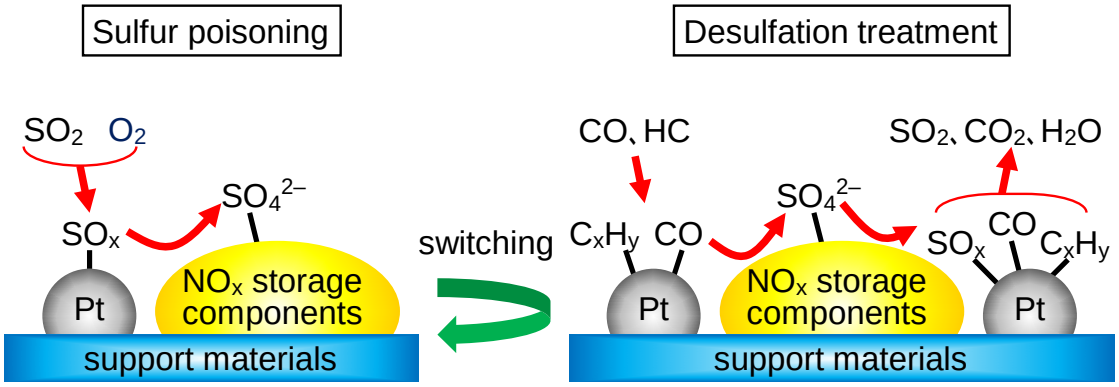

Fig. 5. Mechanisms for sulfur poisoning and dusulfation of NSR catalysts.

The temperature of the exhaust gas from lean-burn engines generally reaches around 850 ºC, although it is lower than that from stoichiometric gasoline engines. Thermal deterioration seems to result from the reaction of NO_x storage components with the support materials and a particle growth of precious metals and NO_x storage components at approximately 850 ºC. The particle growth of precious metals leads to a decrease in the number of surface precious metal sites. Smaller number of precious metal site can enhance a poisoning of reactants (CO and/or HC) onto the precious metals under rich conditions, which brings on a reaction inhibition. Therefore, a method for the suppression of reaction inhibition by reactant poisoning is required as well as for the suppression of particle growth to improve the performance of the NSR catalyst.

The most effective and widely applied after-treatment technology for PM abatement is based on the diesel particulate filter (DPF) or the gasoline particulate filter (GPF). PM trapped in a DPF or GPF must be periodically removed by combustion, due to unacceptable back pressure levels in the gas exhaust line. The direct oxidation of PM over the un-catalyzed DPF or GPF requires high temperatures over 600 °C, and is often carried out by injecting fuel into the exhaust. This strategy incurs additional fuel consumption, requires a complex means of control, and can create significant thermal stress for the DPF or GPF and the other after-treatment devices (i.e., the de-NOx

catalysts). Then, use of catalyzed diesel particulate filter (C-DPF) or catalyzed gasoline particulate filter (C-GPF) is regarded as the most promising solution to reduce PM emissions from lean-burn engines. PM is trapped on the filter and oxidized with a PM oxidation catalyst at lower temperatures.

However, large soot particles are immobile and barely penetrate into the catalyst micropores or mesopores, and thus catalytic soot oxidation is quite slow [16]. Moreover, The nature the 'contact' between PM and catalyst particles has a very strong influence on catalytic performance for PM oxidation. Previous study has revealed that the contact condition in the C-DPFs or C-GPFs is similar to 'loose contact', which was obtained by mixing catalyst and PM powders with a spatula, as distinct from 'tight contact' obtained by mixing them with a mechanical mill or an agate mortar [16]. One of the biggest problem with the C-DPF or G-DPF is the poor contact between the external catalyst surface and the soot particles. Thus, the PM oxidation catalyst used for the filters need to exhibit high catalytic performance even in loose contact mode as well as that in the tight contact mode. To overcome this problem with contact, many catalysts and technologies based on different principles have been proposed. Using gas-phase NO_2 in the application of so-called continuously regeneration trap (CRT) technology causes a decrease in the soot oxidation temperature [17]. NO_2 is generated from the oxidation of NO over a platinum catalyst and functions as a mobile species for soot oxidation by creating catalyst-soot contact; however, a new trend in diesel engines to decrease NO_x emission could impose significant restrictions on the application of CRT technology. Organometallic fuel additives, also known as fuel-borne catalysts (FBCs), lead to the formation of catalyst-doped soot during combustion in the engine, which lowers the soot oxidation temperature in the DPF [18]; however, the continuous consumption of FBCs and the accumulation of metal oxide as an ash inside the DPF restrict their application strongly. A large number of molten salt catalysts, which can wet the soot surface as a mobile catalyst and therefore decrease the PM oxidation temperature in loose contact mode, have been studied in recent years; the formulations are based on the addition of potassium or cesium to transition metal (such as Cu, V, Mo, Co or Fe) oxides [19,20]. However, these catalysts have drawbacks in some practical applications that are related to either thermal degradation or selective leaching in condensed water during the soot oxidation process [21].

Another biggest problem with the C-DPF or G-DPF is the ash deposition onto catalysts coated on the filter. PM is composed of mainly soot, soluble organic fraction (SOF), sulfates, and slightly inorganic metal materials (ash). Ash generally is generated from lubricant oil additives, engine cleaning detergents, trace metals in diesel fuels,

engine wear metals and corrosion products [16]. Although soot and SOF are oxidized over the catalysts, ash could remain as fine particles during regeneration process. After repetitive regenerations, the ash would deposit as a layer on the filter walls, and subsequent PM would be trapped on the ash layer. As a result, the ash layer form a barrier separating the PM from the catalyst coated on the filter walls. In PM oxidation by O_2 over catalyst, contact between the catalyst and the PM should be necessary, since the reaction processes take place at the three-phase boundary between the two solids and the gaseous O_2. Therefore, even just a thin ash layer may interrupt the contact between the catalyst and the PM, and the catalytic performance for soot oxidation could decrease drastically. Thus, the PM oxidation catalyst used for the C-DPF or G-DPF need to retain catalytic performance against for ash deposition.

As mentioned above, both the NSR catalyst and the PM oxidation catalyst still have challenges to be solved for practical use into lean-burn engines, which are resistance to sulfur poisoning and thermal durability in the NSR catalyst, and catalytic performance in loose contact mode and tolerance for ash deposition in the PM oxidation catalyst, respectively.

3. Objectives and outline of this research

This thesis was conducted to obtain the design concepts to improve the catalytic performances of the NSR catalyst and the PM oxidation catalyst from the viewpoint of 'activation and utilization of oxygen'. It is well known that there are several types of activation of oxygen to generate active oxygen species;

(a) Adsorption of gaseous oxygen onto a metal surface to generate dissociative atomic oxygen species, which is the most oxidative. Onto a metal surface, however, reactants, such as CO and HC, often adsorb more strongly than oxygen, resulting in reaction inhibition. This phenomenon is referred to as 'reactant poisoning'.

(b) Adsorption of gaseous oxygen onto a metal oxide surface to generate adsorbed oxygen species, which transform according to the general scheme [22];

$$O_{2(ads)} \rightarrow O_2^-{}_{(ads)} \rightarrow O_2^{2-}{}_{(ads)} \rightarrow 2O^-{}_{(ads)} \rightarrow 2O^{2-}{}_{(lattice)}$$

(c) Adsorption of gaseous oxygen onto a metal surface supported on a metal oxide to generate mobile active oxygen species, which migrates form metal surface to metal oxide surface and spreads even further on metal oxide. This phenomenon is referred to as 'spillover' [23].

(d) Generation from transition metal oxide through its valence fluctuation.

As for the NSR catalyst, desulfation and NO_x reduction processes on the precious metals under rich conditions can be inhibited by poisoning of reactant, such as CO, HC

or sulfur-compounds, based on the above type (a). Transition metal oxides have the potential to provide the active oxygen species onto precious metals to suppress the poisoning, based on the above type (d). In order to promote desulfation and NO_x reduction over the NSR catalyst, effects of the addition of transition metal oxides to the catalyst on its catalytic performance after sulfur poisoning and thermal aging were studied in chapters 2–4. As for the PM oxidation catalyst, the active oxygen species such as $O_{2(ads)}$, $O_2^-{}_{(ads)}$, $O_2^{2-}{}_{(ads)}$, and $2O^-{}_{(ads)}$ on a metal oxide has the potential to create a contact between catalyst and PM by migrating from catalyst to PM particles, based on the above types (b) and (c). Previous studies reported that active oxygen species on CeO_2 shows exceptional mobility [24] and that silver (Ag) loading onto CeO_2 enhanced the generation of active oxygen species [25]. In order to promote the generation of active oxygen species, effect of the morphology of an innovative CeO_2–Ag catalyst on catalytic performance in loose contact mode was investigated in chapter 5. Moreover, impacts of ash deposition on the catalytic performance for PM oxidation via the CeO_2–Ag catalyst were studied using PM/ash/catalyst multi-layered samples and C-DPFs exposed to actual exhaust gas from diesel engines in chapters 6–7.

This thesis consists of eight chapters. General introduction to NSR catalyst and PM oxidation catalyst in C-DPF or C-GPF for abatement of NO_x and PM from lean-burn engines is discussed in Chapter 1. Following is outline of this thesis.

In chapter 2, effect of the addition of transition metal oxides (MO_x : Fe_2O_3, CoO, NiO, CuO) to a NSR catalyst on the sulfur tolerance was studied. This research reveals that the addition of the iron oxide (Fe_2O_3) improves the NO_x removal activity through storage-reduction (NSR activity) after sulfur poisoning and desulfation treatment. SO_2 temperature-programmed desorption (TPD) measurement indicates that the Fe_2O_3 suppresses a poisoning of C_3H_6 and/or sulfur-compounds onto Pt and consequently promotes desulfation of the sulfur-poisoned NSR catalyst.

In chapter 3, effect of the addition of Fe_2O_3 to a NSR catalyst on the thermal durability at 850 ºC was investigated. This study reveals that the addition of Fe_2O_3 improves the NSR activity after thermal aging at 850 ºC when CO is used as a reducing agent. Kinetic analysis of binary gas (CO–O_2, C_3H_6–O_2, CO–NO) reactions and XRD analysis demonstrates that the Fe_2O_3 weakens the CO self-poisoning onto Pt by provision of active oxygen species from Fe_2O_3 or/and Fe in a Pt–Fe alloy and consequently enhances NO_x reduction under rich conditions.

The NSR catalyst for gasoline lean-burn engines also needs three-way catalytic (TWC) performance, i.e., light-off performance in a feedstream of near-stoichiometric

compositions and conversion efficiencies as a function of the stoichiometric ratio. Chapter 4 shows that the Fe_2O_3 addition to a NSR catalyst also improves the TWC performance after thermal aging at 850 ºC. Oxygen storage-release capacity (OSC) measurement and kinetic analysis of binary gas reaction indicate that the Fe_2O_3 plays two important roles; (a) compensating the fluctuations between rich and lean conditions and (b) weakening CO self-poisoning onto Pt by provision of active oxygen species.

In Chapter 5, an innovative CeO_2–Ag catalyst, which has a unique agglomeration morphology consisting of metallic Ag particles in the center surrounded by fine CeO_2 particles, has been developed. The effect of the morphology of this catalyst on the catalytic performance in loose contact mode was investigated compared with conventional catalysts composed of Ag and/or CeO_2. This study reveals that the CeO_2–Ag catalyst exhibited the highest catalytic performance and the lowest sensitivity to the contact between PM and catalyst particles. Oxygen temperature-programmed desorption (O_2-TPD) and electron spin resonance (ESR) analysis data propose a mechanism for PM oxidation over this catalysts, where the atomic oxygen species on the Ag surface migrate to the CeO_2 surface via the interface, transform into O_2^- species, and then further migrate onto soot particles. The morphology of the CeO_2–Ag catalyst is found to be optimal for the formation of both active oxygen species.

In chapter 6, the effect of the morphology of the CeO_2–Ag catalyst on the tolerance for ash deposition of the PM oxidation catalyst was studied using multi-layered samples, composed of a catalyst, an ash material (Al_2O_3 or $CaSO_4$) and PM particles deposited on a thin cordierite plate in sequence. This research reveals that the CeO_2–Ag catalyst enhances the oxidation of PM particles separated from the catalyst by ash deposition, although a simple CeO_2 catalyst does not. The effectiveness of this remote PM oxidation via the CeO_2–Ag catalyst is found to extend across an ash thickness of more than 50 μm.

Chapter 7 shows the effect of the CeO_2–Ag catalyst on the tolerance for ash deposition using C-DPFs through small-scale evaluation and visualization measurement with actual exhaust gas from diesel engines. This study reveals that the CeO_2–Ag catalyst in the C-DPF promotes the oxidation of PM on the ash layer until the ash reaches 40 g/L in weight or 100μm in thickness. ESR analysis proposes a remote PM oxidation mechanism, in which O_2^- species generated on the catalyst's surface first migrates to the ash surface and then to the PM particles. On the other hand, a conventional Pt/Al_2O_3 catalyst in the C-DPF loses the catalytic performance readily by ash deposition.

Chapter 8 summarizes this thesis and gives the general conclusion.

References

[1] T. Inoue, ISBN978-4-254-23771-9 C3353, Japanese Automotive Standards Organization, p23.

[2] M. Shelef, J. H. Jones, J. T. Kummer, K. Otto, E. E. Weaver, Environ. Sci. Tech. 5 (1971) 790.

[3] J. G. Rivard, SAE, Paper No.730005 (1973).

[4] I. Gorille, N. Rittnannsberger , P Werner, SAE Paper No.750368 (1975).

[5] M. Ozawa, M. Kimura, H. Sobukawa, K. Yokota, Toyota Central R&D Review of Toyota CRDL 27 (1992) 43.

[6] S .S. Gill, J. M. Herreros, A. Tsolakis, D. M. Turner, E. Miller, A. P. E. York, RSC Adv. 2 (2012) 10400.

[7] J. Hussain, K. Palaniradja, N. Algumurthi, R. Manimaran, J. Eng. Res. Stud. 3 (2012) 34.

[8] M. Iwamoto, H. Yahiro, Y. Yu-u, S. Shundo, M. Mizuno, Shokubai (Catalyst) 32 (1990) 430.

[9] S. Sato, Y. Yu-u, H. Yahiro, N. Mizuno, M. Iwamoto, Appl. Catal. 70 (1991) L1.

[10] M. Misono, K. Kondo, Chem. Lett. (1991) 1001.

[11] M. Sasaaki, H. Hamada, Y. Kintaichi, T. Ito, Catal. Lett. 15 (1992) 297.

[12] T. Tanaka, T, Okuhara, M. Misono, Appl. Catal. B 4 (1994) L1.

[13] N. Miyoshi, S. Matsumoto, K. Katoh, T. Tanaka, J. Harada, N. Takahashi, K. Yokota, M. Sugiura, K. Kasahara, SAE Tech. Paper 950809 (1995).

[14] N. Takahashi, H. Shinjoh, T. Iijima, T. Suzuki, K. Yamazaki, K. Yokota, H. Suzuki, N. Miyoshi, S. Matsumoto, T. Tanizawa, T. Tanaka, S. Tateishi, K. Kasahara, Catal. Today 27 (1996) 63.

[15] Japan Automobile Manufacturers Association, Inc., eco_reprt2012, http:www.jama.or.o/wrestle/eco_reort/pdf/eco_report2012_01.pdf.

[16] B.A.A.L. van Setten, M. Makkee, J.A. Moulijn, Catal. Rev. Sci. Eng. 43 (2001) 489.

[17] B.J. Cooper, J.E. Thoss, SAE Paper 890404 (1989).

[18] G. Lepperhoff, H. Luders, P. Barthe, J. Lemaire, SAE Paper 950369 (1995).

[19] J.P.A. Neeft, M. Makkee, J.A. Moulijn, Appl. Catal. B 8 (1996) 57.

[20] G. Saracco, C. Badini, N. Russo, V. Specchia, Appl. Catal. B 21 (1999) 233.

[21] B.A.A.L. van Setten, C.G.M. Spitters, J. Bremmer, A.M.M. Mulders, M. Makkee, J. A. Moulijn, Appl. Catal. B 42 (2003) 337.

[22] A. Bielanski, J. Haber, Catal.–Rev. Sci. Eng., 19 (1979) 1.

[23] W. C. Conner, J. L. Falconer, Chem. Rev. 95 (1995) 759.

[24] D. Martin, D. Duprez, J. Phys. Chem. 100 (1996) 9429.

[25] M. Machida, Y. Murata, K. Kishikawa, D. Zhang, K. Ikeue, Chem. Mater. 20 (2008) 4489.

Chapter 2

Improved resistance to sulfur poisoning of NO_x storage-reduction catalyst

Abstract

The NO_x storage-reduction catalysis under oxidizing conditions in the presence of SO_2 has been investigated on Pt/Ba/Fe/Al_2O_3, Pt/Ba/Co/Al_2O_3, Pt/Ba/Ni/Al_2O_3, and Pt/Ba/Cu/Al_2O_3 catalysts compared with Pt/Ba/Al_2O_3, Pt/Fe/Al_2O_3, Pt/Co/Al_2O_3, Pt/Ni/Al_2O_3, Pt/Cu/Al_2O_3 and Pt/Al_2O_3 catalysts. The NO_x purification activity of Pt/Ba/Fe/Al_2O_3 catalyst was the highest of all the catalysts investigated in this paper after an aging treatment. That of the aged Pt/Ba/Co/Al_2O_3 and Pt/Ba/Ni/Al_2O_3 catalysts was essentially the same as that of the aged Pt/Ba/Al_2O_3 catalyst, while that of the aged Pt/Ba/Cu/Al_2O_3 and Pt/Cu/Al_2O_3 catalysts was substantially lower than the others.

The Fe-compound on the aged Pt/Ba/Fe/Al_2O_3 catalyst has played a role in decreasing the sulfur content on the catalyst after exposure to simulated reducing gas compared with the Pt/Ba/Al_2O_3 catalyst without the Fe-compound. XRD and EDX show that the Fe-compound inhibits the growth in the size of $BaSO_4$ particles formed on the Pt/Ba/Fe/Al_2O_3 catalyst under oxidizing conditions in the presence of SO_2 and promotes the decomposition of $BaSO_4$ and desorption of the sulfur compound under reducing conditions.

Keywords: Lean-burn engine, NO_x storage-reduction catalysis, Sulfur Poisoning, Platinum, Barium, Iron, Cobalt, Nickel, Copper, Alumina

1. Introduction

The lean-burn engine system has been one of the key technologies for suppressing the fuel consumption of vehicles. Accordingly, NO_x purification under oxidizing conditions was a key issue in meeting more stringent regulations, which could be enforced to effectively reduce both the emission of NO_x, CO and hydrocarbons (HCs) in the exhaust and the fuel consumption of vehicles. However, the fuel lean operating conditions have been limited, because the NO_x emitted under oxidizing conditions could not be purified over the conventional 3-way catalysts, because reductants such as CO and HCs preferentially react with excess oxygen.

Many studies have been carried out on many kinds of catalysts for selective catalytic reduction (SCR) of NO_x under oxidizing conditions, e.g., copper

ion-exchanged zeolites (Cu-ZSM-5) [1-3], alumina [4], base metals supported on zeolites [5], and precious metals supported on zeolites [6]. However, these catalysts have many problems for practical use such as low activity, a narrow temperature window and insufficient durability [7]. On the other hand, many such problems have been solved by a new concept ' NO_x storage-reduction catalyst ' (NSR catalyst) having the ability to store NO_x under oxidizing conditions and to reduce the stored NO_x under reducing conditions. Here, the NSR catalyst has been applied to lean burn gasoline engines in Japan in 1994 [8,9]. However, a shortcoming of the NSR catalysts is the deterioration by SO_2 derived from sulfur in the fuel, that is, it has been necessary to overcome the problem of sulfur poisoning under laboratory and engine operating conditions. Since then, some studies have been published on the NO_x purification mechanism, NO_x purification performance and the cause of deterioration of the NSR catalysts [9-11]. The current state of research on automotive lean NO_x catalysis was reviewed in detail by Misono and Inui [12], and Fritz and Pitchon [13]. On further improving the durability of NSR catalysts, these catalysts have been applied to gasoline direct injection engines in Japan in 1996 and 1999 [14-16]. However, these can be used only in limited markets such as Japan where the sulfur content in gasoline is very low [8,9,14-16]. It is still important to study further improvement of NO_x purification activities of NSR catalysts in the presence of SO_2 under oxidizing conditions.

The purpose of this study was to examine the effect of the addition of transition metals to a $Pt/Ba/Al_2O_3$ catalyst before and after aging treatments on the NO_x storage-reduction catalysis under oxidizing conditions in simulated model gases containing SO_2. Another purpose was to clarify the role of the Fe-compound to improve the NO_x purification activity of the $Pt/Ba/Fe/Al_2O_3$ catalyst in the simulated model gases.

2. Experimental

2.1. Catalyst preparation

Eleven catalysts summarized in Table 1 were prepared for use in this study. The $Pt/Ba/Fe/Al_2O_3$ catalyst was prepared using the following method. A γ-alumina pellet (Nikki Universal, 0.2-0.3 cm in diameter, 150 m^2/g) was contacted by an aqueous solution containing $Pt(NH_3)_2(NO_2)_2$ (Tanaka Precious Metal), $Ba(CH_3COO)_2$ (Wako Pure Chemical Industries) and $Fe(NO_3)_3 \cdot 9H_2O$ (Wako Pure Chemical Industries), followed by drying at 393 K for 12 h and by calcination at 773K for 3h in air. The amount of Pt, Ba, and Fe loading was respectively 1.67, 34.3, and 9.3 wt% of the catalyst.

Table 1. Catalyst formulations.

Catalyst	Pt loading (%)	Ba loading (%)	Transition metal loading (%)
$Pt/Ba/Fe/Al_2O_3$	1.67	34.3	9.3
$Pt/Ba/Co/Al_2O_3$	1.67	34.3	9.8
$Pt/Ba/Ni/Al_2O_3$	1.67	34.3	9.8
$Pt/Ba/Cu/Al_2O_3$	1.67	34.3	10.6
$Pt/Ba/Al_2O_3$	1.67	34.3	—
$Pt/Fe/Al_2O_3$	1.67	—	9.3
$Pt/Co/Al_2O_3$	1.67	—	9.8
$Pt/Ni/Al_2O_3$	1.67	—	9.8
$Pt/Cu/Al_2O_3$	1.67	—	10.6
Pt/Al_2O_3	1.67	—	—
powdery Fe_2O_3 -added $Pt/Ba/Al_2O_3$	1.67	34.3	9.3

The $Pt/Ba/Co/Al_2O_3$, $Pt/Ba/Ni/Al_2O_3$ and $Pt/Ba/Cu/Al_2O_3$ catalysts were prepared in the same way as described above except that an aqueous solution of $Co(NO_3)_2 \cdot 6H_2O$, $Ni(NO_3)_2 \cdot 6H_2O$, and $Cu(NO_3)_2 \cdot 3H_2O$, respectively, was used instead of $Fe(NO_3)_3 \cdot 9H_2O$. The amount of Pt, Ba and Co, Ni, or Cu loading was respectively 1.67, 34.3, and 9.8, 9.8, or 10.6 wt%.

The $Pt/Ba/Al_2O_3$ catalyst was prepared in the same way as described above except that an aqueous solution of the transition metal nitrate was not used. The amount of Pt and Ba metal loading was 1.67 and 34.3 wt% respectively.

The $Pt/Fe/Al_2O_3$, $Pt/Co/Al_2O_3$, $Pt/Ni/Al_2O_3$, $Pt/Cu/Al_2O_3$, and Pt/Al_2O_3 catalysts

were prepared in the same way as described above except that an aqueous solution of $Ba(CH_3COO)_2$ was not used. The amount of Pt and Fe, Co, Ni, or Cu loading was respectively 1.67 and 9.3, 9.8, 9.8, or 10.6 wt%.

The powdery Fe_2O_3-added $Pt/Ba/Al_2O_3$ catalyst was prepared using the following method. Powdery γ-alumina(Nikki Universal, 150 m^2/g) was blended with powdery Fe_2O_3 (Wako Pure Chemical Industries), followed by pressing into disks and pulverizing to 0.2-0.3 cm in diameter. The obtained pellet-type sample was contacted with an aqueous solution containing $Pt(NH_3)_2(NO_2)_2$ and $Ba(CH_3COO)_2$, followed by drying at 393 K for 12 h and by calcination at 773 K for 3 h in air. The amount of Pt, Ba, and Fe loading was respectively 1.67, 34.3, and 9.3 wt% of the catalyst, which was equal to that of the $Pt/Ba/Fe/Al_2O_3$ catalyst.

2.2. Catalyst aging treatment

An aging treatment was performed by placing a 7.5 g catalyst sample in the center of a tube furnace and downstream from a heat exchange zone. A constant treatment temperature was maintained using a thermocouple placed just above the catalyst bed.

The catalyst was first exposed to a simulated oxidizing gas containing SO_2 at 873 K for 5 h. The simulated oxidizing gas consisted of 0.15 % NO, 7.0 % O_2, 0.1 % C_3H_6, 0.5 % CO, 10 % CO_2, 3.0 % H_2O, 0.08 % SO_2, and the balance of N_2 and was passed into a catalyst bed at a gas flow rate of 1,000 cm^3/min. The feedstream was then changed to the simulated reducing gas at 873 K for 30 min. The simulated reducing gas consisted of 0.15 % NO, 0.5 % O_2, 0.1 % C_3H_6, 1.4 % CO, 10 % CO_2, 3.0 % H_2O, and the balance of N_2 and was passed into a catalyst bed at a gas flow rate of 30,000 cm^3/min.

2.3. Catalytic activity measurements

The laboratory reactor system used in this experiment is similar to the previously described system [8,9]. Catalytic activity data were obtained using a conventional fixed-bed flow reactor at atmospheric pressure. A quartz tube with an inner diameter of 3.0 cm was chosen as the reactor tube. A 7.5 g catalyst (about 20 cm^3) was placed on a quartz filter at the middle part of the reactor. The upper part of the catalyst bed was packed with 200 cm^3 of inactive SiC spheres (0.3 cm in diameter) for preheating the feed gas. Furnace temperature was controlled within a maximum variation of 2 K by an automatic temperature controller. The gas leaving the reactor was fed to a condenser to remove the water vapor. The remaining components were continuously analyzed by a nondispersive infrared spectrophotometer (CO and CO_2), a flame ionization detector

(hydrocarbon, HC), magnetic susceptibility (O_2), and chemiluminescence (NO_x) equipped with an automotive gas analyzer (Horiba, MEXA-8120).

The feed compositions and reaction conditions used in this study were as follows: (1) Simulated oxidizing feedstream consisted of 7.9 % O_2, 0.06 % NO, 0.1 % C_3H_6, 0.17 % CO, 9.2 % CO_2, 10 % H_2O and the balance of N_2. This mixture simulated an A/F ratio of 22. (2) The simulated reducing feedstream consisted of 0.6 % O_2, 0.06 % NO, 0.1 % C_3H_6, 1.3 % CO, 14.3 % CO_2, 10 % H_2O and the balance of N_2. This mixture simulated an A/F ratio of 14.0. For each catalytic activity measurement, catalysts were exposed to these simulated feedstreams at a flow rate of 30,000 cm^3/min.

The measurements of NO_x conversion for storage-reduction were conducted by alternating the gas between oxidizing and reducing feedstreams at 120 sec. Fig. 1 shows the NO_x purification behavior of $Pt/Ba/Al_2O_3$. NO_x concentration in the outlet gas gradually increased with time under oxidizing conditions, and NO_x concentration in the outlet gas immediately decayed toward zero under reducing conditions [9]. Though this experiment was carried out for a long period of time, the same behavior was reproducible for each case. As mentioned above, these results indicate that NO_x was stored on the catalyst under oxidizing conditions and that the stored NO_x was then reduced to N_2 under reducing conditions. From the NO_x purification behavior, NOx conversion for NO_x storage-reduction (NO_x conversion for NSR) was calculated by the following equation:

$$NO_x \text{ conversion for NSR}$$

$$= \left[\, 1 - \int_{t_1}^{t_2} ([NO_x]_{inlet} - [NO_x]_{outlet})dt \Big/ \int_{t_1}^{t_2} [NO_x]_{inlet} dt \,\right] \times 100\ (\%), \quad \text{--- (1)}$$

$$t_2 = t_1 + 240 \text{ seconds}$$

where $[NO_x]_{inlet}$ and $[NO_x]_{outlet}$ are the NO_x concentrations in the inlet gas and in outlet gas, respectively, and t_1 and t_2 are initial and final times when the simulated gases are fed alternately under oxidizing and reducing conditions.

When the catalyst was exposed to the simulated gases under oxidizing conditions for a long period, the NO_x concentration in the outlet gas became almost constant but did not reach that in inlet gas [9], because the selective catalytic reduction of NO_x by reducing gases such as C_3H_6 occurred under oxidizing conditions. NO_x conversion for NSR contains NO_x conversion for selective catalytic reduction (NO_x conversion for SCR). So, to clarify the effect of NO_x storage and reduction, the NO_x conversion for

SCR was also measured by the following method, i.e., the catalyst was exposed to the simulated gases under oxidizing conditions until the NO_x concentration in the outlet gas became almost constant. The NO_x conversion for SCR was given by the following equation:

NO_x conversion for SCR
$= [\ 1 - [NO_x]_{outlet}^{constant} / [NO_x]_{inlet}\ ] \times 100\ (\%)$, --- (2)

where $[NO_x]_{outlet}^{constant}$ is the NO_x concentration in the outlet gas when it becomes constant.

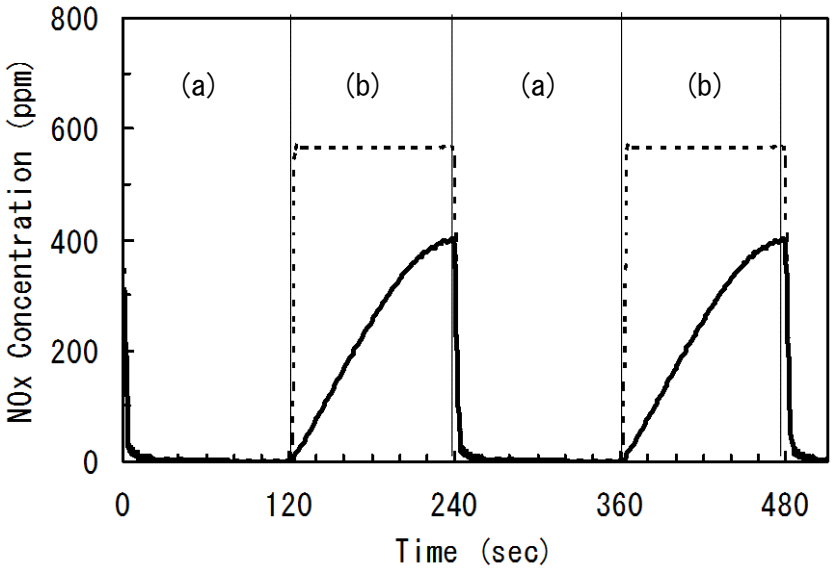

Fig. 1. NOx purification behavior of NOx storage-reduction catalyst (--------) inlet gas, (——) outlet gas; the inlet gas was fed alternately at every 120 s under (a) reducing and (b) oxidizing conditions. Catalyst: $Pt/Ba/Al_2O_3$, temperature: 573K.

2.4. Catalyst characterization

The sulfur content of the aged catalysts was determined by infrared absorption after combustion in an induction furnace [17].

A temperature-programmed desorption (TPD) measurement was performed using a flow system with a fixed-bed reactor. The reactor consisted of a quartz tube with an inner diameter of 0.6 cm and was heated by a furnace. A temperature programmer was used to control catalyst heating at a linear rate of 20K/min from 473 K up to 1073 K.

The carrier gas was 1 % C_3H_6 in N_2 under atmospheric pressure, which flowed over the catalyst at 100 cm^3/min. The effluent from the reactor was analyzed by a quadruple mass spectrometer (ULVAC MSQ-150A).

X-ray diffraction (XRD) measurement was recorded on a Rigaku RINT-2100 equipped with a Cu source(CuKα radiation). Samples of catalyst powder were pressed into wafers and affixed to standard-sized microscope slides. Calculation of the average crystallite size was done using the $BaSO_4$ (310) line width in Scherrer's equation, with the Gaussian line shape approximation.

Scanning electron microscopic (SEM) and energy dispersive X-ray spectroscopic (EDX) observations with a point resolution of 1nm were done using a Nippon Denshi JSM-890.

3. Results and discussion

3.1. NO_x purification activity of fresh catalysts

Table 2 shows the NO_x conversions of fresh catalysts. For all catalysts, the NO_x conversion for NSR is much higher than that for SCR, especially for the Ba-compound-containing catalysts. This result indicates that NO_x purification due to NO_x storage-reduction is more available than that due to the selective catalytic reduction of NO_x.

At first, we confirmed that the NO_x conversion for NSR of the fresh $Pt/Ba/Al_2O_3$ catalyst was much higher than that of the fresh Pt/Al_2O_3 catalyst [9], especially at 573 K and 623 K. This result indicates that the Ba-compound is an effective NO_x storage compound, because the Ba-compound with strong basicity is able to store NO_x to form a stable nitrate to higher temperature.

The NO_x conversion for NSR of the fresh $Pt/Ba/Fe/Al_2O_3$, $Pt/Ba/Co/Al_2O_3$ and $Pt/Ba/Ni/Al_2O_3$ catalysts is nearly equal to that of the fresh $Pt/Ba/Al_2O_3$ catalyst. The NO_x conversion for NSR of the fresh powdery Fe_2O_3-added $Pt/Ba/Al_2O_3$ catalyst is also nearly equal to that of the fresh $Ba/Pt/Fe/Al_2O_3$ catalyst. These results indicate that the addition of Fe-, Co-, and Ni-compounds to the fresh NSR catalysts does not influence the NO_x conversion for NSR. Therefore, Fe-, Co- and Ni-compounds would not interact physically and chemically with NOx, Pt, Ba-compound and Al_2O_3 because of the weaker basicity of the Fe-, Co-, and Ni-compounds than that of the Ba-compound.

Table 2. NOx conversions (%) of fresh catalysts in this study.

Catalyst	For NOx storage-reduction(NSR)			For selective catalytic reduction(SCR)		
	523K	573K	623K	523K	573K	623K
$Pt/Ba/Fe/Al_2O_3$	67.2	55.2	45.4	28.8	12.2	4.0
$Pt/Ba/Co/Al_2O_3$	67.5	54.8	45.6	29.2	12.8	4.9
$Pt/Ba/Ni/Al_2O_3$	67.6	55.9	47.1	29.2	12.7	5.2
$Pt/Ba/Cu/Al_2O_3$	16.4	22.3	23.8	8.0	5.9	3.4
$Pt/Ba/Al_2O_3$	67.8	55.8	47.0	29.3	13.8	5.5
$Pt/Fe/Al_2O_3$	54.2	30.0	12.9	27.3	11.0	4.6
$Pt/Co/Al_2O_3$	51.4	27.2	11.2	26.7	9.9	4.1
$Pt/Ni/Al_2O_3$	52.1	28.0	13.5	26.8	10.1	4.6
$Pt/Cu/Al_2O_3$	20.1	11.4	5.2	10.2	4.0	1.6
Pt/Al_2O_3	52.0	26.2	11.1	26.8	10.0	4.5
powdery Fe_2O_3 -added $Pt/Ba/Al_2O_3$	66.3	54.8	45.8	28.9	13.0	4.5

The NO_x conversion for NSR of the fresh $Pt/Fe/Al_2O_3$, $Pt/Co/Al_2O_3$ and $Pt/Ni/Al_2O_3$ catalysts without the Ba-compound is nearly equal to or slightly higher than that of the fresh Pt/Al_2O_3 catalyst at every temperature. In addition, Sakamoto et al. have reported that the addition of Fe to the Pt/Al_2O_3 catalyst plays no significant role in the reactivity of Pt on the $Pt/Fe/Al_2O_3$ catalyst after being heated in flowing 7.5 % O_2 / N_2 [18]. These results indicate that the addition of Fe-, Co-, and Ni-compounds to the fresh Pt/Al_2O_3 catalyst also has little ability for NOx storage-reduction catalysis because of the weaker basicity of the Fe-, Co-, and Ni-compounds than that of the Ba-compound.

Similarly, the NO_x conversion for SCR of the fresh $Pt/Ba/Fe/Al_2O_3$, $Pt/Ba/Co/Al_2O_3$, $Pt/Ba/Ni/Al_2O_3$ and powdery Fe_2O_3-added $Pt/Ba/Al_2O_3$ catalysts is nearly equal to that of the fresh $Ba/Pt/Al_2O_3$ catalyst. This result indicates that the addition of Fe-, Co-, and Ni-compounds to the fresh $Pt/Ba/Al_2O_3$ catalyst does not influence the NO_x conversion for SCR.

On the other hand, the NO_x conversion for NSR and SCR of the fresh $Pt/Ba/Cu/Al_2O_3$ catalyst is far smaller than that of the fresh $Pt/Ba/Al_2O_3$ catalyst at every temperature. Also, the NO_x conversion for NSR and SCR of $Pt/Cu/Al_2O_3$ is far smaller than that of the fresh Pt/Al_2O_3 catalyst. These results indicate that the addition of a Cu-compound to the fresh NSR catalyst influences the NOx conversion for NSR negatively. Liao et al. have reported that a combined Pt-Cu entity with preferential Cu enrichment exists in $Pt\text{-}Cu/\gamma\text{-}Al_2O_3$ [19]. Pakhomov et al. have reported that a Cu-compound reacted with Pt particles to form Pt-Cu complex oxides such as $C_{1-x}Pt_xO$ on a Pt-Cu catalyst by heat treatment under oxidizing conditions [20]. Probably, because of the formation of Pt-Cu complex oxides, Cu-compounds are thought to be responsible for interacting as a catalyst poison.

3.2. NO_x purification activity of aged catalysts

Table 3 shows the NO_x conversions of aged catalysts exposed to a simulated oxidizing gas containing SO_2 and a simulated reducing gas. The NO_x conversion for NSR of the aged catalysts in Table 3 is smaller than that of the fresh catalysts composed of the same composition in Table 2.

Table 3. NOx conversions (%) of aged catalysts in this study.

Catalyst	For NOx storage-reduction(NSR)			For selective catalytic reduction(SCR)		
	523K	573K	623K	523K	573K	623K
$Pt/Ba/Fe/Al_2O_3$	56.6	38.0	22.3	28.0	12.1	3.8
$Pt/Ba/Co/Al_2O_3$	48.2	33.0	17.9	26.8	12.1	2.8
$Pt/Ba/Ni/Al_2O_3$	48.4	33.2	21.0	26.4	13.7	4.7
$Pt/Ba/Cu/Al_2O_3$	6.1	8.0	10.2	4.7	4.8	2.7
$Pt/Ba/Al_2O_3$	49.8	33.0	19.9	27.3	11.6	3.7
$Pt/Fe/Al_2O_3$	51.6	23.4	7.3	28.0	10.6	3.5
$Pt/Co/Al_2O_3$	47.4	20.3	7.1	27.5	10.8	4.1
$Pt/Ni/Al_2O_3$	46.2	22.3	7.8	27.9	10.8	4.2
$Pt/Cu/Al_2O_3$	3.8	1.9	1.0	6.4	2.4	0.0
Pt/Al_2O_3	49.7	20.7	7.3	27.5	10.7	4.6
powdery Fe_2O_3 -added $Pt/Ba/Al_2O_3$	55.8	38.7	23.3	28.0	12.0	3.7

The NO_x conversion for NSR of the aged $Pt/Ba/Al_2O_3$ catalyst is higher than that of aged Pt/Al_2O_3 catalyst at 573 and 623 K. This result indicates that the Ba-compound is able to store NO_x to form a stable nitrate at higher temperatures such as 573 and 623 K. This suggests that no sulfur-poisoning Ba-compound still remains in the aged $Pt/Ba/Al_2O_3$ catalyst though the aged catalyst is exposed to a simulated oxidizing gas containing SO_2 and a simulated reducing gas.

The NO_x conversion for NSR of the aged $Pt/Ba/Co/Al_2O_3$ and $Pt/Ba/Ni/Al_2O_3$ catalysts is nearly equal to that of the aged $Pt/Ba/Al_2O_3$ catalyst at every temperature as well as that of these fresh catalysts. However, the NO_x conversion of the aged $Pt/Ba/Fe/Al_2O_3$ catalyst is larger than that of the aged $Pt/Ba/Al_2O_3$ catalyst at every temperature, which is quite different from the relation between the fresh $Pt/Ba/Fe/Al_2O_3$ and $Pt/Ba/Al_2O_3$ catalysts. The NO_x conversion of the aged powdery Fe_2O_3-added $Pt/Ba/Al_2O_3$ catalyst is also larger than that of the aged $Pt/Ba/Al_2O_3$ catalyst at every temperature. These results indicate that the addition of the Fe-compound to the NSR catalyst such as $Pt/Ba/Al_2O_3$ plays an important role in the NO_x conversion for NSR, but the addition of Co- and Ni-compounds does not influence the NO_x conversion for NSR. The important role of the Fe-compound in the aged NSR catalyst will be studied in detail later in chapter 3.3.

The NO_x conversion for NSR of aged $Pt/Fe/Al_2O_3$, $Pt/Co/Al_2O_3$ and $Pt/Ni/Al_2O_3$ catalysts without the Ba-compound at every temperature is nearly equal to that of the aged Pt/Al_2O_3 catalyst. This result indicates that the addition of Fe-, Co-, and Ni-compounds to the aged Pt/Al_2O_3 catalyst does not influence the NO_x conversion for NSR. Therefore, the addition of Fe-, Co-, and Ni-compounds to the aged NSR catalysts such as Pt/Al_2O_3 would not interact physically or chemically with NO_x, Pt and Al_2O_3. This tendency is the same as that for these fresh catalysts as shown in Table 2.

On the other hand, The NO_x conversion for NSR of the aged $Pt/Ba/Cu/Al_2O_3$ catalyst is far smaller than that of aged $Pt/Ba/Al_2O_3$ catalyst at every temperature. The NO_x conversion for NSR of the aged $Pt/Cu/Al_2O_3$ catalyst is also far smaller than that of the aged Pt/Al_2O_3 catalyst at every temperature. This tendency is also the same as that for these fresh catalysts as shown in Table 2.

3.3. Role of Fe-compound in the aged NSR catalyst

Table 4 shows the sulfur content in $Pt/Ba/Fe/Al_2O_3$, powdery Fe_2O_3-added $Pt/Ba/Al_2O_3$ and $Pt/Ba/Al_2O_3$ catalysts exposed to only a simulated oxidizing gas containing SO_2, followed by exposure to a simulated reducing gas. The sulfur content of the $Pt/Ba/Fe/Al_2O_3$ catalyst exposed to only an oxidizing gas containing SO_2 is the

same as that of the $Pt/Ba/Al_2O_3$ catalyst exposed to the same gas, which is nearly equal to the total amount of sulfur in the feed gas. The sulfur content of the powdery Fe_2O_3-added $Pt/Ba/Al_2O_3$ catalyst exposed to only an oxidizing gas containing SO_2 is also the same as that of the $Pt/Ba/Al_2O_3$ catalyst exposed to the same gas. The sulfur content of the $Pt/Ba/Fe/Al_2O_3$ catalyst exposed to a reducing gas is about one-half that of the $Pt/Ba/Al_2O_3$ catalyst exposed to the same gas, which is much smaller than the total amount of sulfur in the feed gas. This result indicates that the amount of sulfur desorbed from $Pt/Ba/Fe/Al_2O_3$ catalysts under reducing condition is more than that from a $Pt/Ba/Al_2O_3$ catalyst. The sulfur content of the powdery Fe_2O_3-added $Pt/Ba/Al_2O_3$ catalyst exposed to a reducing gas is also smaller than that of the $Pt/Ba/Al_2O_3$ catalyst exposed to the same gas. The lower sulfur content of the aged $Pt/Ba/Fe/Al_2O_3$ and powdery Fe_2O_3-added $Pt/Ba/Al_2O_3$ catalysts can account for the higher NO_x purification activity after an aging treatment.

Table 4. Sulfur content of catalysts exposed to only a simulated oxidizing gas containing SO_2, followed by exposure to a simulated reducing gas at 873K.

Catalyst	S/Ba atomic ratio (—)*	
	exposed to only oxidizing gas containing SO_2	exposed to reducing gas
$Pt/Ba/Fe/Al_2O_3$	1.4	0.4
powdery Fe_2O_3 -added $Pt/Ba/Al_2O_3$	1.4	0.5
$Pt/Ba/Al_2O_3$	1.4	0.9

* analyzed by infrared absorption method after combustion in an induction furnace

To clarify the difference between the sulfur contents of $Pt/Ba/Fe/Al_2O_3$ and $Pt/Ba/Al_2O_3$ catalysts after an aging treatment, the TPD profile of SO_2 from the $Pt/Ba/Fe/Al_2O_3$ and $Pt/Ba/Al_2O_3$ catalysts was investigated as a function of the amount

of Fe loading. Fig. 2 shows the TPD profile of SO_2 from $Pt/Ba/Fe/Al_2O_3$ catalysts of different Fe loading and $Pt/Ba/Al_2O_3$ catalyst, which were exposed to the simulated oxidizing gas containing SO_2. The SO_2 desorption from the $Pt/Ba/Fe/Al_2O_3$ catalyst occurs at a lower temperature compared to that from the $Pt/Ba/Al_2O_3$ catalyst. In addition, the larger the amount of Fe loading was, the lower the SO_2 desorption temperature was. These results indicate that the Fe-compound promotes the SO_2 desorption from the NSR catalyst.

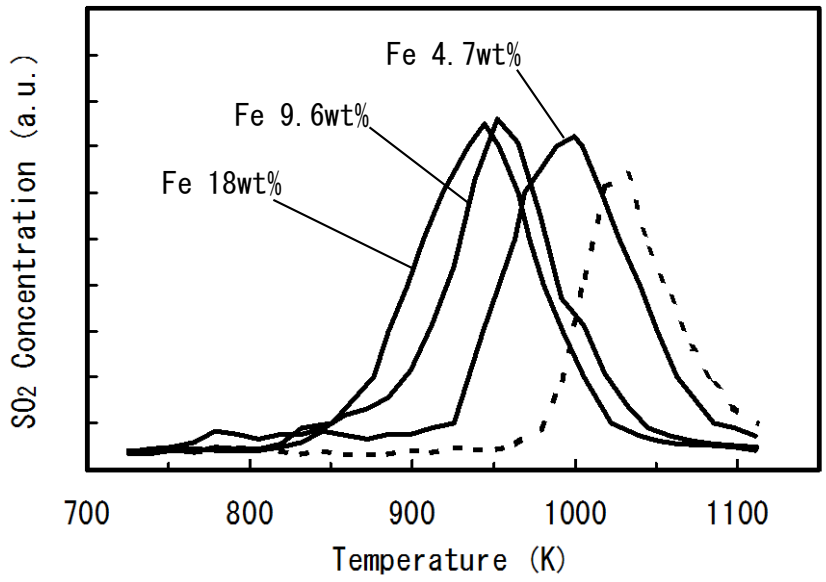

Fig. 2. TPD profile of SO_2 from (——) $Pt/Ba/Fe/Al_2O_3$ catalysts and from (--------) $Pt/Ba/Al_2O_3$ catalyst exposed to a simulated oxidizing gas containing SO_2.

To make clear the effect of Fe-compound, the $BaSO_4$ particle size of the $Pt/Ba/Fe/Al_2O_3$ and $Pt/Ba/Al_2O_3$ catalysts was investigated as a function of the amount of Fe loading. Fig. 3 shows the $BaSO_4$ particle size of $Pt/Ba/Fe/Al_2O_3$ catalysts of different Fe loading and $Pt/Ba/Al_2O_3$ catalyst, which were exposed to the simulated oxidizing gas containing SO_2. The $BaSO_4$ particle size of the $Pt/Ba/Fe/Al_2O_3$ catalysts is far smaller than that of $Pt/Ba/Al_2O_3$ catalyst, although there is no difference between the sulfur contents of these catalysts as shown in Table 4. In addition, the larger the amount of Fe loading was, the smaller the $BaSO_4$ particle size was. These results indicate that the Fe-compound inhibits the growth in size of the $BaSO_4$ particles under oxidizing condition in the presence of SO_2.

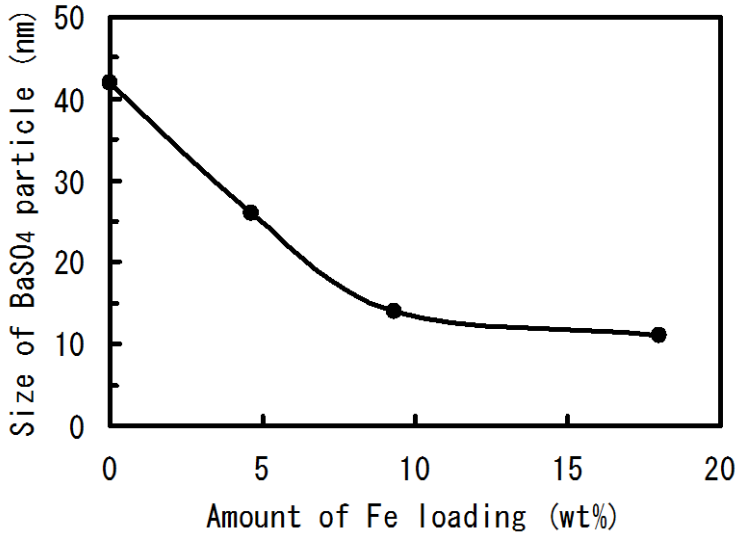

Fig. 3. Size of $BaSO_4$ particles on catalyst exposed to a simulated oxidizing gas containing SO_2. * Calculated using $BaSO_4$ (310) line width in Scherrer's equation, with Gaussian line shape approximation.

The previous paper reported on the interaction between the Ba-compound and Pt on the $Pt/Ba/Al_2O_3$ catalyst: the Ba-compound is highly dispersed and is in contact with Pt on the catalyst [9]. However, there are no reports on the interaction among the Fe-compound, the Ba-compound and Pt on the $Pt/Ba/Fe/Al_2O_3$ catalyst. The state of the Ba-compound with and without the Fe-compound on the $Pt/Ba/Fe/Al_2O_3$ catalyst was further examined using SEM and EDX of the powdery Fe_2O_3-added catalyst which was exposed to a simulated oxidizing gas containing SO_2 and a simulated reducing gas, because the NOx conversion for NSR of the powdery Fe_2O_3-added $Pt/Ba/Al_2O_3$ catalyst is almost the same as that of the $Pt/Ba/Fe/Al_2O_3$ catalyst, as shown in Tables 2 and 3.

Fig. 4 shows a typical high-magnification SEM micrograph of the powdery Fe_2O_3-added $Pt/Ba/Al_2O_3$ catalyst. There are about 2-3 μm Fe_2O_3 clusters in the catalyst, which consist of 0.1-0.2 μm Fe_2O_3 particles. The particles of the Ba-compound are hardly observed, except for only a few particles (smaller than 0.1 μm). This result indicates that small particles of the Ba-compound are homogeneously dispersed. Fig. 5 shows the EDX results of small portions (~1 μm φ) in the catalyst, where Fe_2O_3 particles are present and absent. Sulfur is observed in the portion where Fe_2O_3 particles are absent, but sulfur is not observed in the portion where Fe_2O_3 particles are present. This result indicates that $BaSO_4$ neighboring the Fe-compound decomposes and releases sulfur under reducing condition. That is, the interaction between the

Fe-compound and Ba-compound would occur on the Ba-compound neighboring the Fe-compound, perhaps by forming a kind of composite sulfate on the surface of the $BaSO_4$ particles or by doping of the Fe-compound into the $BaSO_4$ particles.

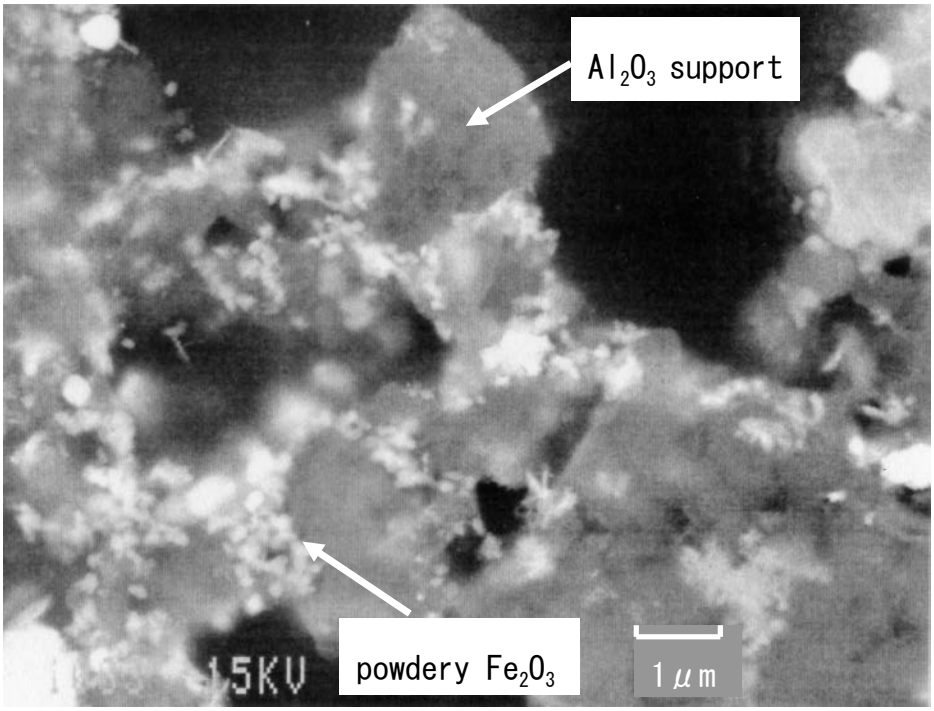

Fig. 4. Scanning electron micrograph (back scattering electron image) of the powdery Fe_2O_3-added $Pt/Ba/Al_2O_3$ catalyst after an aging treatment.

The Fe-compound has been proved to inhibit the growth in size of the $BaSO_4$ particles as mentioned above. As reported in a previous paper [9], the sulfate particle size is an important factor in its decomposition, that is to say, the smaller the sulfate particle size is, the easier the decomposition of sulfates is. Therefore, the Fe-compound promotes the decomposition of the $BaSO_4$ and the desorption of sulfur under reducing conditions as a result of inhibiting the growth in size of $BaSO_4$ neighboring the Fe-compound under oxidizing conditions in the presence of SO_2. The desorption of sulfur leads to the formation of Ba-compound which can store NO_x. Therefore, the Fe-compound proves to be very effective for the NO_x purification activity of aged $Pt/Ba/Fe/Al_2O_3$ and powdery Fe_2O_3-added $Pt/Ba/Al_2O_3$ catalysts exposed to a simulated oxidizing gas containing SO_2 and a simulated reducing gas.

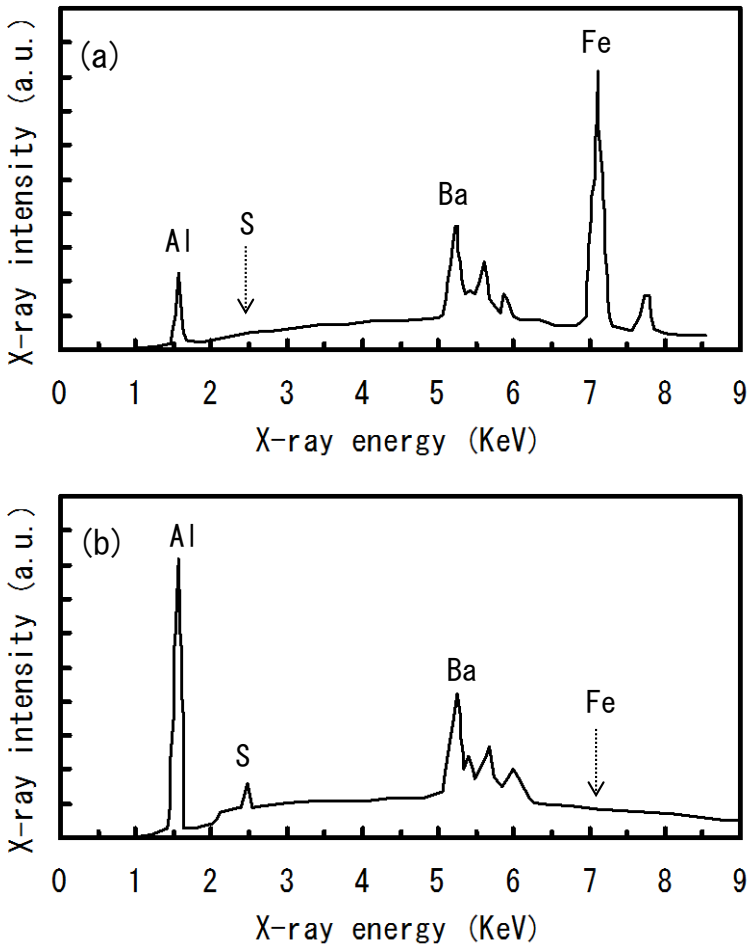

Fig. 5. Energy dispersive X-ray spectroscopic profiles of (a) a small portion where Fe_2O_3 particles are present and (b) a small portion where Fe_2O_3 particles are absent, in the powdery Fe_2O_3-added $Pt/Ba/Al_2O_3$ catalyst after an aging treatment.

4. Conclusions

The effect of the addition of transition metals to a $Pt/Ba/Al_2O_3$ catalyst on the NO_x storage-reduction catalysis under oxidizing conditions in the presence of SO_2 has been studied to improve the durability of the $Pt/Ba/Al_2O_3$ catalyst.

The NO_x purification activity of aged $Pt/Ba/Fe/Al_2O_3$ catalyst was the largest of all the aged catalysts with and without transition metals such as Co-, Ni-, and Cu-compounds after exposure to a simulated oxidizing gas containing SO_2. XRD and EDX data indicated that the Fe-compound on an aged $Pt/Ba/Fe/Al_2O_3$ catalyst played two important roles: (1) preventing a sulfate deposit on the catalyst and (2) inhibiting of the growth in size of $BaSO_4$ particles formed on the catalyst by the reaction of the

Ba-compound with SO_2. Therefore, the Fe-compound promoted the decomposition of $BaSO_4$ particles and the desorption of sulfur when exposed to a simulated reducing gas.

The NO_x purification activity of aged $Pt/Ba/Co/Al_2O_3$ and $Pt/Ba/Ni/Al_2O_3$ catalysts was nearly equal to that of the aged $Pt/Ba/Al_2O_3$ catalyst after exposure to a simulate oxidizing gas containing SO_2. Therefore, the addition of Co- and Ni-compounds to a $Pt/Ba/Al_2O_3$ catalyst on the NOx storage-reduction catalysis had no effect on the NO_x storage-reduction catalysis. The NO_x purification activity of the aged $Pt/Ba/Cu/Al_2O_3$ catalyst was the lowest of all aged catalysts with and without a transition metal after exposure to a simulated oxidizing gas containing SO_2. Therefore, the addition of a Cu-compound had a negative effect on the NO_x storage-reduction catalysis.

References

[1] W. Held, A. Konning, T. Richter, L. Puppe, SAE paper 900496 (1990).

[2] S. Sato, Y. Yu-u, H. Yahiro, N. Mizuno, M. Iwamoto, Appl. Catal. 70 (1991) L1.

[3] Y. Fujitani, H. Muraki, S. Kondoh, M. Fukui, Ger. Offen. DE3735151 (1988).

[4] Y. Kintaichi, H. Hamada, M. Tabata, M. Sasaki, T. Ito, Catal. Lett. 6 (1990) 239.

[5] H. Hamada, Y. Kintaichi, M. Sasaki, T. Ito, M. Tabata, Appl. Catal. 75 (1991) L14.

[6] A. Takami, T. Takemoto, S. Ichikawa, F. Saito, K. Komatsu, 1994 JSAE Spring Convention Proc. 9433858 (1994).

[7] M. Matsumoto, K. Yokota, H. Doi, K. Kimura, K. Sekizawa, Catal. Today 22 (1994) 127.

[8] N. Miyoshi, S. Matsumoto, K. Katoh, T. Tanaka, J. Harada, N. Takahashi, K. Yokota, M. Sugiura, K. Kasahara, SAE paper 950809 (1995).

[9] N. Takahashi, H. Shinjoh, T. Iijima, T. Suzuki, K. Yamazaki, K. Yokota, H. Suzuki, N. Miyoshi, S. Matsumoto, T. Tanizawa, T. Tanaka, S. Tateishi, K. Kasahara, Proc. 1st Int. Cong. On Environ. Catal., Pisa, 1995, p.45 : Catal. Today 27 (1996) 63.

[10] M. S. Brogan, R. J. Brisley, A. P. Walker, D. E. Webster, W. Boegner, N. P. Fekete, M. Kramer, B. Krutzsch, D. Voigtiander, SAE paper 952490 (1995) : W. Boegner, M. Kramer, B. Krutzsch, S. Piscinger, D. Voigtiander, G. Wenniger, F. Wirbeleit, M. S. Brogan, R. J. Brisley, D. E. Webster, Appl. Catal. B 7 (1995) 153.

[11] S. Hodjiati, P. Bernhardt, C. Petit, V. Pitchon, A. Kiennemann, Appl. Catal. B 19 (1998) 209–219.

[12] M. Misono, T. Inui, Catal. Today 51 (1999) 369.

[13] A. Fritz, V. Pitchon, Appl. Catal. B 13 (1997) 1.

[14] Y. Ikeda, K. Sobue, S. Tsuji, S. Matsumoto, SAE Technical Paper 1999-01-1279.

[15] S. Matsumoto, N. Miyoshi, Y. Ikeda, ISATA, 99CPE075 (1999).

[16] S. Matsumoto, Y. Ikeda, H. Suzuki, M. Ogai, N. Miyoshi, Appl. Catal. B 25 (2000) 115.

[17] “Standard Test Method for Determination of Carbon, Sulfur, Nitrogen, Oxygen, and Hydrogen in Steel and Iron, Nickel, and Cobalt Alloys”, Annual Books of ASTM Standards, vol. 03.05, Philadelphia: ASTM, 1989, p.706.

[18] Y. Sakamoto, K. Higuchi, N. Takahashi, K. Yokota, H. Doi, M. Sugiura, Appl. Catal. B 23 (1999) 159.

[19] P. C. Liao, J. J. Carberry, T. H. Fleisch, E. E. Wolf, J. Catal. 74 (1982) 307.

[20] N. A. Pakhomov, N. A. Zaitseva, E. M. Moroz, Kinet. Katal.(Russian), 33 (1992) 426.

Chapter 3

Improved thermal durability of NO_x storage-reduction catalyst

Abstract

The NO_x purification activity through storage-reduction (NSR activity) over a Pt/Ba/(Al_2O_3-CeO_2-Fe_2O_3) catalyst was investigated in comparison with a Pt/Ba/(Al_2O_3-CeO_2) catalyst. Two kinds of reducing agents, C_3H_6 and CO, were used for the measurement of the NSR activity. There was no difference in the NSR activity between these two fresh catalysts. After thermal aging at 1123 K, however, the aged Pt/Ba/(Al_2O_3-CeO_2-Fe_2O_3) catalyst was found to show a higher NSR activity in the case of using CO as a reducing agent than did the aged Pt/Ba/(Al_2O_3-CeO_2) catalyst, although there was no difference in the NSR activity in the case of using C_3H_6 as a reducing agent between these two aged catalysts. Reaction analysis of a simple binary gas system showed that the Fe-compound weakened the CO self-poisoning for the CO-O_2 reaction and the CO-NO_x reaction under reducing conditions, probably by provision of oxygen to the CO from Fe_2O_3 or/and Fe in a Pt-Fe alloy. The weaker CO self-poisoning for the CO-NO_x reaction leads to a greater ability to reduce stored NO_x on the catalysts by CO under reducing conditions, causing a higher NSR activity in the case of using CO as a reducing agent after thermal aging.

Keywords: Lean-burn engine, NO_x storage-reduction catalyst, NO_x purification activity through storage-reduction, Thermal aging, Platinum, Barium, Alumina, Cerium oxide, Iron oxide

1. Introduction

Increasing global environmental concerns have led to a demand for suppression of carbon dioxide (CO_2) emissions, improved fuel efficiency, and a high level of exhaust gas purification. The lean-burn engine system has been one of the key technologies to improve the fuel efficiency of vehicles. This can reduce the fuel consumption and provide more efficient combustion in comparison with a stoichiometric operating engine system. The increased combustion efficiency reduces the amounts of CO_2, carbon monoxide (CO) and hydrocarbons (HC) emitted during driving, and hence more fuel is directly converted into useful energy [1]. However, it is associated with the problem that a conventional three-way catalyst is incapable of fully reducing nitrogen oxides (NO_x)

because of excessive oxygen content in the exhaust gas of a lean-burn engine. Several types of catalyst systems, such as copper ion-exchanged zeolites, metal oxides and precious metals supported on zeolites, have been explored in an attempt to solve this problem [2-7], but no material has been found with the activity and durability necessary for successful commercialization [8,9].

A new concept to solve such problems is the NO_x storage-reduction catalyst (NSR catalyst), which was initially developed by Toyota in the early 1990s [10-13]. The NSR catalyst consists of NO_x storage components based on alkaline earth or alkaline metal oxides, notably BaO, and precious metals, mainly Pt, dispersed on support materials, generally γ-Al_2O_3. The concept of the NSR catalyst is to store NO_x under oxidizing conditions after which it is regenerated under reducing conditions, where NO_x is released and subsequently reduced with HC, CO and H_2 to form N_2, H_2O and CO_2 [11,13]. Many experimental investigations on the NSR catalyst have been conducted and some theoretical models for its reaction have been developed [14-24]. The biggest issue with the NSR catalyst is the deactivation problem. There are two factors in the deactivation of the NSR catalyst, i.e., thermal deterioration and sulfur poisoning. The thermal deterioration seems to result from the reaction of NO_x storage components with the support materials and particle growth of the precious metals and NO_x storage components. The sulfur poisoning could to be ascribed to sulfate formation caused by the reaction of NO_x storage components with SO_2 in the exhaust gas and seems to be the most difficult problem to solve for the NSR catalyst.

In the development process of the NSR catalyst, we have found that the addition of an Fe-compound to the NSR catalyst improves the durability against sulfur poisoning and thermal deterioration. Consequently, this approach became the basis for the first NSR catalyst which was put into the Japanese market in 1994. In a previous paper [25], we reported that the addition of an Fe-compound to a Pt/Ba/Al_2O_3 catalyst lowered the desorption temperature of the adsorbed sulfate complexes by limiting the size of the barium sulfate particles after exposure to a simulated oxidizing gas containing SO_2. Recently, Fanson et al., using FT-IR spectroscopy, reported that the addition of an Fe-compound improves the long-term satiability of catalysts caused by the formation of a previously unobserved bulk nitrate species [26].

The purpose of this study is to clarify the effect of the addition of an Fe-compound to the NSR catalyst on its NO_x purification activity through storage-reduction (NSR activity) after thermal aging, by comparison between Pt/Ba/(Al_2O_3-CeO_2-Fe_2O_3) and Pt/Ba/(Al_2O_3-CeO_2) catalysts. Another purpose is to clarify the role of the Fe-compound in the improved durability against thermal deterioration of the NSR

catalyst.

2. Experimental

2.1. Catalyst preparation

The Pt/Ba/(Al_2O_3-CeO_2-Fe_2O_3) catalyst was prepared using a two-step wet impregnation method. Firstly, powdery γ-Al_2O_3 (Nikki Universal, 150 m^2/g) was blended with powdery CeO_2 (Wako Pure Chemical Industries, 120 m^2/g), and Fe_2O_3 (Wako Pure Chemical Industries) in distilled water and contacted with an aqueous solution containing $Pt(NH_3)_2(NO_2)_2$ (Tanaka Precious Metals), followed by drying at 393 K for 12 h and by calcination at 773 K for 3 h in air. The resultant powdery product was then contacted with an aqueous solution containing $Ba(CH_3COO)_2$ (Wako Pure Chemical Industries), followed by drying at 393 K for 12 h and by calcination at 773 K for 3 h in air. The amount of Pt, BaO and CeO_2 was respectively 0.83, 19.1, and 20.4 wt.% of the catalyst. The amount of Fe_2O_3 was 3.3, 6.6(mainly), or 13.2 wt.% of the catalyst.

The Pt/Ba/(Al_2O_3-CeO_2) catalyst was prepared in the same way as described above except that powdery Fe_2O_3 was not used. The amount of Pt, BaO and CeO_2 was respectively 0.83, 19.1, and 20.4 wt.% of the catalyst, which was equal to that of the Pt/Ba/(Al_2O_3-CeO_2-Fe_2O_3) catalyst.

The prepared catalysts were pressed into disks and pulverized to a 0.17 - 0.28 cm size in diameter for use in catalyst aging treatment and catalytic activity measurements.

2.2. Catalyst aging treatment

A thermal aging treatment was performed by placing a 10.0 g catalyst sample in the center of a tube furnace and downstream from a heat exchange zone. A constant treatment temperature was maintained using a thermocouple placed just above the catalyst bed.

The catalyst was exposed to a cycled feedstream simulating a stoichiometric engine exhaust gas at 1123 K for 5 h. Table 1 shows the composition of the cycled feedstream, which alternately changes between oxidizing and reducing conditions every 5 minutes. The feedstream was passed into the catalyst bed at a gas flow rate of 1,000 cm^3/min.

Table 1. Gas compositions for thermal aging

Condition	Concentration (vol.%)							
	C_3H_6	CO	H_2	NO	O_2	CO_2	H_2O	N_2
Oxidizing	0.067	0.075	0.025	0.12	1.20	10.0	3.0	bal.
Reducing	0.067	1.50	0.50	0.12	0.25	10.0	3.0	bal.

2.3. Catalytic activity measurements

The laboratory reactor system used in this experiment is similar to the previously described system [11, 27]. Catalytic activity data were obtained using a conventional fixed-bed flow reactor system at atmospheric pressure, equipped with mass flow controllers and injector valves to obtain a premixed feedstream of desired composition, simulating the various air-to-fuel ratios (A/F ratios) of the engine exhaust gas. This apparatus can deliver a cycled feedstream to simulate the dynamic behavior of an engine exhaust gas. The stoichiometry number, S, used to identify the redox characteristic of the feedstreams, which is related to the A/F ratio of the engine exhaust gas, is defined as follows:

$$S = (2[O_2] + [NO]) / ([H_2] + [CO] + 9[C_3H_6])$$

When S<1.0, S=1.0, and S>1.0, the redox characters of the feedstream are net reducing, stoichiometric, and net oxidizing, respectively. A quartz tube with an inner diameter of 3.0 cm was chosen as the reactor tube. A 10.0 g catalyst (about 20 cm^3) was placed on a quartz filter in the middle part of the reactor. The upper part of the catalyst bed was packed with 200 cm^3 of inactive quartz spheres (0.3 cm in diameter) for preheating the feed gas. The furnace temperature was controlled within a maximum variation of 2 K by an automatic temperature controller. The gas leaving the reactor was fed to a condenser to remove the water vapor. The remaining components were continuously analyzed by a nondispersive infrared spectrophotometer (CO and CO_2), a flame ionization detector (hydrocarbon, HC), magnetic susceptibility (O_2), and chemiluminescence (NO_x) equipped with an automotive gas analyzer (Best-Sokki, CATA-5000).

The measurements of NSR activity were conducted at constant temperatures by alternating the gas between oxidizing and reducing feedstreams, at 60 seconds and 3 seconds, respectively. Table 2 shows the composition of the oxidizing and reducing feedstreams, which simulate A/F ratios of 22 and 12, respectively. As a reducing agent,

either C_3H_6 or CO was used in the reducing feedstream. The flow rate of these feedstreams was kept at 30,000 cm^3/min, resulting in a space velocity of about 90,000 h^{-1}. The NO_x conversion was calculated as the overall conversion under oxidizing and reducing conditions by using the following equation:

$$\text{NOx conversion} = \left(1 - \int_{t_1}^{t_2} [NO_x]_{outlet} dt \Big/ \int_{t_1}^{t_2} [NO_x]_{inlet} dt\right) \times 100\ (\%) \text{ -------- (1)}$$

$$t_2 = t_1 + 63\ s$$

where $[NO_x]_{inlet}$ and $[NO_x]_{outlet}$ are the inlet and outlet NO_x concentrations, respectively.

2.4. Simple binary gas reaction

Reaction analysis of simple binary gas systems was conducted using the same reactor system as that used for catalytic activity measurements. The conversions of CO, HC and NO_x as a function of reaction temperature were measured with premixed CO-O_2, C_3H_6-O_2 and CO-NO feedstreams of desired compositions. The flow rate of these feedstreams was kept at 30,000 cm^3/min.

2.5. Catalyst Characterization

The BET surface area was measured by N_2 adsorption at liquid nitrogen temperature using a conventional flow-type adsorption apparatus.

X-ray diffraction (XRD) measurement was carried out with a Rigaku RINT-2100 X-ray diffractometer using Cu Kα radiation. The samples of catalyst powder were pressed and loaded on a sample holder at a depth of 0.1 cm. Calculation of the crystalline particle size was done using the diffraction line width in Scherrer's equation with the Gaussian line shape approximation.

X-ray photoelectron spectra (XPS) measurements were conducted using a V. G. Scientific Escalab MK III with Mg Kα X-rays under 1×10^{-7} Torr O_2 pressure at room temperature by a conventional method which involved exposure of the sample to air for a few minutes when placing it on the sample holder. The $Pt4d_{5/2}$ and $Fe2p_{3/2}$ binding energies were calibrated using Si2p (103.4 kV).

Table 2. Gas compositions for the measurement of NOx purification activity through storage-reduction

		Concentration (vol.%)							S	Time
		C_3H_6	CO	NO	O_2	CO_2	H_2O	N_2	(−)	(s)
Oxidizing		−	−	0.050	7.0	10.0	10.0	bal.	∞	60
Reducing	#1	0.556	−	0.050	0.2	10.0	10.0	bal.	0.09	3
	#2	−	5.00	0.050	0.2	10.0	10.0	bal.		

Table 3. BET surface areas of fresh and aged catalysts

Catalyst	Amount of Fe_2O_3 loading (wt.%)	BET surface area (m^2/g)		Decrease in BET surface area* (%)
		Fresh	Aged	
Pt/Ba/(Al_2O_3-CeO_2-Fe_2O_3)	3.3	126	75	40
	6.6	116	69	40
	13.2	110	66	39
Pt/Ba/(Al_2O_3-CeO_2)		130	80	39

* [1−(BET surface area of aged catalyst) / (that of fresh catalyst)] × 100 (%)

3. Results and Discussion

3.1. Thermal stability of support materials and Pt

Table 3 shows the BET surface areas of fresh and aged catalysts examined in this study. For both fresh and aged catalysts, the surface areas of all Pt/Ba/(Al_2O_3-CeO_2-Fe_2O_3) catalysts were lower than that of a Pt/Ba/(Al_2O_3-CeO_2) catalyst. However, the decrease in the BET surface area caused by the thermal aging (see Table 3) of the former catalysts was almost equal to that of the latter catalyst. Table 4 shows the Pt particle sizes calculated by XRD measurement on the aged catalysts. There was no significant difference in the Pt particle sizes among all of the aged catalysts. Therefore, the addition of an Fe-compound to a Pt/Ba/(Al_2O_3-CeO_2) catalyst does not influence the thermal stability of the support materials and Pt during thermal aging at 1123 K.

Table 4. Pt particle size of aged catalysts

Catalyst	Amount of Fe_2O_3 loading (wt.%)	Pt particle size (nm)
Pt/Ba/(Al_2O_3-CeO_2-Fe_2O_3)	3.3	15.8
	6.6	17.0
	13.2	17.5
Pt/Ba/(Al_2O_3-CeO_2)		19.3

3.2. NO_x purification activity through storage-reduction (NSR activity)

The NSR activity of the Pt/Ba/(Al_2O_3-CeO_2-Fe_2O_3) catalyst with 6.6 wt.% Fe_2O_3 loading was compared with that of the Pt/Ba/(Al_2O_3-CeO_2) catalyst. Fig. 1 (a) shows the outlet NO_x concentration profiles at 573 K in the case of using C_3H_6 as a reducing agent over the two fresh catalysts during the measurement of the NSR activity. As shown in the figure, good reproducibility was observed in each outlet NO_x concentration profile, after alternating oxidizing and reducing conditions for a long period (about 20 minutes). Under oxidizing conditions, the outlet NO_x concentration increases slowly with time, which means that some NO_x is stored in the catalyst, as mentioned previously [11]. Under reducing conditions, a quick increase in the outlet NO_x concentration is observed in the first few seconds. This may occur for two reasons. One is that the ability to store NO_x in the catalyst decreased when the O_2 concentration decreased, followed by the release of stored NO_x from the catalyst. The other is that, in

the first few seconds of the reducing conditions, a certain amount of oxygen remains on a Pt site, which impedes the reduction of NO_x on the Pt site. However, the inlet NO_x concentration decreases quickly under reducing conditions, indicating that some of the stored NO_x is reduced by C_3H_6, as mentioned previously [11]. A comparison between the two fresh catalysts showed no difference in the outlet NO_x concentration profile in the case of using C_3H_6. Fig. 2 (a) shows the NO_x conversions of the two fresh catalysts in case of using C_3H_6 as a reducing agent, calculated from the integration of the inlet and outlet NO_x concentration profiles. The NO_x conversion of the fresh Pt/Ba/(Al_2O_3-CeO_2-Fe_2O_3) catalyst was almost the same as that of the fresh Pt/Ba/(Al_2O_3-CeO_2) catalyst at temperatures from 523 to 623 K.

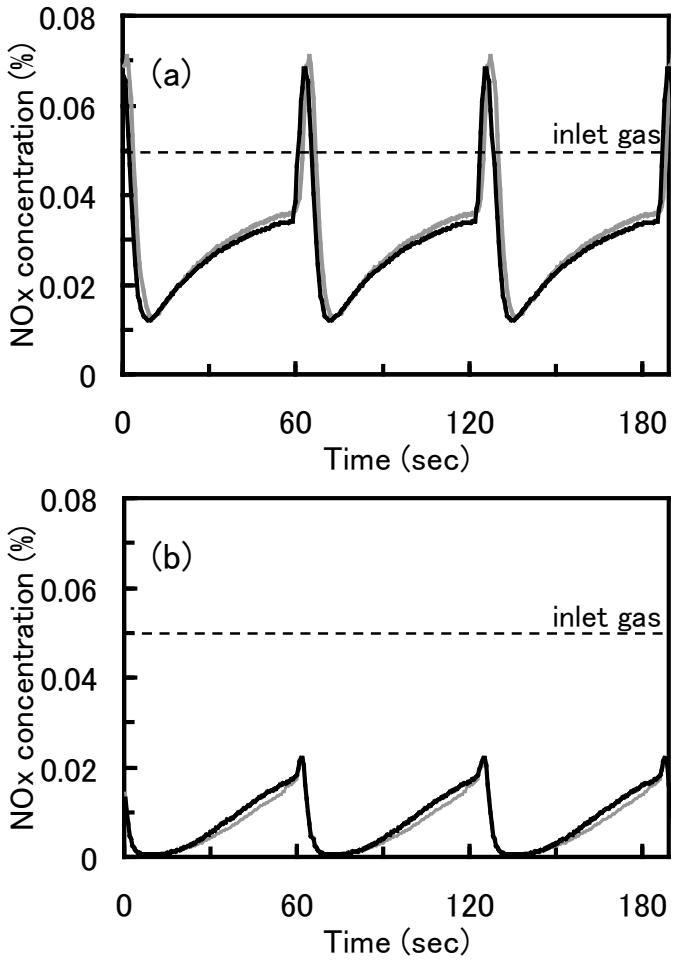

Fig. 1. NO_x concentration profiles at 573 K under alternating oxidizing (60 s) and reducing (3 s) conditions in the case of using (a) C_3H_6 and (b) CO as a reducing agent, over a fresh Pt/Ba/(Al_2O_3-CeO_2-Fe_2O_3) catalyst with 6.6 wt.% Fe_2O_3 loading (black line) and a fresh Pt/Ba/(Al_2O_3-CeO_2) catalyst (gray line).

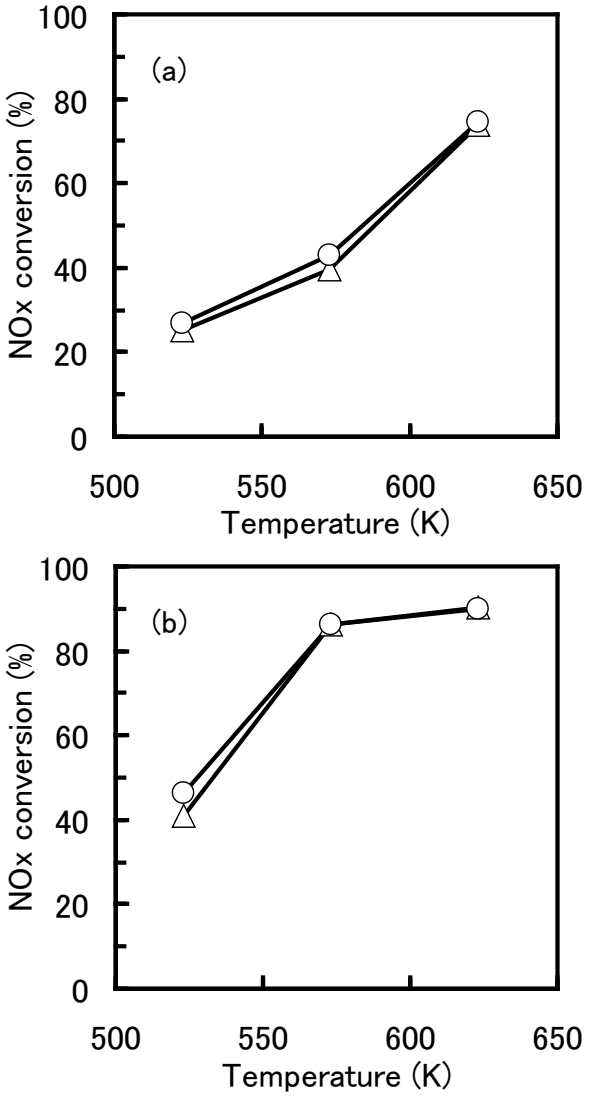

Fig. 2. NO_x conversions (%) through NO_x storage-reduction of a fresh Pt/Ba/(Al_2O_3-CeO_2-Fe_2O_3) catalyst with 6.6 wt.% Fe_2O_3 loading (○) and a fresh Pt/Ba/(Al_2O_3-CeO_2) catalyst (△), in the case of using (a) C_3H_6 and (b) CO as a reducing agent.

Fig. 1 (b) shows the outlet NO_x concentration profiles at 573 K when using CO as a reducing agent over the two fresh catalysts during the measurement of the NSR activity. The NO_x concentration profile when using CO showed the same behavior as that when using C_3H_6, i.e., increasing slowly under oxidizing conditions, a quick increase in the first few seconds of the reducing conditions, decreasing quickly under reducing conditions, and good reproducibility after alternating oxidizing and reducing conditions over a long period. On the other hand, by comparing Fig. 1 (b) with (a), the NO_x concentration in the case of using CO was far lower than that in the case of using C_3H_6

over each catalyst, although there was no difference in the S value of the feedstream under the reducing condition (see Table 2) between the cases of using C_3H_6 and CO. This result suggests that CO reduces the stored NO_x more effectively than does C_3H_6. By comparison between the two fresh catalysts, there was also no difference in the outlet NO_x concentration profile in the case of using CO. Fig. 2 (b) shows the NO_x conversions of the two fresh catalysts in the case of using CO as a reducing agent. The NO_x conversion of the fresh Pt/Ba/(Al_2O_3-CeO_2-Fe_2O_3) catalyst was almost the same as that of the fresh Pt/Ba/(Al_2O_3-CeO_2) catalyst at temperatures from 523 to 623 K. Therefore, the addition of an Fe-compound to the fresh NSR catalyst does not influence the NSR activity when using either C_3H_6 or CO as a reducing agent.

Fig. 3 (a) shows the outlet NO_x concentration profiles at 573 K when using C_3H_6 as a reducing agent over the aged Pt/Ba/(Al_2O_3-CeO_2-Fe_2O_3) catalyst and the aged Pt/Ba/(Al_2O_3-CeO_2) catalyst during the measurement of the NSR activity. Fig. 4 (a) shows the NO_x conversions of the two aged catalysts in the case of using C_3H_6 as a reducing agent. There was no significant difference in the outlet NO_x concentration profiles between the two aged catalysts, and the NO_x conversion of the former catalyst was equal to or slightly lower than that of the latter catalyst at temperatures from 523 to 623 K. On the other hand, Fig. 3 (b) shows the outlet NO_x concentration profiles at 573 K when using CO as a reducing agent over the two aged catalysts during the measurement of the NSR activity. Fig. 4 (b) shows the NO_x conversions of the two aged catalysts when using CO as a reducing agent. The outlet NO_x concentration under oxidizing and reducing conditions over the aged Pt/Ba/(Al_2O_3-CeO_2-Fe_2O_3) catalyst was lower than that of the aged Pt/Ba/(Al_2O_3-CeO_2) catalyst. The NO_x conversion of the former catalyst was higher than that of the latter catalyst at temperatures from 523 to 573 K, although that of the former catalyst was almost the same as that of the latter catalyst at 623 K. Thus we can see that the addition of an Fe-compound to the aged NSR catalyst improves the NSR activity when using CO as a reducing agent at relatively low temperature (up to 573 K), after thermal aging at 1123 K.

3.3. Role of Fe-compound

First, in order to clarify the role of an Fe-compound after thermal aging, simple binary gas reaction systems were investigated on the aged Pt/Ba/(Al_2O_3-CeO_2-Fe_2O_3) catalyst with 6.6 wt.% Fe_2O_3 loading and the aged Pt/Ba/(Al_2O_3-CeO_2) catalyst. Fig. 5 shows the conversions (a) of CO in the CO-O_2 reaction, (b) of HC in the C_3H_6-O_2 reaction, and (c) of CO in the CO-NO reaction under stoichiometric conditions as a function of the reaction temperature. CO in the CO-O_2 reaction and CO in the CO-NO

reaction over the aged Pt/Ba/(Al_2O_3-CeO_2-Fe_2O_3) catalyst were converted at far lower temperatures than over the aged Pt/Ba/(Al_2O_3-CeO_2) catalyst, although C_3H_6 in the C_3H_6-O_2 reaction over the former catalyst was converted at a slightly higher temperature than over the latter catalyst.

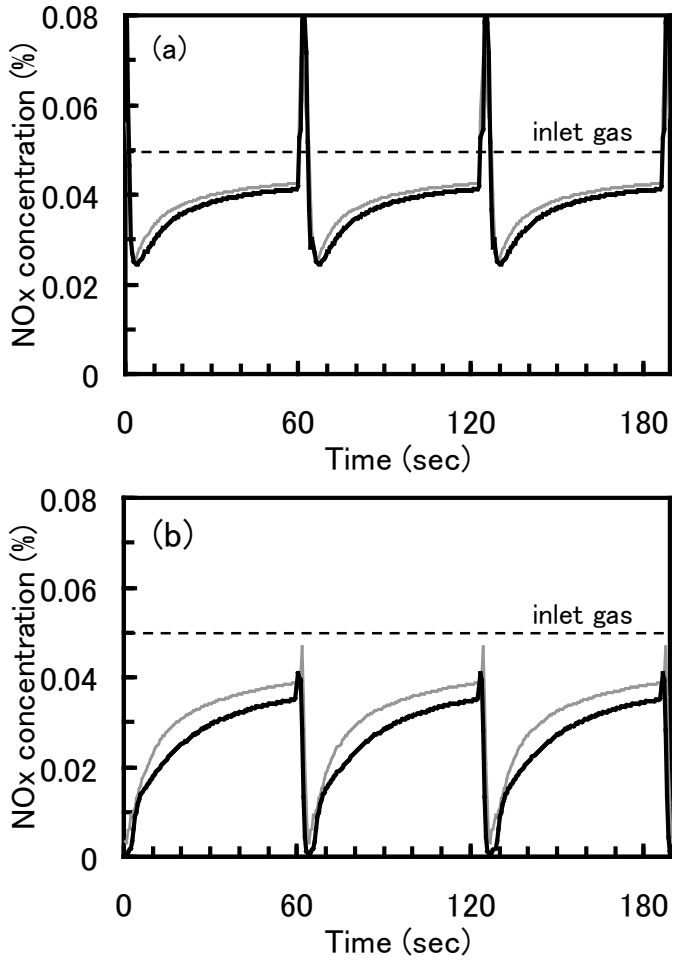

Fig. 3. NO_x concentration profiles at 573 K under alternating oxidizing (60 s) and reducing (3 s) conditions in the case of using (a) C_3H_6 and (b) CO as a reducing agent, over an aged Pt/Ba/(Al_2O_3-CeO_2-Fe_2O_3) catalyst with 6.6 wt.% Fe_2O_3 loading (black line) and an aged Pt/Ba/(Al_2O_3-CeO_2) catalyst (gray line) after thermal aging at 1123 K.

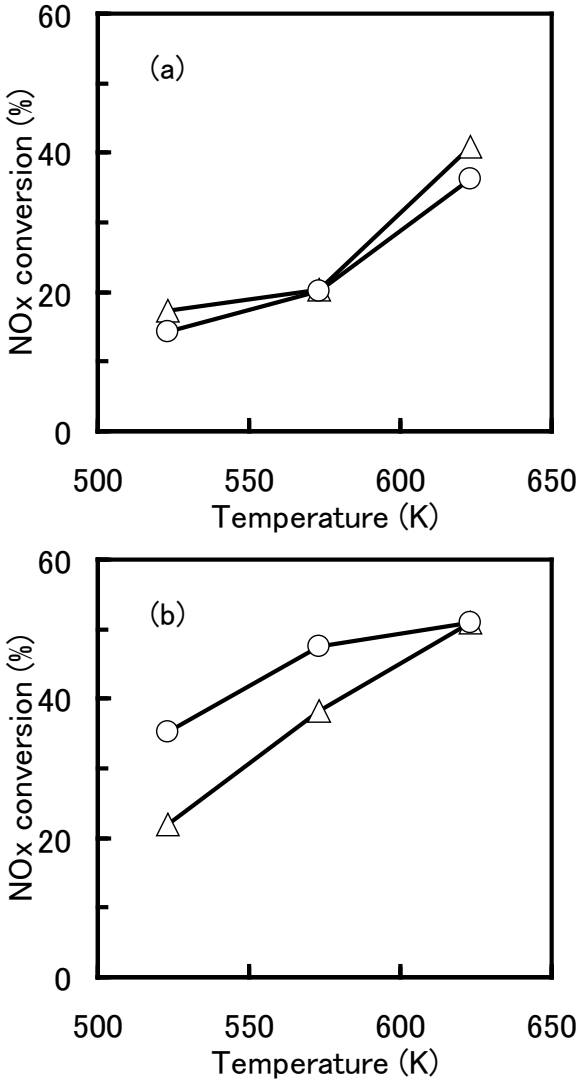

Fig. 4. NO_x conversions (%) through NO_x storage-reduction of an aged Pt/Ba/(Al_2O_3-CeO_2-Fe_2O_3) catalyst with 6.6 wt.% Fe_2O_3 loading (○) and an aged Pt/Ba/(Al_2O_3-CeO_2) catalyst (△) after thermal aging at 1123 K, when using (a) C_3H_6 and (b) CO as a reducing agent.

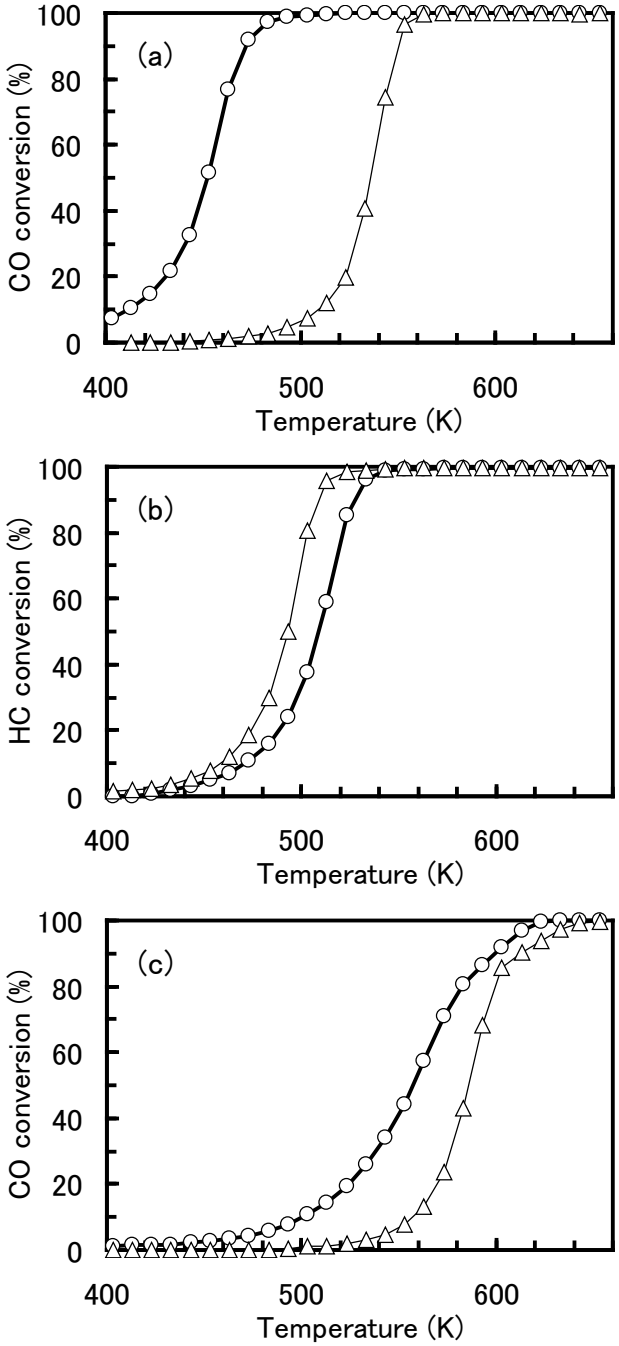

Fig. 5. Conversions (a) of CO in the CO-O_2 reaction, (b) of HC in the C_3H_6-O_2 reaction, and (c) of CO in the CO-NO reaction, under stoichiometric conditions as a function of reaction temperature, over an aged Pt/Ba/(Al_2O_3-CeO_2-Fe_2O_3) catalyst with 6.6 wt.% Fe_2O_3 loading (○) and an aged Pt/Ba/(Al_2O_3-CeO_2) catalyst (△). Reaction conditions are (a) 1% CO and 0.5% O_2, (b) 0.067% C_3H_6 and 0.3% O_2, and (c) 0.12% CO and 0.12% NO.

Next, in order to account for the role of an Fe-compound in the activity for CO and

O_2 under reducing conditions after thermal aging, the reaction analysis of the CO-O_2 reaction under reducing conditions over the aged Pt/Ba/(Al_2O_3-CeO_2-Fe_2O_3) catalyst with 6.6 wt.% Fe_2O_3 loading and the aged Pt/Ba/(Al_2O_3-CeO_2) catalyst was conducted The kinetics of the CO-O_2 reaction was subjected to empirical laws: the rate of carbon dioxide formation, v, is generally expressed by the following equation:

$$v = k \times P_{CO}^{m} \times P_{O2}^{n} \times \exp(-\Delta E / RT)$$

where P_{CO} and P_{O2} are the partial pressures of CO and O_2 and the partial reaction orders m and n are derived from data obtained under conditions of low conversion, usually less than 30%. The range of P_{CO} and P_{O2} are respectively 1.0-6.0% and 0.2-1.5%. The values of m and n were determined from a conventional log-log relation between rate and partial pressures of the respective species at about 473 K. The kinetic parameters determined over the aged catalysts are summarized in Table 5. The reaction order with respect to CO partial pressure, m, over the aged Pt/Ba/(Al_2O_3-CeO_2-Fe_2O_3) catalyst was of negative order (–0.2), but its absolute value was smaller than that of the aged Pt/Ba/(Al_2O_3-CeO_2) catalyst (–1.0). The reaction order with respect to O_2 partial pressure, n, over the former catalyst was of positive order, which was almost equal to that of the latter catalyst. The negative order with CO and the positive order with O_2 suggest that CO is adsorbed strongly on the catalyst surface, causing CO self-poisoning for the CO-O_2 reaction [28]. The smaller absolute value of the negative reaction order with respect to CO partial pressure over the aged Pt/Ba/(Al_2O_3-CeO_2-Fe_2O_3) catalyst compared with that over the aged Pt/Ba/(Al_2O_3-CeO_2) catalyst suggests that the CO self-poisoning over the former catalyst is weaker than that over the latter catalyst. We may therefore reasonably conclude that an Fe-compound on the aged Pt/Ba/(Al_2O_3-CeO_2-Fe_2O_3) catalysts weakens the CO self-poisoning for the CO-O_2 reaction.

Table 5. Partial reaction orders in CO-O_2 reaction at 473K over the aged catalysts

Catalyst	m	n
Pt/Ba/(Al_2O_3-CeO_2-Fe_2O_3)	−0.2	1.0
Pt/Ba/(Al_2O_3-CeO_2)	−1.0	1.1

[$v = k \times P_{CO}^{m} \times P_{O2}^{n} \times \exp(-\Delta E / RT)$]
The range of P_{CO} and P_{O2} are respectively 1.0-6.0% and 0.2-1.5%

The reaction analysis of the CO-NO reaction under reducing conditions over the aged Pt/Ba/(Al_2O_3-CeO_2-Fe_2O_3) catalyst with 6.6 wt.% Fe_2O_3 loading and the aged Pt/Ba/(Al_2O_3-CeO_2) catalyst was also conducted using the following equation, as well as that of the CO-O_2 reaction:

$$v = k \times P_{CO}^{m} \times P_{NO}^{n} \times \exp(-\Delta E / RT)$$

where v is the rate of carbon dioxide formation, P_{CO} and P_{NO} are the partial pressures of CO and NO and the partial reaction orders m and n are derived from data obtained under conditions of low conversion. The range of P_{CO} and P_{NO} are respectively 0.24-0.96% and 0.12-0.48%. The kinetic parameters determined at about 623K are summarized in Table 6. The reaction order with respect to CO partial pressure, m, over the aged Pt/Ba/(Al_2O_3-CeO_2-Fe_2O_3) catalyst was of negative order (–0.7), but its absolute value was smaller than that of the aged Pt/Ba/(Al_2O_3-CeO_2) catalyst (–1.5). The reaction order with respect to NO partial pressure, n, over the former catalyst was of positive order, as well as that of the latter catalyst. The negative order with CO and the positive order with NO suggest that CO is adsorbed strongly on the catalyst surface, causing CO self-poisoning for the CO-NO reaction. The smaller absolute value of the negative reaction order with respect to CO partial pressure over the aged Pt/Ba/(Al_2O_3-CeO_2-Fe_2O_3) catalyst compared with that over the aged Pt/Ba/(Al_2O_3-CeO_2) catalyst suggests that the CO self-poisoning for the CO-NO reaction over the former catalyst is weaker than that over the latter catalyst. Therefore, it seems reasonable to conclude that an Fe-compound on the aged Pt/Ba/(Al_2O_3-CeO_2-Fe_2O_3) catalyst weakens the CO self-poisoning for the CO-NO reaction, as well as that for the CO-O_2 reaction, causing improvement in the activity for CO and NO_x under reducing conditions after thermal aging.

Table 6. Partial reaction orders in CO-NO reaction at 623K over the aged catalysts

Catalyst	m	n
Pt/Ba/(Al_2O_3-CeO_2-Fe_2O_3)	−0.7	0.7
Pt/Ba/(Al_2O_3-CeO_2)	−1.5	1.5

[$v = k \times P_{CO}^{m} \times P_{NO}^{n} \times \exp(-\Delta E / RT)$]
The range of P_{CO} and P_{NO} are respectively 0.24-0.96% and 0.12-0.48%

Thirdly, in order to shed light on the role of an Fe-compound in the NSR activity in the case of using CO as a reducing agent after thermal aging, the ability to store NOx under oxidizing conditions and the ability to reduce stored NO_x on the catalysts under reducing conditions were separately investigated over the aged Pt/Ba/(Al_2O_3-CeO_2-Fe_2O_3) catalyst with 6.6 wt.% Fe_2O_3 loading and the aged Pt/Ba/(Al_2O_3-CeO_2) catalyst using the same oxidizing and reducing feedstreams as those for the measurement of the NSR activity. At the start, after the catalyst was exposed to a feedstream of 3% H_2 in N_2 at 673 K for 10 minutes to regenerate from stored NO_x, it was exposed to the oxidizing feedstream at 573 K until the outlet NO_x concentration became constant. Fig. 6 (a) shows the outlet NO_x concentration profiles over the two aged catalysts, when exposed to the oxidizing feedstream. The outlet NO_x concentration over the aged Pt/Ba/(Al_2O_3-CeO_2-Fe_2O_3) catalyst increases more rapidly than that over the aged Pt/Ba/(Al_2O_3-CeO_2) catalyst, and they become constant at the same value after a long period (1200 seconds). These results indicate that the ability of the former catalyst to store NO_x under oxidizing conditions is lower than that of the latter catalyst. The catalyst was subsequently exposed to the reducing feedstream with CO as a reducing agent for 3 seconds, followed by the oxidizing feedstream at 573 K until the outlet NO_x concentration became constant again. Fig. 6 (b) shows the inlet NOx concentration profiles when exposed to the reducing feedstream (3 seconds) and followed by the oxidizing feedstream. The outlet NO_x concentration over the aged Pt/Ba/(Al_2O_3-CeO_2-Fe_2O_3) catalyst increases more slowly than does that over the aged Pt/Ba/(Al_2O_3-CeO_2) catalyst, and they become constant at the same value again after a long period (600 seconds), which is quite different from the relation between the two aged catalysts in Fig. 6 (a). These results indicate that the ability to reduce stored NO_x by CO under reducing conditions of the former catalyst is higher than that of the latter catalyst, contrary to the relation of the ability to store NO_x under oxidizing conditions. Therefore, the higher NSR activity of the aged Pt/Ba/(Al_2O_3-CeO_2-Fe_2O_3) catalyst in the case of using CO as a reducing agent can explained by its higher ability to reduce stored NO_x by CO, compared with the aged Pt/Ba/(Al_2O_3-CeO_2) catalyst. Takahashi et al. have reported the NOx storage and reduction mechanism, i.e., NO_x is oxidized on precious metals and stored on neighboring NO_x storage components as nitrates under oxidizing conditions, and the nitrates are decomposed into NO_x by reducing agents activated on precious metals, followed by the reduction of the emitted NO_x into N_2 on precious metals by reducing agents under reducing conditions [11]. Thus, the final NO_x reduction process over NSR catalysts under reducing conditions is the same as the reaction between reducing agents and NO_x on precious metals over a three-way catalyst

under reducing conditions. We have already said that an Fe-compound on the aged Pt/Ba/(Al_2O_3-CeO_2-Fe_2O_3) catalyst weakens the CO self-poisoning for the CO-O_2 and CO-NO_x reactions under reducing conditions. The absence of the effect of an Fe-compound on the NSR activity at a relatively high temperature (623 K) supports the CO self-poisoning, which generally occurs at a relatively low temperature. Therefore, these results lead to the conclusion that an Fe-compound on the aged Pt/Ba/(Al_2O_3-CeO_2-Fe_2O_3) catalyst weakens the CO self-poisoning for the CO-O_2 and CO-NO_x reactions under reducing conditions and consequently enhances the ability to reduce stored NO_x by CO, causing improvement in the NSR activity when using CO as a reducing agent at a relatively low temperature after thermal aging.

The addition of an Fe-compound to the fresh NSR catalyst does not influence the NSR activity, as we have seen above. We may say that the effect of addition of an Fe-compound was not observed because the fresh NSR catalyst shows sufficient NSR activity derived from enough active sites to negate the role of the Fe-compound.

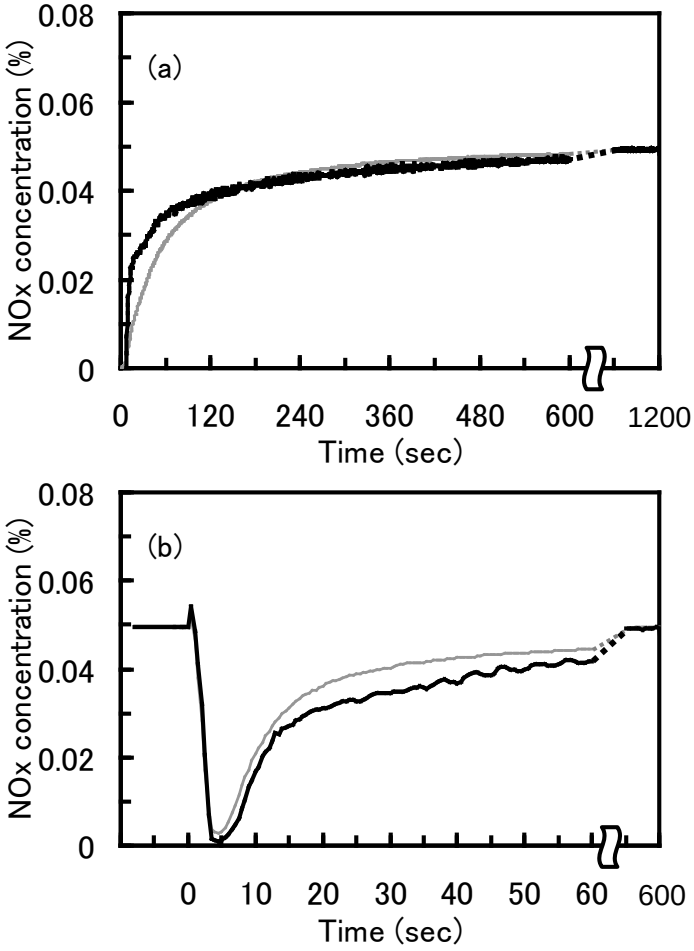

Fig. 6. Outlet NO_x concentration profiles at 623 K over an aged Pt/Ba/(Al_2O_3-CeO_2-Fe_2O_3) catalyst with 6.6 wt.% Fe_2O_3 loading (black line) and an aged Pt/Ba/(Al_2O_3-CeO_2) catalyst (gray line), (a) when exposed to an oxidizing feedstream after exposure to a feedstream of 3% H_2 in N_2 at 673 K for 10 minutes to regenerate from stored NO_x, (b) when subsequently exposed to a reducing feedstream with CO as a reducing agent for 3 seconds, followed by an oxidizing feedstream.

3.4. Status of Pt and Fe-compound on NSR catalysts

In order to look closely at the CO self-poisoning for the CO-O_2 reaction and the CO-NO reaction under reducing conditions, the status of Pt and an Fe-compound was investigated on the aged Pt/Ba/(Al_2O_3-CeO_2-Fe_2O_3) catalysts and the aged Pt/Ba/(Al_2O_3-CeO_2) catalyst, because the CO self-poisoning was regarded to occur on these two active components. The status of Pt could be directly observed through XRD analysis, while the status of an Fe-compound is hard to be accessed simply from XRD patterns. Fig. 7 shows the lattice constant of Pt on the aged catalysts as a function of the amount of Fe_2O_3 loading. The larger was the amount of Fe_2O_3 loading, the smaller was

the lattice constant of Pt. The lattice constant of Pt on the aged Pt/Ba/(Al_2O_3-CeO_2) catalyst matches with that of the pure Pt (cubic system) in the literature (PDF# 4-802). These results indicate that Pt reacts with an Fe-compound to form a Pt-Fe alloy in the aged catalysts. The lattice constant of Pt_3Fe (cubic system) in the literature (PDF# 29-716) is listed in Fig. 7. We can estimate the molar fractions of Fe in a Pt-Fe alloy using Vegard's rule with the lattice constants of Pt and Pt_3Fe, and the ratios of Ft-atoms in a Pt-Fe alloy to the whole Fe-atoms on the aged Pt/Ba/(Al_2O_3-CeO_2-Fe_2O_3) catalysts with different Fe_2O_3 loadings. Table 7 shows the results of these estimations. These results indicate that a very small portion of an Fe-compound reduces to Fe and forms a Pt-Fe alloy in the aged Pt/Ba/(Al_2O_3-CeO_2-Fe_2O_3) catalysts. Fig. 8 (a) shows the XPS spectra in the region of the $Pt4d_{5/2}$ emission band of the aged catalysts. All of the peak positions in the region of the $Pt4d_{5/2}$ emission are almost the same and could be ascribed to the metallic Pt. Fig. 8 (b) shows the XPS spectra in the region of the $Fe2p_{3/2}$ emission band of the aged catalysts. All of the peak positions in the region of the $Fe2p_{3/2}$ emission are also almost the same and could be ascribed to Fe_2O_3. These results indicate that a large portion of an Fe-compound remains as Fe_2O_3, which is a starting material. These results are, therefore, consistent with results through XRD analysis. We have already said that an Fe-compound on the Pt/Ba/(Al_2O_3-CeO_2-Fe_2O_3) catalysts acts at a store for oxygen at 523 K. Thus, we may say that Fe_2O_3 is changed to Fe_3O_4, FeO or/and Fe under reaction conditions, as shown in equation (2).

$$1/2\ Fe_2O_3 \Leftrightarrow 1/3\ Fe_3O_4 + 1/12\ O_2 \Leftrightarrow FeO + 1/4\ O_2 \Leftrightarrow Fe + 3/4\ O_2 \text{ -------- (2)}$$

It was reported that CO adsorbed on a precious metal can react with oxygen from CeO_2, as shown by the temperature-programmed desorption of adsorbed CO over CeO_2-supported precious metal catalysts [29-31]. In a similar manner, it is likely that CO adsorbed on Pt can react with oxygen from an Fe-compound, which acts as a store for oxygen more effectively than does CeO_2. In addition, it is likely that Fe in the Pt-Fe alloy causes oxygen to react with CO absorbed on neighboring Pt via the temporary formation of Fe-oxides on the surface of the Pt-Fe alloy. Although further consideration of the status of Pt and an Fe-compound on the Pt/Ba/(Al_2O_3-CeO_2-Fe_2O_3) catalysts is needed, we may reasonably conclude that an Fe-compound on the aged Pt/Ba/(Al_2O_3-CeO_2-Fe_2O_3) catalysts in the form of Fe_2O_3 or/and Fe in a Pt-Fe alloy provides oxygen to CO adsorbed on the metallic Pt, causing suppression of the CO self-poisoning for the CO-O_2 reaction and the CO-NO reaction under reducing conditions after thermal aging.

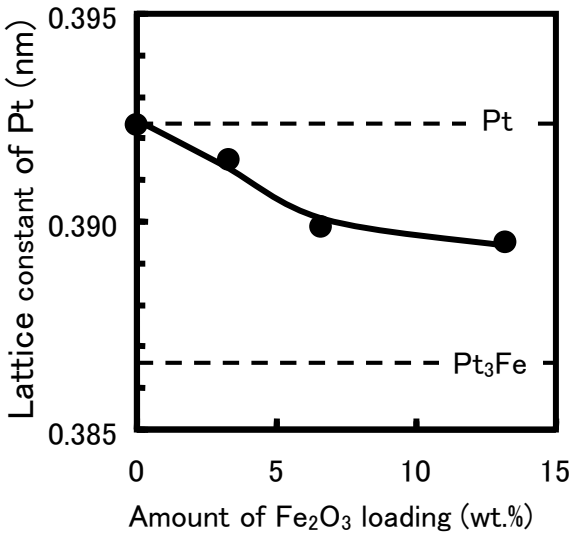

Fig. 7. Lattice constant of Pt on aged Pt/Ba/(Al_2O_3-CeO_2-Fe_2O_3) catalysts with different amounts of Fe_2O_3 loading and a Pt/Ba/(Al_2O_3-CeO_2) catalyst as a function of the amount of Fe_2O_3 loading.

Table 7. The amounts of Fe-atoms in a Pt-Fe alloy on the aged Pt/Ba/(Al_2O_3-CeO_2-Fe_2O_3) catalysts

Amount of Fe_2O_3 loading (wt.%)	Mol fraction of Fe in a Pt-Fe alloy (at.%)	Ratio of Fe-atoms in a Pt-Fe alloy to whole Fe-atoms (at.%)
3.3	4.0	0.4
6.6	10.4	0.6
13.2	12.3	0.4

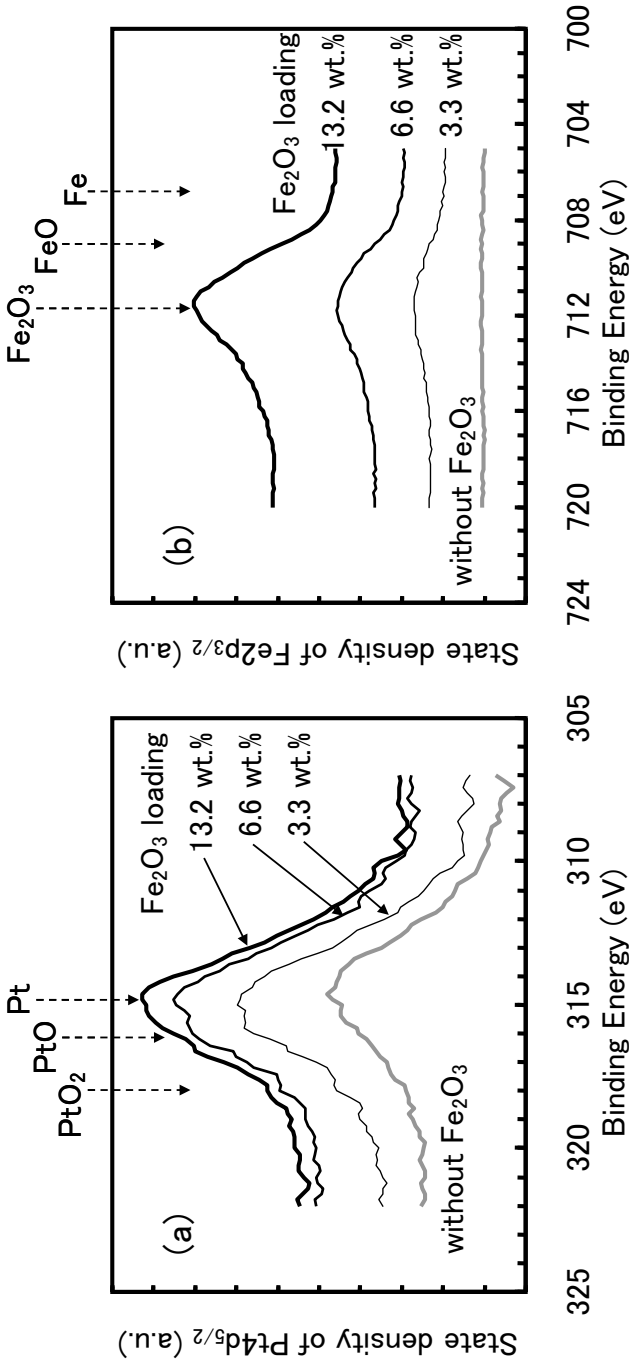

Fig. 8. XPS spectra in the region of the (a) $Pt4d_{5/2}$ emission band and (b) $Fe2p_{3/2}$ emission band of aged $Pt/Ba/(Al_2O_3\text{-}CeO_2\text{-}Fe_2O_3)$ catalysts with different amounts of Fe_2O_3 loading and an aged $Pt/Ba/(Al_2O_3\text{-}CeO_2)$ catalyst.

4. Conclusions

The effect of addition of an Fe-compound to a NO_x storage-reduction catalyst (NSR catalyst) on its NO_x purification activity through storage-reduction (NSR activity) was studied by comparison between Pt/Ba/(Al_2O_3-CeO_2-Fe_2O_3) and Pt/Ba/(Al_2O_3-CeO_2) catalysts to improve the durability against thermal deterioration.

The fresh Pt/Ba/(Al_2O_3-CeO_2-Fe_2O_3) catalyst showed the same NSR activity as did the fresh Pt/Ba/(Al_2O_3-CeO_2) catalyst, when either C_3H_6 or CO as a reducing agent. On the other hand, after thermal aging at 1123 K, the aged Pt/Ba/(Al_2O_3-CeO_2-Fe_2O_3) catalyst showed a higher NSR activity when using CO as a reducing agent at a relatively low temperature (up to 573 K) than did the aged Pt/Ba/(Al_2O_3-CeO_2) catalyst. However, there was no significant difference in the NSR activity between the two aged catalysts when using C_3H_6 as a reducing agent.

The data obtained from the reaction analysis of simple binary gas systems and XRD measurements show that the Fe-compound on the aged Pt/Ba/(Al_2O_3-CeO_2-Fe_2O_3) catalyst weakens the CO self-poisoning for the CO-O_2 and CO-NO reactions under reducing conditions, probably by provision of oxygen to the CO from Fe_2O_3 or/and Fe in a Pt-Fe alloy. The weaker CO self-poisoning for the CO-O_2 and CO-NO reactions can account for the higher ability to reduce stored NO_x by CO under reducing conditions, causing a greater NSR activity when using CO as a reducing agent at a relatively low temperature.

Acknowledgements

We wish to thank our colleagues Mr. Kazuhiko Dohmae and Ms. Kae Yamamura for the XPS measurements and for the OSC measurements, respectively.

References

[1] R.M. Heck, R.J. Ferrauto, Catalytic Air Pollution Control, Van Nostrand Reinhold, New York, 1995.
[2] W. Held, A. König, T. Richter, L.Puppe, SAE paper 900496 (1990).
[3] S. Sato, Y. Yu-u, H. Yahiro, N. Mizuno, M. Iwamoto, Appl. Catal. 70 (1991) L1.
[4] Y. Fujitani, H. Muraki, S. Kondoh, M. Fukui, Ger. Offen. DE3735151 (1988).
[5] Y. Kintaichi, H. Hamada, M. Tabata, M. Sasaki, T. Ito, Catal. Lett. 6 (1990) 239.
[6] H. Hamada, Y. Kintaichi, M. Sasaki, T. Ito, M. Tabata, Appl. Catal. 75 (1991) L14.
[7] A. Takami, T. Takemoto, S. Ichikawa, F. Saito, K. Komatsu, JSAE Spring Convention Proceedings, 9433858 (1994).
[8] M. Matsumoto, K. Yokota, H. Doi, K. Kimura, K. Sekizawa, S. Kasahara, Catal.

Today 22 (1994) 127.
[9] R. J. Ferrauto, R. M. Heck, Catal. Today 55 (2000) 179.
[10] N. Miyoshi, S. Matsumoto, K. Katoh, T. Tanaka, J. Harada, N. Takahashi, K. Yokota, M. Sugiura, K. Kasahara, SAE paper 950809 (1995).
[11] N. Takahashi, H. Shinjoh, T. Iijima, T. Suzuki, K. Yamazaki, K. Yokota, H. Suzuki, N. Miyoshi, S. Matsumoto, T. Tanizawa, T. Tanaka, S. Tateishi, K. Kasahara, Catal. Today, 27 (1996) 63.
[12] S. Matsumoto, Catal. Today 29 (1996) 43.
[13] H. Shinjoh, N. Takahashi, K. Yokota, M. Sugiura, Appl. Catal. B 15 (1998) 189
[14] M.S. Brogan, R.J. Brisley A.P. Walker, D.E. Webster, W. Boegner, N.P. Fekete, M. Kramer, B. Krutzsch, D. Voigtiander, SAE paper 952490 (1995).
[15] W. Boegner, M. Kramer, B. Krutzsch, S. Pischinger, D. Voigtlander, G. Wenninger, F. Wirbeleit, M.S. Brogan, R.J. Brisley, D.E. Webster, Appl. Catal. B 7 (1995) 153
[16] E. Fridell, M. Skoglundh, S. Johansson, B. Westerberg, A. Torncrona, G. Smedler, Stud. Surf. Sci. Catal. 116 (1998) 537.
[17] E. Fridell, M. Skoglundh, B. Westerberg, S. Johansson, G. Smedler, J. Catal. 183 (1999) 196.
[18] S. Hodjati, P. Bernhardt, C. Petit, V. Pitchon, A. Kiennemann, Appl. Catal. B 19 (1998) 209.
[19] S. Hodjati, P. Bernhardt, C. Petit, V. Pitchon, A. Kiennemann, Appl. Catal. B 19 (1998) 219.
[20] H. Mahzoul, J.F. Brilhac, P. Gilot, Appl. Catal. B 20 (1999) 47.
[21] S. Matsumoto, Y. Ikeda, H. Suzuki, M. Ogai, N. Miyoshi, Appl. Cat. B 25 (2000) 115.
[22] H. Hirata, I. Hachisuka, Y. Ikeda, S. Tsuji, S. Matsumoto, Top. Catal. 16/17 (2001) 145.
[23] H. Y. Huang, R.Q. Long, R.T. Yang, Appl. Cat. B 33 (2001) 127.
[24] A. Amberntsson, M. Skoglundh, S. Ljungstrom, E. Fridell, J. Catal. 217 (2003) 253.
[25] K. Yamazaki, T. Suzuki, N. Takahashi, K. Yokota, M. Sugiura, Appl. Catal. B 30 (2001) 459.
[26] P. T. Fanson, M. R. Horton, W. N. Delgass, J. Lauterbach, Appl. Catal. B 46 (2003) 393.
[27] H. Muraki, K. Yokota, Y. Fujitani, Appl. Catal. 48 (1989) 93.
[28] H. Shinjoh, H. Muraki, Y. Fujitani, Appl. Catal. 49 (1989) 195.
[29] T. Jin, T. Okuhara, G. J. Mains, J. M. White, J. Phys. Chem. 91 (1987) 3310.

[30] G. S. Zafiris, R. J. Gorte, J. Catal. 139 (1993) 561.
[31] H. Cordatos, R. J. Gorte, J. Catal. 139 (1996) 112

Chapter 4

Improved three-way catalytic performance of NO_x storage-reduction catalyst

Abstract

The three-way catalytic (TWC) performance of NO_x storage-reduction catalyst (NSR catalyst) was investigated over a Pt/Ba/(Al_2O_3-CeO_2-Fe_2O_3) catalyst and compared with a Pt/Ba/(Al_2O_3-CeO_2) catalyst. For fresh catalysts, the TWC performances of these catalysts were almost equal. However, after thermal aging at 1123K, the TWC performance of the aged former catalyst was higher than that of the aged latter one.

X-ray diffraction measurements showed that there is no difference in the Pt and CeO_2 particle size between the aged Pt/Ba/(Al_2O_3-CeO_2-Fe_2O_3) catalyst and aged Pt/Ba/(Al_2O_3-CeO_2) catalyst. However, the thermogravimetric analysis showed that the oxygen storage-release capacity (OSC) of the aged former catalyst was far greater than that of the aged latter one. Therefore, the Fe-compound on a Pt/Ba/(Al_2O_3-CeO_2-Fe_2O_3) catalyst has been proved to increase the OSC of the aged catalyst, resulting in high TWC performance after thermal aging.

Keywords: Lean-burn engine, NO_x storage-reduction catalyst (NSR catalyst), Three-way catalytic performance (TWC performance), Thermal aging, Platinum, Barium, Alumina, Cerium oxide, Iron oxide

1. Introduction

The lean-burn engine system has been one of the key technologies for suppressing the fuel consumption of vehicles. Accordingly, NO_x purification under oxidizing conditions was a key issue in meeting more stringent regulations. Many studies have been carried out on many kinds of catalysts for the selective catalytic reduction (SCR) of NO_x under oxidizing conditions, e.g., copper ion-exchanged zeolites (Cu-ZSM-5) [1-3], base metals supported on alumina [4], and precious metals supported on zeolites [5]. However, these catalysts have many problems for practical use such as low activity, a narrow temperature window and insufficient durability [6]. Many such problems have been solved by a new concept, 'the NO_x storage-reduction catalyst (NSR catalyst)', having the ability to store NO_x under oxidizing conditions and to reduce the stored NO_x

under reducing conditions [7,8]. However, a shortcoming of the NSR catalysts is the deterioration by SO_2 derived from sulfur in the fuel under engine operating conditions. In a previous paper, we reported that the addition of an Fe-compound to the NSR catalyst improves its NO_x purification ability in the presence of SO_2 under oxidizing conditions [9].

In the development process of the NSR catalyst, we have found that the addition of an Fe-compound to the NSR catalyst improves the durability against sulfur poisoning and thermal deterioration. On the other hand, the NSR catalyst needs the three-way catalytic performance (TWC performance) under stoichiometric or near-stoichiometric conditions as well as NO_x purification activity through storage-reduction, because the lean-burn engine system partially operates under stoichiometric conditions when more power is required. In this study, we investigated the effect of the addition of an Fe-compound to the NSR catalyst on its TWC performance after thermal aging, and clarified the role of the Fe-compound in improving the TWC performance of the Pt/Ba/(Al_2O_3-CeO_2-Fe_2O_3) catalyst.

2. Experimental

2.1. Catalyst preparation

The Pt/Ba/(Al_2O_3-CeO_2-Fe_2O_3) catalyst was prepared using a two-step wet impregnation method. Firstly, powdery γ-Al_2O_3 (Nikki Universal, 150 m^2/g) was blended with powdery CeO_2 (Wako Pure Chemical Industries, 120 m^2/g), and Fe_2O_3 (Wako Pure Chemical Industries) in distilled water and contacted with an aqueous solution containing $Pt(NH_3)_2(NO_2)_2$ (Tanaka Precious Metals), followed by drying at 393 K for 12 h and by calcination at 773 K for 3 h in air. The resultant powdery product was then contacted with an aqueous solution containing $Ba(CH_3COO)_2$ (Wako Pure Chemical Industries), followed by drying at 393 K for 12 h and by calcination at 773 K for 3 h in air. The amount of Pt, BaO and CeO_2 was respectively 0.83, 19.1, and 20.4 wt.% of the catalyst. The amount of Fe_2O_3 was 3.3, 6.6(mainly), or 13.2 wt.% of the catalyst.

The Pt/Ba/(Al_2O_3-CeO_2) catalyst was prepared in the same way as described above except that powdery Fe_2O_3 was not used. The amount of Pt, BaO and CeO_2 was respectively 0.83, 19.1, and 20.4 wt.% of the catalyst, which was equal to that of the Pt/Ba/(Al_2O_3-CeO_2-Fe_2O_3) catalyst.

The prepared catalysts were pressed into disks and pulverized to a 0.17 - 0.28 cm size in diameter for use in catalyst aging treatment and catalytic activity measurements.

2.2. Catalyst aging treatment

A thermal aging treatment was performed by placing a 10.0 g catalyst sample in the center of a tube furnace and downstream from a heat exchange zone. A constant treatment temperature was maintained using a thermocouple placed just above the catalyst bed.

The catalyst was exposed to a cycled feedstream simulating a stoichiometric engine exhaust gas at 1123 K for 5 h. Table 1 shows the composition of the cycled feedstream, which alternately changes between oxidizing and reducing conditions every 5 minutes. The feedstream was passed into the catalyst bed at a gas flow rate of 1,000 cm^3/min.

Table 1. Gas compositions for thermal aging

Condition	Concentration (vol.%)							
	C_3H_6	CO	H_2	NO	O_2	CO_2	H_2O	N_2
Oxidizing	0.067	0.075	0.025	0.12	1.20	10.0	3.0	bal.
Reducing	0.067	1.50	0.50	0.12	0.25	10.0	3.0	bal.

2.3. Catalytic activity measurements

Catalytic activity data were obtained using a conventional fixed-bed flow reactor system at atmospheric pressure, equipped with mass flow controllers and injector valves to obtain a premixed feedstream of desired composition, simulating the various air-to-fuel ratios (A/F ratios) of the engine exhaust gas. This apparatus can deliver a cycled feedstream to simulate the dynamic behavior of an engine exhaust gas. The stoichiometry number, S, used to identify the redox characteristic of the feedstreams, which is related to the A/F ratio of the engine exhaust gas, is defined as follows:

$$S = (2[O_2] + [NO]) / ([H_2] + [CO] + 9[C_3H_6])$$

When S<1.0, S=1.0, and S>1.0, the redox characters of the feedstream are net reducing, stoichiometric, and net oxidizing, respectively. A quartz tube with an inner diameter of 3.0 cm was chosen as the reactor tube. A 10.0 g catalyst (about 20 cm^3) was placed on a quartz filter in the middle part of the reactor. The upper part of the catalyst bed was packed with 200 cm^3 of inactive quartz spheres (0.3 cm in diameter) for preheating the feed gas. The furnace temperature was controlled within a maximum variation of 2 K by

an automatic temperature controller. The gas leaving the reactor was fed to a condenser to remove the water vapor. The remaining components were continuously analyzed by a nondispersive infrared spectrophotometer (CO and CO_2), a flame ionization detector (hydrocarbon, HC), magnetic susceptibility (O_2), and chemiluminescence (NO_x) equipped with an automotive gas analyzer (Best-Sokki, CATA-5000).

Two experiments were carried out in the TWC performance measurements; light-off performance and conversion efficiencies as a function of the S. Light-off performance was measured with a cycled feedstream of time-averaged S=1.0 and a 5 K/min heating rate of the reactor. Table 2 shows the composition of the cycled feedstream, which alternately changes between oxidizing and reducing conditions every second. Conversion efficiencies as a function of the S value were measured at 623 K. The S values were varied from 0.36 to 1.65, simulating A/F ratios from 14.0 to 14.9. The flow rate of these simulated feedstreams in the above experiments was kept at 30,000 cm^3/min, resulting in a space velocity of about 90,000 h^{-1}.

Table 2. Gas compositions for the measurement of light-off performance

Condition	Concentration (vol.%)							
	C_3H_6	CO	H_2	NO	O_2	CO_2	H_2O	N_2
Oxidizing	0.053	0.72	0.24	0.12	1.40	8.0	5.0	bal.
Reducing	0.053	1.83	0.61	0.12	0.65	8.0	5.0	bal.

2.4. Catalyst Characterization

The BET surface area was measured by N_2 adsorption at liquid nitrogen temperature using a conventional flow-type adsorption apparatus.

X-ray diffraction (XRD) measurement was carried out with a Rigaku RINT-2100 X-ray diffractometer using Cu Kα radiation. The samples of catalyst powder were pressed and loaded on a sample holder at a depth of 0.1 cm. Calculation of the crystalline particle size was done using the diffraction line width in Scherrer's equation with the Gaussian line shape approximation.

The oxygen storage-release capacity (OSC) was measured using thermogravimetric analysis. The OSC was calculated from the weight gain and loss of the catalyst alternately exposed to an oxidizing gas (50% O_2 in N_2) and a reducing gas (20% H_2 in N_2) every 5 minutes at 523 K.

3. Results and Discussion

3.1. Three-way catalytic performance (TWC performance)

The TWC performance of a Pt/Ba/(Al_2O_3-CeO_2-Fe_2O_3) catalyst with 6.6 wt.% Fe_2O_3 loading was compared with that of a Pt/Ba/(Al_2O_3-CeO_2) catalyst. Fig. 1 shows the light-off performances of the two fresh catalysts. The light-off performance of the fresh Pt/Ba/(Al_2O_3-CeO_2-Fe_2O_3) catalyst was almost the same as that of the fresh Pt/Ba/(Al_2O_3-CeO_2) catalyst. Above 500 K, both catalysts showed high conversions of HC, CO and NO_x (>96% for all components) in a cycled feedstream, which fluctuated between oxidizing and reducing conditions every second.

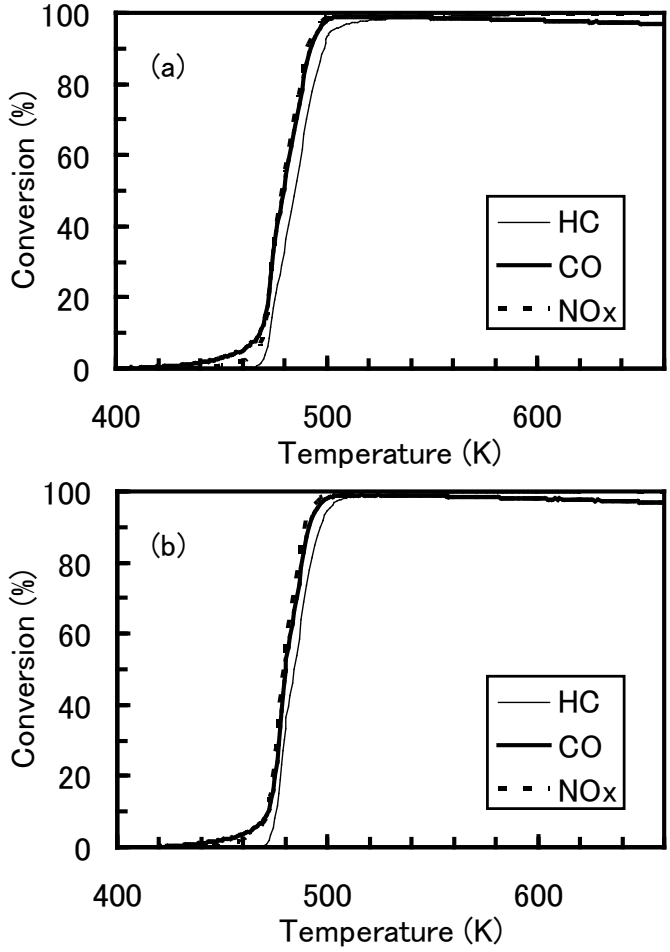

Fig. 1. Light-off performance in a cycled feedstream of a time-averaged stoichiometric composition with a 5 K/min heating rate over fresh catalysts (a) Pt/Ba/(Al_2O_3-CeO_2-Fe_2O_3) with 6.6 wt.% Fe_2O_3 loading and (b) Pt/Ba/(Al_2O_3-CeO_2).

Three-way catalysts generally cannot convert HC and CO effectively under static reducing conditions due to the lack of oxygen, and NO_x under static oxidizing conditions due to the lack of reducing agents. For high conversions of all HC, CO and NO_x in such a cycled feedstream, it is necessary to compensate for the fluctuations between oxidizing and reducing conditions over the catalysts. Therefore, this result indicates that both fresh catalysts have a great ability to compensate for the fluctuation between oxidizing and reducing conditions. Fig. 2 shows the conversion efficiencies as a function of S at 623 K on the two fresh catalysts. The activities for HC, CO and NO_x under the reducing and oxidizing conditions of the former catalyst were almost the same as those of the latter. Therefore, the addition of an Fe-compound to the fresh NSR catalyst does not influence the TWC performance significantly.

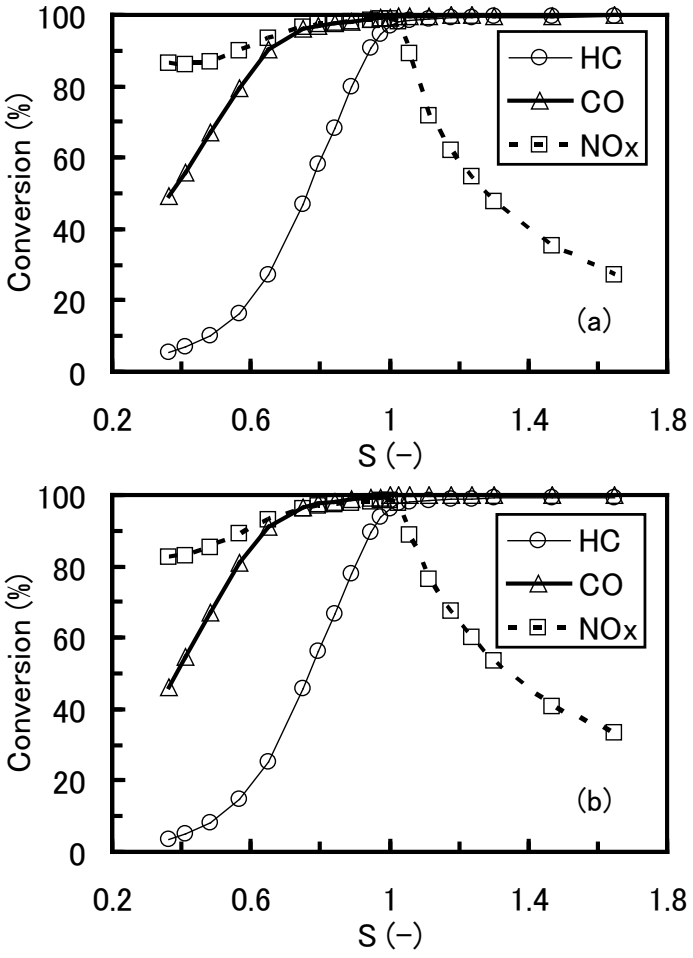

Fig. 2. Conversion efficiencies as a function of the stoichiometric number (S) at 623 K for fresh catalysts (a) Pt/Ba/(Al_2O_3-CeO_2-Fe_2O_3) with 6.6 wt.% Fe_2O_3 loading and (b) Pt/Ba/(Al_2O_3-CeO_2).

Fig. 3 shows the light-off performances of the two aged catalysts after thermal aging at 1123 K. HC, CO and NO_x over the aged Pt/Ba/(Al_2O_3-CeO_2-Fe_2O_3) catalyst were converted at a lower temperature compared with that over the aged Pt/Ba/(Al_2O_3-CeO_2) catalyst, that is, the light-off performance of the former catalyst was higher than that of the latter. In addition, the activity for CO and NO_x above 570 K of the aged Pt/Ba/(Al_2O_3-CeO_2-Fe_2O_3) catalyst was higher than that of the aged Pt/Ba/(Al_2O_3-CeO_2) catalyst; that is, the ability of the former catalyst to compensate for the fluctuations between oxidizing and reducing conditions was higher than that of the latter catalyst.

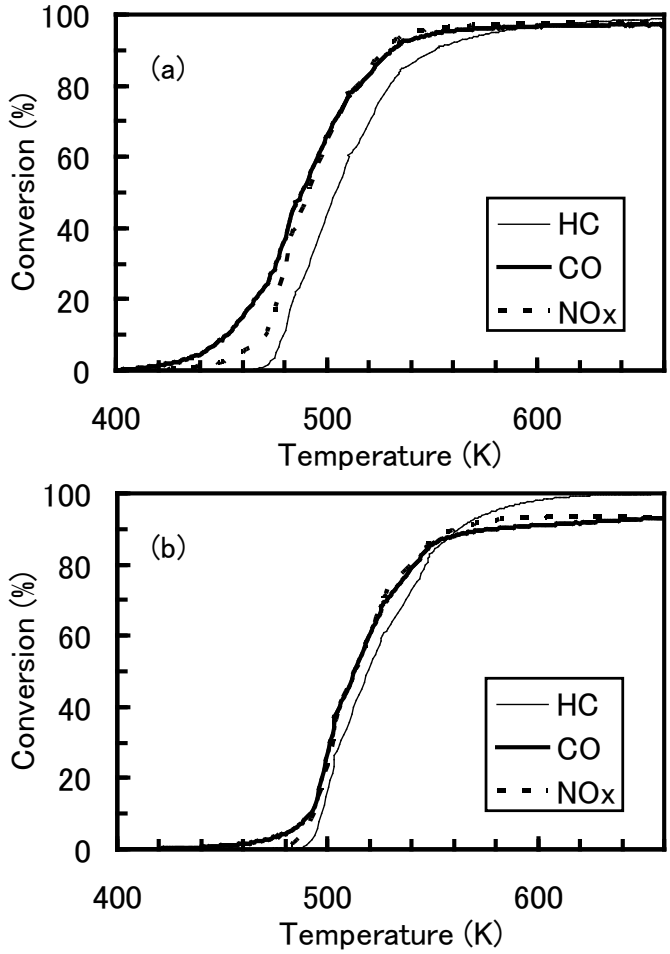

Fig. 3. Light-off performance in a cycled feedstream of a time-averaged stoichiometric composition with a 5 K/min heating rate over aged catalysts (a) Pt/Ba/(Al_2O_3-CeO_2-Fe_2O_3) with 6.6 wt.% Fe_2O_3 loading and (b) Pt/Ba/(Al_2O_3-CeO_2), after thermal aging at 1123 K.

Fig. 4 shows the conversion efficiencies as a function of S at 623 K on the two aged catalysts. The activity for NO_x and CO under reducing conditions of the aged Pt/Ba/(Al_2O_3-CeO_2-Fe_2O_3) catalyst was higher than that of the aged Pt/Ba/(Al_2O_3-CeO_2) catalyst. It should be noted that the activity for NO_x decreased with a decrease in S value under reducing conditions at 623 K over the latter catalyst. Thus we can see that the addition of an Fe-compound to the aged NSR catalyst improves (1) the light-off performance under stoichiometric conditions, (2) the ability to compensate for the fluctuations between oxidizing and reducing conditions at relatively high temperature (above 570 K), and (3) the activity for NO_x and CO under reducing conditions, after thermal aging at 1123 K.

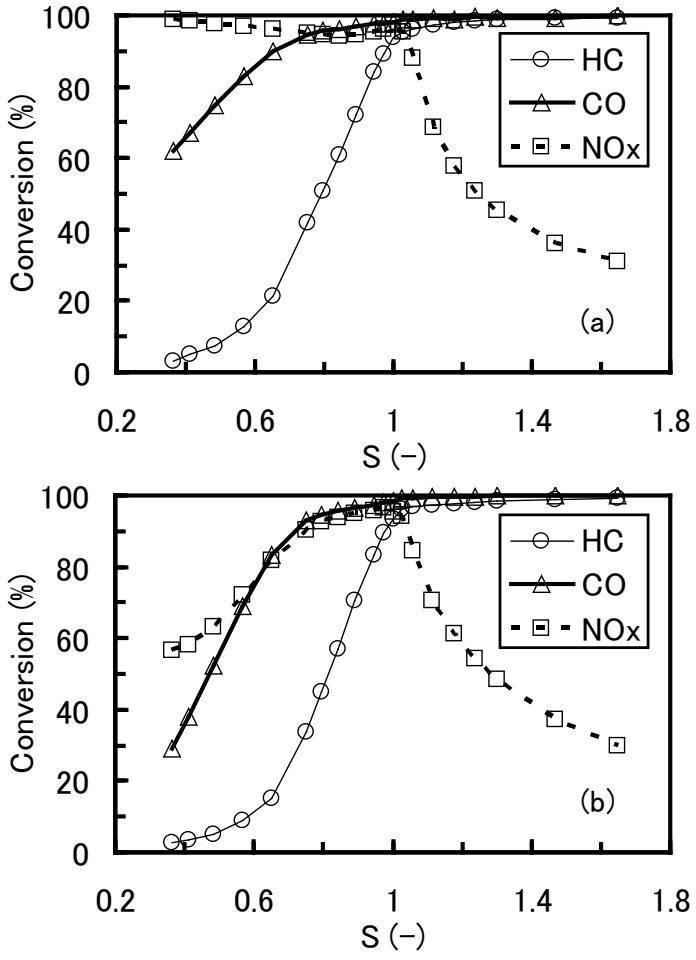

Fig. 4. Conversion efficiencies as a function of the stoichiometric number (S) at 623 K for aged catalysts (a) Pt/Ba/(Al_2O_3-CeO_2-Fe_2O_3) with 6.6 wt.% Fe_2O_3 loading and (b) Pt/Ba/(Al_2O_3-CeO_2), after thermal aging at 1123 K.

3.2. Role of Fe-compound in TWC performance

For both fresh and aged catalysts, the surface areas of all Pt/Ba/(Al_2O_3-CeO_2-Fe_2O_3) catalysts were lower than that of a Pt/Ba/(Al_2O_3-CeO_2) catalyst (see Table 3 in Chapter 3). However, the decrease in the BET surface area caused by the thermal aging of the former catalysts was almost equal to that of the latter catalyst. There was no significant difference in the Pt particle sizes among all of the aged catalysts (see Table 4 in Chapter 3). Therefore, the addition of an Fe-compound to a Pt/Ba/(Al_2O_3-CeO_2) catalyst does not influence the thermal stability of the support materials and Pt during thermal aging at 1123 K.

First, in order to clarify the role of an Fe-compound in the ability to compensate for the fluctuations between oxidizing and reducing conditions after thermal aging, the oxygen storage-release capacity (OSC) of the Pt/Ba/(Al_2O_3-CeO_2-Fe_2O_3) catalysts with different amounts of Fe_2O_3 loading and the Pt/Ba/(Al_2O_3-CeO_2) catalyst was measured. Fig. 5 shows the OSC at 523 K of the fresh and aged catalysts as a function of the amount of Fe_2O_3 loading. There were good linear correlations between these two parameters for the fresh and aged catalysts. These results indicate that an Fe-compound in the fresh and aged Pt/Ba/(Al_2O_3-CeO_2-Fe_2O_3) catalysts acts to store oxygen, i.e., it takes up oxygen under oxidizing conditions and releases oxygen under reducing conditions. It is well-known that CeO_2 also acts to store oxygen. If the Fe-compound and CeO_2 have contributed to the OSC of the catalyst independently by following equations,

$$1/2\ Fe_2O_3 \Leftrightarrow 1/3\ Fe_3O_4 + 1/12\ O_2 \Leftrightarrow FeO + 1/4\ O_2 \Leftrightarrow Fe + 3/4\ O_2 \text{ -------- (1)}$$

$$CeO_2 \Leftrightarrow 1/2\ Ce_2O_3 + 1/4\ O_2 \text{ -------- (2)}$$

the gradients and the intercepts of the linear correlations in Fig. 5 would estimate that 1mol of Fe and Ce on the fresh catalysts showed an OSC of 0.064 and 0.034 mol-O_2, respectively, and 1mol of Fe and Ce on the aged catalysts showed an OSC of 0.063 and 0.015 mol-O_2, respectively. These estimations suggest that the Fe-compound presents a higher OSC and a smaller decrease in OSC caused by thermal aging than does CeO_2. It should be concluded, from what has been said above, that an Fe-compound on the aged Pt/Ba/(Al_2O_3-CeO_2-Fe_2O_3) catalysts acts to store oxygen more effectively than does CeO_2, causing improvement of the ability to compensate for the fluctuations between oxidizing and reducing conditions after thermal aging at 1123 K.

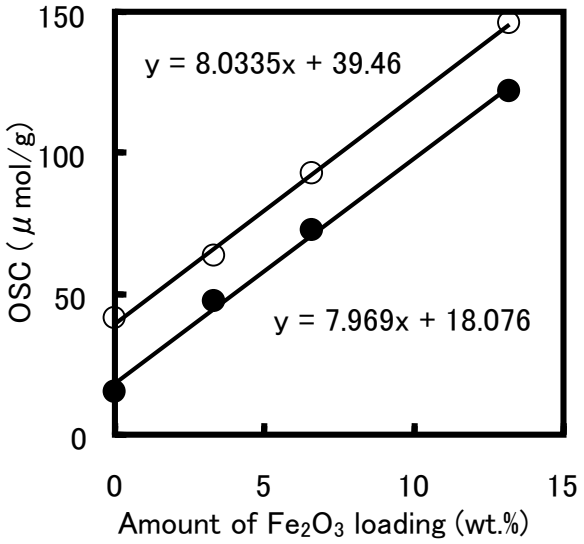

Fig. 5. Oxygen storage-release capacity at 573 K of fresh (○) and aged (●) Pt/Ba/(Al_2O_3-CeO_2-Fe_2O_3) catalysts with different amounts of Fe_2O_3 loading and a Pt/Ba/(Al_2O_3-CeO_2) catalyst, as a function of the amount of Fe_2O_3 loading.

Next, in order to clarify the role of an Fe-compound in the light-off performance under a stoichiometric condition after thermal aging, simple binary gas reaction systems, which are elementary reactions in the three-way catalytic reaction, were investigated on the aged Pt/Ba/(Al_2O_3-CeO_2-Fe_2O_3) catalyst with 6.6 wt.% Fe_2O_3 loading and the aged Pt/Ba/(Al_2O_3-CeO_2) catalyst (see Fig. 5 in Chapter 3). CO in the CO-O_2 reaction and CO in the CO-NO reaction over the aged Pt/Ba/(Al_2O_3-CeO_2-Fe_2O_3) catalyst were converted at far lower temperatures than over the aged Pt/Ba/(Al_2O_3-CeO_2) catalyst, although C_3H_6 in the C_3H_6-O_2 reaction over the former catalyst was converted at a slightly higher temperature than over the latter catalyst. In addition, CO in the CO-O_2 reaction was converted at the lowest temperature of all reactions over each catalyst. This result suggests that the CO-O_2 reaction is a rate-determining step of the three-way catalytic reaction at low temperatures, where the light-off over the catalyst occurs.

The kinetics of the CO-O_2 reaction was subjected to empirical laws: the rate of carbon dioxide formation, v, is generally expressed by the following equation:

$$v = k \times P_{CO}^{m} \times P_{O2}^{n} \times \exp(-\Delta E / RT)$$

where P_{CO} and P_{O2} are the partial pressures of CO and O_2 and the partial reaction orders m and n are derived from data obtained under conditions of low conversion, usually less than 30 %. The range of P_{CO} and P_{O2} are respectively 1.0-6.0 % and 0.2-1.5 %. The

values of m and n were determined from a conventional log-log relation between rate and partial pressures of the respective species at about 473 K (see Table 5 in Chapter 3). The reaction order with respect to CO partial pressure, m, over the aged Pt/Ba/(Al_2O_3-CeO_2-Fe_2O_3) catalyst was of negative order (–0.2), but its absolute value was smaller than that of the aged Pt/Ba/(Al_2O_3-CeO_2) catalyst (–1.0). The reaction order with respect to O_2 partial pressure, n, over the former catalyst was of positive order, which was almost equal to that of the latter catalyst. The negative order with CO and the positive order with O_2 suggest that CO is adsorbed strongly on the catalyst surface, causing CO self-poisoning for the CO-O_2 reaction. The smaller absolute value of the negative reaction order with respect to CO partial pressure over the aged Pt/Ba/(Al_2O_3-CeO_2-Fe_2O_3) catalyst compared with that over the aged Pt/Ba/(Al_2O_3-CeO_2) catalyst suggests that the CO self-poisoning over the former catalyst is weaker than that over the latter catalyst. We may therefore reasonably conclude that an Fe-compound on the aged Pt/Ba/(Al_2O_3-CeO_2-Fe_2O_3) catalysts weakens the CO self-poisoning for the CO-O_2 reaction, causing improvement in the light-off performance under stoichiometric conditions after thermal aging.

Lastly, as for the activity for NO_x and CO under reducing conditions, Shinjoh et al. studied the NO-CO reaction over Pt, Pd and Rh catalysts and demonstrated that CO inhibits NO reduction strongly over Pt catalyst because of CO self-poisoning [10]. The reaction analysis of the CO-NO reaction under reducing conditions over the aged Pt/Ba/(Al_2O_3-CeO_2-Fe_2O_3) catalyst with 6.6 wt.% Fe_2O_3 loading and the aged Pt/Ba/(Al_2O_3-CeO_2) catalyst was also conducted using the following equation, as well as that of the CO-O_2 reaction:

$$v = k \times P_{CO}^{m} \times P_{NO}^{n} \times \exp(-\Delta E / RT)$$

where v is the rate of carbon dioxide formation, P_{CO} and P_{NO} are the partial pressures of CO and NO and the partial reaction orders m and n are derived from data obtained under conditions of low conversion. The range of P_{CO} and P_{NO} are respectively 0.24-0.96% and 0.12-0.48% (see Table 6 in Chapter 3). The reaction order with respect to CO partial pressure, m, over the aged Pt/Ba/(Al_2O_3-CeO_2-Fe_2O_3) catalyst was of negative order (–0.7), but its absolute value was smaller than that of the aged Pt/Ba/(Al_2O_3-CeO_2) catalyst (–1.5). The reaction order with respect to NO partial pressure, n, over the former catalyst was of positive order, as well as that of the latter catalyst. The negative order with CO and the positive order with NO suggest that CO is adsorbed strongly on the catalyst surface, causing CO self-poisoning for the CO-NO

reaction. The smaller absolute value of the negative reaction order with respect to CO partial pressure over the aged Pt/Ba/(Al_2O_3-CeO_2-Fe_2O_3) catalyst compared with that over the aged Pt/Ba/(Al_2O_3-CeO_2) catalyst suggests that the CO self-poisoning for the CO-NO reaction over the former catalyst is weaker than that over the latter catalyst. Therefore, it seems reasonable to conclude that an Fe-compound on the aged Pt/Ba/(Al_2O_3-CeO_2-Fe_2O_3) catalyst weakens the inhibition of the NO_x reduction by CO self-poisoning, causing improvement in the activity for NO_x and CO under reducing conditions after thermal aging.

The addition of an Fe-compound to the fresh NSR catalyst does not influence the TWC performance, as we have seen above. We cannot say, however, that the Fe-compound plays no role in acting as a store for oxygen and weakening the CO self-poisoning for the CO-O_2 reaction and the CO-NO reaction on the fresh catalyst. The Pt particle sizes of the fresh catalysts have not been determined by XRD measurement. This result suggests that the Pt particle sizes of the fresh catalysts are smaller than about 5nm, which are far smaller than that of the aged catalysts (see Table 4 in Chapter 3). CeO_2 on the fresh catalysts displays an OSC double than that on the aged catalysts, as shown in the estimations in Fig. 5. Therefore, it seems reasonable to conclude that the effect of addition of an Fe-compound was not observed because the fresh NSR catalyst shows a sufficient TWC performance derived from enough active sites and sufficient OSC to negate the role of the Fe-compound.

4. Conclusions

The effect of addition of an Fe-compound to a NO_x storage-reduction catalyst (NSR catalyst) on its three-way catalytic (TWC) performance was studied by comparison between Pt/Ba/(Al_2O_3-CeO_2-Fe_2O_3) and Pt/Ba/(Al_2O_3-CeO_2) catalysts to improve the durability against thermal deterioration.

The fresh Pt/Ba/(Al_2O_3-CeO_2-Fe_2O_3) catalyst showed the same TWC performance as did the fresh Pt/Ba/(Al_2O_3-CeO_2) catalyst. On the other hand, after thermal aging at 1123 K, the aged Pt/Ba/(Al_2O_3-CeO_2-Fe_2O_3) catalyst showed a higher TWC performance i.e., (1) the light-off performance under stoichiometric conditions, (2) the ability to compensate for the fluctuations between oxidizing and reducing conditions, and (3) activity for NO_x and CO under reducing conditions, compared with the aged Pt/Ba/(Al_2O_3-CeO_2) catalyst.

The data obtained from oxygen storage-release capacity (OSC) measurements, the reaction analysis of simple binary gas systems, and XRD measurements show that the Fe-compound on the aged Pt/Ba/(Al_2O_3-CeO_2-Fe_2O_3) catalyst plays two important

roles, i.e., (a) acting as a store for oxygen more effectively than does CeO_2, and (b) weakening the CO self-poisoning for the CO-O_2 and CO-NO reactions under reducing conditions, probably by provision of oxygen to the CO from Fe_2O_3 or/and Fe in a Pt-Fe alloy. The more effective storing of oxygen causes a greater ability to compensate for the fluctuations between oxidizing and reducing conditions. The weaker CO self-poisoning for the CO-O_2 reaction is due to the higher light-off performance under stoichiometric conditions. The weaker CO self-poisoning for the CO-NO reaction is due to the higher activity for NO_x and CO under reducing conditions

References

[1] W. Held, A. König, T. Richter, L. Puppe, SAE paper (1990) 900496.

[2] S. Sato, Y. Yu-u, H. Yahiro, N. Mizuno, M. Iwamoto, Appl. Catal. 70 (1991) L1.

[3] Y. Fujitani, H. Muraki, S. Kondoh, M. Fukui, Ger. Offen. (1988) DE3735151.

[4] H. Hamada, Y. Kintaichi, M. Sasaki, T. Ito, M. Tabata, Appl. Catal. 75 (1991) L14.

[5] A. Takami, T. Takemoto, S. Ichikawa, F. Saito, K. Komatsu, 1994 JSAE Spring Convention Proc. (1994) 9433858.

[6] M. Matsumoto, K. Yokota, H. Doi, K. Kimura, K. Sekizawa, S. Kasahara, Catal. Today 22 (1994) 127.

[7] N. Miyoshi, S. Matsumoto, K. Katoh, T. Tanaka, J. Harada, N. Takahashi, K. Yokota, M. Sugiura, K. Kasahara, SAE paper (1995) 950809.

[8] N. Takahashi, H. Shinjoh, T. Iijima, T. Suzuki, K. Yamazaki, K. Yokota, H. Suzuki, N. Miyoshi, S. Matsumoto, T. Tanizawa, T. Tanaka, S. Tateishi and K. Kasahara, Catal. Today 27 (1996) 63.

[9] K. Yamazaki, T. Suzuki, N. Takahashi, K. Yokota, and M. Sugiura, Appl. Catal. B 30 (2001) 459.

[10] H. Shinjoh, H. Muraki, Y. Fujitani, Catalysis and Automotive Pollution Control (1987) 187.

Chapter 5

Improved catalytic performance for PM oxidation in loose contact mode

Abstract

A CeO_2–Ag catalyst with a 'rice-ball' morphology, consisting of Ag particles in the center surrounded by fine CeO_2 particles, exhibits exceptional catalytic performance for soot oxidation by O_2 below 300 °C. The reaction mechanism over this catalyst were studied by O_2 temperature-programmed desorption (O_2-TPD), $^{18}O/^{16}O$ isotopic exchange (IE) reaction and electron spin resonance (ESR) techniques. It is speculated that adsorbed oxygen species on the Ag surface migrate to the CeO_2 surface via the Ag/CeO_2 interface to form O_n^{x-} species (at least partly O_2^-) and further migrate onto the soot particles. Due to morphological compatibility of the moderately large Ag particles (ca. 30–40 nm) and the extremely large interfacial area with the CeO_2 particles, the formation and migration rates of the oxygen species on the CeO_2–Ag catalyst are efficiently promoted, resulting in its distinguished catalytic performance and relative insensitivity to the contact mode of the soot-catalyst mixture.

Keywords; Soot oxidation, Silver, Ceria, Morphology, Reaction mechanism, Diesel emission control

1. Introduction

In recent years, diesel-powered vehicles have increased their market share in the world, due to lower fuel consumption, higher durability and reliability in comparison to gasoline-powered vehicles. Diesel engines are expected to play a positive role in the prevention of global warming by increased fuel efficiency and thus lower CO_2 emission than gasoline engines. However, there is a strong demand for the abatement of nitrogen oxide (NO_x; NO + NO_2) and particulate matter (PM; mainly ‘soot’) from diesel engines, which can give rise to serious environmental and health problems. The severity of new emission regulations requires solutions based on suitable after-treatment technologies, as well as technical improvements to the engines. The most effective and widely applied after-treatment technology for PM control is based on the diesel particulate filter (DPF). Soot trapped in a DPF must be periodically removed by combustion, due to unacceptable back pressure levels in the gas exhaust line. The direct oxidation of soot over the un-catalyzed DPF requires high temperatures around 600 °C, and is generally

carried out by injecting diesel fuel into the exhaust. This strategy incurs additional fuel consumption, requires a complex means of control, and can create significant thermal stress for the DPF and the other after-treatment devices (i.e., the de-NOx catalysts).

A catalyzed diesel particulate filter (C-DPF) is regarded as the most promising solution to reduce PM emissions from diesel engines, where the soot is trapped and oxidized with a catalyst at lower temperature. However, large soot particles are immobile and barely penetrate into the catalyst micropores or mesopores, and thus catalytic soot oxidation is quite slow [1,2]. The major problem with the C-DPF is the poor contact between the external catalyst surface and the soot particles. To overcome this problem, many catalysts and technologies based on different principles have been proposed. Using gas-phase NO_2 in the application of so-called continuously regeneration trap (CRT) technology causes a decrease in the soot oxidation temperature [3]. NO_2 is generated from the oxidation of NO over a platinum catalyst and functions as a mobile species for soot oxidation by creating catalyst-soot contact; however, a new trend in diesel engines to decrease NO_x emission could impose significant restrictions on the application of CRT technology. Organometallic fuel additives, also known as fuel-borne catalysts (FBCs), lead to the formation of catalyst-doped soot during combustion in the engine, which lowers the soot oxidation temperature in the DPF [4,5]; however, the continuous consumption of FBCs and the accumulation of metal oxide as an ash inside the DPF restrict their application strongly. A large number of molten salt catalysts, which can wet the soot surface as a mobile catalyst and therefore decrease the soot oxidation temperature, have been studied in recent years; the formulations are based on the addition of potassium or cesium to transition metal (such as Cu, V, Mo, Co or Fe) oxides [6-10], combinations of Co, K/MgO or Ba, K/CeO_2 [11-13], and perovskites such as $LaCrO_3$ and $La_{0.9}K_{0.1}Cr_{0.9}O_3$ [14]. However, these catalysts have drawbacks in some practical applications that are related to either thermal degradation or selective leaching in condensed water during the soot oxidation process [15].

Recently, many researchers have reported that CeO_2-based oxides have good activity for soot oxidation at lower temperature [16-23]. Aneggi et al. studied the effect of Ag addition on the soot oxidation activity of various metal oxides [24]; the addition of Ag to ZrO_2 and Al_2O_3 resulted in very active catalysts while addition to CeO_2 had little benefit. On the other hand, Machida et al. and Shimizu et al. reported that Ag loading onto CeO_2 enhanced the catalytic activity for soot oxidation [25,26]. However, the design concept of these catalysts, i.e., morphology control based on the functions of Ag and CeO_2, has not been devoted to the problem of catalyst-soot particle contact. In addition, silver-supporting catalysts may suffer from performance degradation due to Ag

sintering under oxidative conditions at temperatures around 400 °C [27].

Considering this background, we have developed an innovative CeO_2–Ag catalyst, which exhibits exceptional performance for soot oxidation with gaseous oxygen at temperatures below 300 °C [28]. This catalyst has a unique agglomeration morphology, as shown in Fig. 1, in which the scanning electron microscopy (SEM) image (a) shows that this catalyst consists of numerous spherical 'balls' with diameters of about 100 nm and the transmission electron microscopy (TEM) image of the cut plane of a single ball (b) shows that the center Ag metal is surrounded by fine CeO_2 particles. The morphology of this catalyst is schematically illustrated in Fig. 2, in which the unique agglomeration nanostructure is similar to a Japanese 'rice-ball', consisting of a center composed of Ag particles (rice ball filling) surrounded by fine CeO_2 particles (grains of rice). This morphology was designed to increase the Ag/CeO_2 interface area per unit surface area of Ag particles and to inhibit Ag sintering, because thermally stable CeO_2 particles act as barriers to sintering. A CeO_2–Ag catalyst with such morphology was synthesized by a novel nanofabrication method based on precipitation between aqueous solutions of nitrates and ammonia [28].

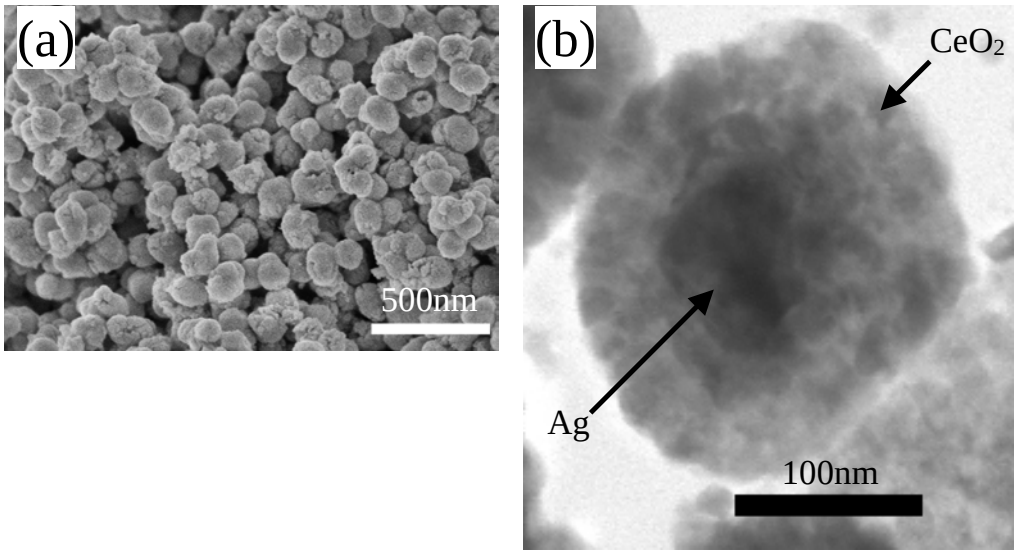

Fig. 1. (a) SEM image of CeO_2–Ag catalyst particles and (b) TEM image of the cut plane of a single spherical agglomerate of CeO_2–Ag catalyst [28].

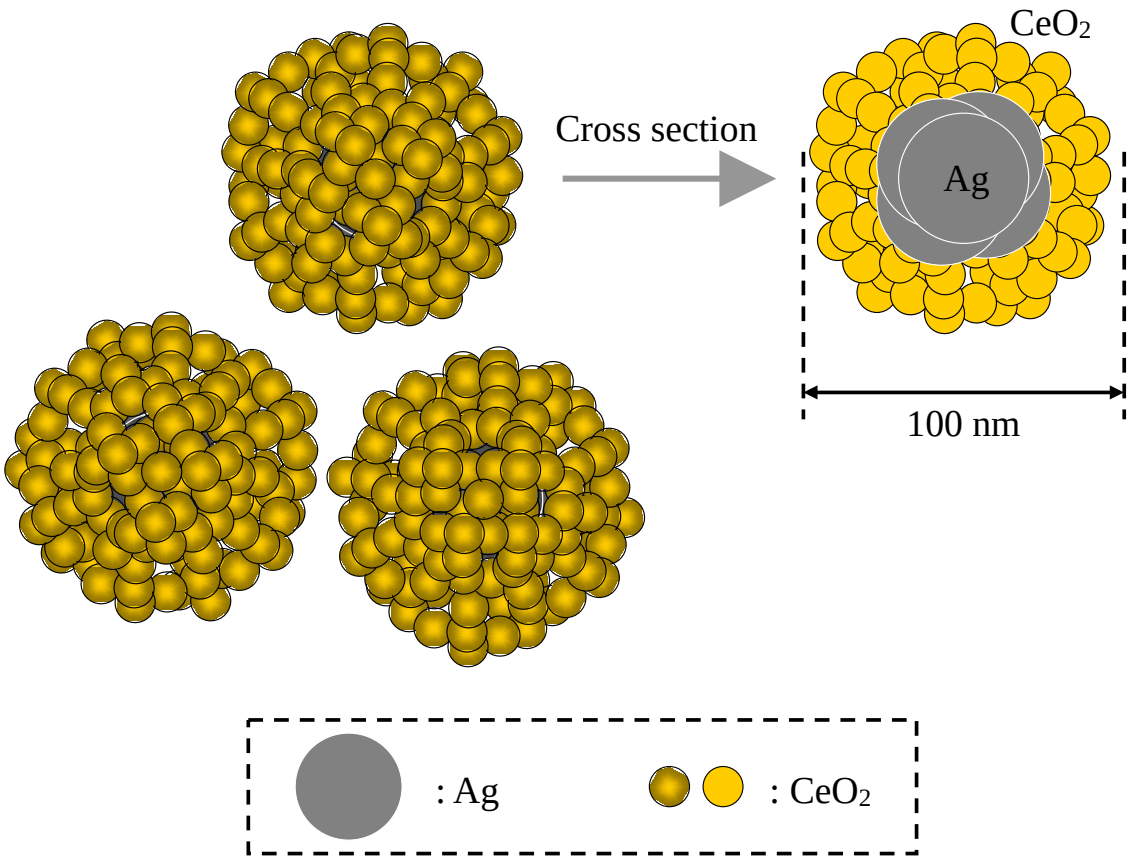

Fig. 2. Structural schematic of the CeO_2–Ag catalyst [28].

In this study, temperature-programmed oxidation (TPO) over the soot/catalyst mixture under tight and loose contact modes was used to evaluate the catalytic performance. To reveal the different aspects involved in catalytic soot oxidation, oxygen temperature-programmed desorption (O_2-TPD), $^{18}O/^{16}O$ isotopic exchange (IE) reaction, and electron spin resonance (ESR) techniques were employed to characterize the active property of oxygen species, oxygen mobility or migration rates and identification of oxygen species, respectively. Through discussing these characterization results and correlating with their catalytic performances, we tried to elucidate the mechanism involved in catalytic soot oxidation, especially over the CeO_2–Ag catalyst with unique "rice-ball" morphology, which exhibits an overwhelmingly high catalytic performance among the prepared catalysts.

2. Experimental

2.1. Catalyst preparation

A CeO_2–Ag catalyst was synthesized by a coprecipitation-based method. 150 mL aqueous solution of $AgNO_3$ (Toyo Chemical Industrial, 29.63 g) and $Ce(NO_3)_3 \cdot 6H_2O$ (Wako Pure Chemical Industries, 50.49 g) was added to a diluted ammonia solution (35.6 g of 25% ammonia solution, diluted by 100 mL of water) instantly (in less than a second) with a rotary stirrer (350 rpm) at room temperature. The mixture was stirred for 1 min and the coprecipitate was heated uniformly by steam in an autoclave at 120 °C for 10 min. The gained coprecipitate was separated by centrifugation and calcined at 500 °C for 5 h in air. The Ag content of the obtained CeO_2–Ag catalyst was 39 wt%. A more detailed description of the catalyst preparation is given elsewhere [28].

Ag(x)/CeO_2, Ag(x)+CeO_2, Ag(x)/Al_2O_3 and CeO_2 catalysts, where 'x' denotes the Ag content in wt%, were used as reference catalysts. The CeO_2 catalyst was obtained by calcination of a commercial CeO_2 powder (Rhodia, BET surface area 150 m^2/g) at 600 °C for 50 h, with a BET surface area of 78 m^2/g. The Ag(x)/CeO_2 catalysts were prepared by impregnation of the CeO_2 catalyst with aqueous $AgNO_3$ solution and calcination at 500 °C for 5 h in air. The Ag(x)+CeO_2 catalysts were prepared by physical mixing of the CeO_2 catalyst and a commercial Ag powder (Nisshin Engineering, BET surface area 9 m^2/g) with a magnetically driven mortar for 20 min followed by calcination at 300 °C for 5 h in air. The Ag(x)/Al_2O_3 catalysts were prepared by impregnation of a commercial Al_2O_3 powder (Showa Denko, UA-5205 with BET surface area 25 m^2/g) with aqueous $AgNO_3$ solution followed by calcination at 500 °C for 5 h in air.

2.2. Catalytic performance evaluation

The catalytic performance for soot oxidation was evaluated by temperature programmed oxidation (TPO) of soot-catalyst mixtures so as to compare the CeO_2–Ag catalyst with other reference catalysts. Two kinds of carbon black powder (Degussa AG, Printex-V with BET surface area 85 m^2/g, and Degussa AG, Printex-U with BET surface area 92 m^2/g) were used as the model soot in this study. The tight contact and loose contact modes were adopted for the soot-catalyst mixture [1,6]. The tight contact was attained by grinding catalyst with Printex-V using a magnetically driven mortar for 5 min. The loose contact was achieved by mixing catalyst with Printex-U loosely using a spatula for 10 min in a reproducible way. Because the grain size of the Printex-U is smaller than that of the Printex-V, for a better contact between the soot and catalyst, the

Printex-U was used for the samples in the loose contact mode. The weight ratios of the soot to catalyst were both 1:19.

In TPO experiments, the heat and mass transfer were concerned. Against heat and mass transfer limitations, two measures were taken as follows, for heat release from soot combustion, quartz wool (Tosoh, Fine grade) was used to dilute samples of catalyst-soot mixtures. For mass transfer limitation, the gas of O_2(10vol%)/He was flowed at a relative high flow rate (50 mL/min), although just 40 mg of the soot-catalyst mixture was put in a fixed-bed flow reactor. The two measures ensured that there was no apparent temperature rises caused by soot oxidation, and mass transfer limitation could be ignored. So we can say that the reaction regime was mostly controlled by the chemical kinetics, instead of by mass and heat transfer. A thermocouple was inserted into the soot-catalyst mixtures in order to monitor the reaction temperature. TPO spectra were recorded at a heating rate of 20 °C/min. The concentration of CO_2 and CO in the effluent were analyzed online using a quadrupole mass spectrometer (Q-MS; Ulvac, RG-102). Soot oxidation was regarded as the sum of the amount of CO_2 and CO formed during TPO; however, the amount of CO formed was much less than that of CO_2 in the presence of all of the catalysts examined. CO was only observed in the absence of the catalyst. The catalytic performance in this study is indicated by the temperature corresponding to the maximum soot oxidation rate (T_{max}) derived from the TPO spectra, with reference to the method by Moulijn et al. [1,6]. A lower T_{max} value indicates higher catalytic performance for soot oxidation.

2.3. Catalyst characterization

The BET surface area was measured by single-point N_2 adsorption at –196 °C using an automatic surface area analyzer (Microdata, MS4232II) after pretreatment at 200 °C for 20 min.

X-ray diffraction (XRD; Rigaku, RINT-TTR) patterns of the powder samples were recorded using Cu Kα radiation and a fixed power source (50 kV and 300 mA). The data were obtained between 20° and 60° (2θ) with a step of 0.02° and for 1 s per step. The average particle sizes of all the phases present in the catalysts were estimated using Scherrer's equation.

Oxygen temperature-programmed desorption (O_2-TPD) was performed in a fixed-bed reactor. For O_2 pre-adsorption, 160 mg of the catalyst was heated in a 20 mL/min O_2 flow at 600 °C for 30 min and cooled down to room temperature. After purging the catalyst with Ar for 30 min at room temperature, the catalyst was heated to

600 °C at 20 °C/min under a 20 mL/min Ar flow. The corresponding O_2 desorption spectrum was detected using the Q-MS.

Isotopic exchange (IE) reaction experiments were carried out in a re-circulated reactor (ca 100 cm^3) coupled to the Q-MS. Masses of 32, 34, 36 (oxygen isotopomers, $^{16}O_2$, $^{18}O^{16}O$ and $^{18}O_2$) and 28 (to detect a possible leak) were continuously monitored. The vacuum connection to the mass spectrometer was thermoregulated to maintain a constant pressure of 10^{-4} Pa, while the pressure in the reactor loop was 5650 Pa. 30 mg of the catalyst was placed into a quartz reactor for *in situ* experimentation. After oxidation with oxygen at 500 °C for 30 min and evacuation at 500 °C for 10 min, the sample was cooled to 300 °C. 5650 Pa of pure $^{18}O_2$ (99.2 % of ^{18}O, ICON) was then introduced at 300 °C and the partial pressure variation of the oxygen isotopomers, P_{36} ($^{18}O_2$), P_{34} ($^{18}O^{16}O$) and P_{32} ($^{16}O_2$), were continuously recorded. The total pressure (P_{36}, P_{34} and P_{32}) remained virtually constant. A more detailed description of this experiment is given elsewhere [29,30]. From the partial pressure values, the ^{18}O atomic fraction $\alpha_g(t)$ in the gas phase at a time t can be defined as:

$$\alpha_g(t) = [(1/2)P_{34}(t) + P_{36}(t)]/[P_{36}(t) + P_{34}(t) + P_{32}(t)] \quad (1)$$

The IE reaction at a time t, IE(t), corresponds to the disappearance of ^{18}O from the gas phase; therefore, it is possible to determine IE(t) (in moles of oxygen molecules per catalyst weight) using the following equation [29]:

$$IE(t) = n_g[1 - \alpha_g(t)]/w_c = (P_T/R)(V_r/T_r + V_c/T_c)[1 - \alpha_g(t)]/w_c \quad (2)$$

where n_g is the total number of moles of oxygen molecules in the gas phase, w_c is the catalyst weight, P_T is the total pressure, R is the ideal gas constant, V_r and V_c are the volumes of the heated and unheated zones of the reactor, respectively, and T_r and T_c are the temperatures of the heated and unheated zones of the reactor, respectively. The rate of IE reaction (in moles of oxygen molecules per catalyst weight and per time unit), R_{IE}, can be calculated using the following equation:

$$R_{IE} = -(n_g/w_c)d\alpha_g(t)/dt = -(P_T/Rw_c)(V_r/T_r + V_c/T_c)d\alpha_g(t)/dt \quad (3)$$

ESR analysis was conducted using a Bruker ESP350E spectrometer at 9.46 GHz. 20 mg of catalyst was placed in a 3.5 mm-diameter quartz ESR tube attached to a

high-vacuum stopcock, which allowed pretreatment and adsorption of various gases. After pre-adsorption of O_2 at 600 °C for 30 min, the catalyst was cooled to room temperature, purged with He for 30 min, and then finally exposed to a He flow or 3% H_2/He flow at 50 mL/min for 2 min at 250 °C, while the ESR spectrum was recorded at 20 K. Technically it is difficult to monitor or track the oxygen source involved in the soot oxidation. Considering the light-off temperature of soot oxidation (TPO) and oxygen desorption temperature from the O_2-TPD experiment, the above temperature of the ESR analysis was chosen as 250 °C. At this temperature, the existing oxygen species could be probed properly. Spin density was determined from double integration of derivative ESR signals and comparison with the weak pitch sample.

3. Results

3.1. Morphology and structural properties of catalysts

Fig. 3 shows XRD patterns of the CeO_2–Ag, Ag(39)/CeO_2, Ag(39)+CeO_2, Ag(39)/Al_2O_3 and CeO_2 catalysts, in addition to that of Ag powder used for the preparation of the Ag(x)+CeO_2 catalysts. The CeO_2-Ag catalyst consists of Ag (JCPDS 4-783) and CeO_2 (JCPDS 34-394) phases. The Ag(39)/CeO_2 and Ag(39)+CeO_2 catalysts also consist of Ag and CeO_2 phases. No evidence for the presence of the Ag_2O phase was obtained from the XRD patterns of all Ag-containing catalysts.

The particle sizes of the Ag and CeO_2 phases, and lattice spacings of Ag(111) and CeO_2(111) calculated from the XRD patterns of the catalysts are summarized in Table 1. The lattice spacing of Ag(111) and CeO_2(111) in the CeO_2–Ag catalyst are consistent with that of Ag(111) in the Ag powder and that of CeO_2(111) in the CeO_2 catalyst, respectively. Thus, no solid reaction occurred between the Ag and CeO_2 phases in this catalyst. In a similar fashion, no solid reaction occurred in the Ag(x)/CeO_2 and Ag(x)+CeO_2 catalysts, irrespective of the Ag content. The particle sizes of the Ag (36 nm) and CeO_2 (16 nm) phases from the XRD patterns of the CeO_2–Ag catalyst are consistent with the TEM image (Fig. 1b).

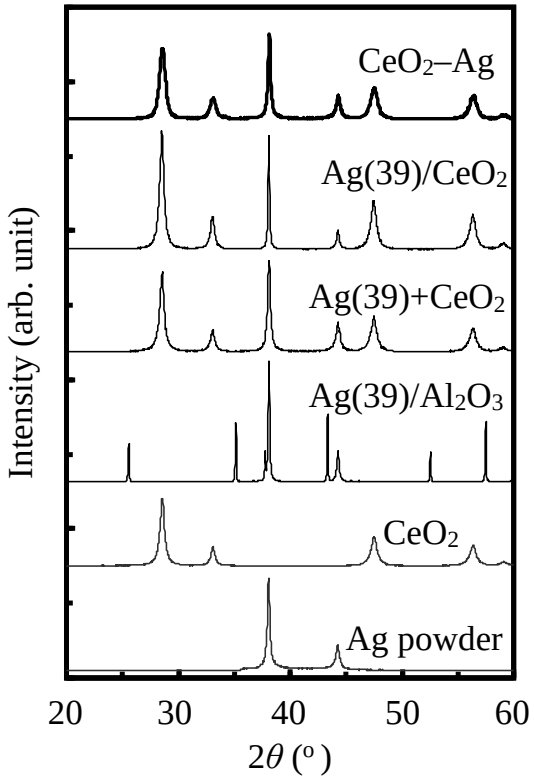

Fig. 3. XRD patterns of CeO_2–Ag, Ag(39)/CeO_2, Ag(39)+CeO_2, Ag(39)/Al_2O_3, CeO_2 catalysts and Ag powder.

3.2. TPO of catalyst-soot mixtures

Figs. 4a and 5a show the TPO profiles for soot oxidation over CeO_2–Ag, Ag(39)/CeO_2, Ag(39)+CeO_2, Ag(39)/Al_2O_3 and CeO_2 catalysts carried out under 10% O_2/He flow in addition to that for non-catalyzed soot oxidation (without catalyst) in tight and loose contact modes, respectively. The TPO profiles for all catalysts were shifted to lower temperatures compared with non-catalyzed soot oxidation regardless of the contact mode, which confirms that all the catalysts are able to catalyze soot oxidation. The performances of the CeO_2–Ag, Ag(39)/CeO_2 and Ag(39)+CeO_2 catalysts are higher than those of the Ag(39)/Al_2O_3 and CeO_2 catalysts in both contact modes. This result indicates that the catalytic performance for soot oxidation is promoted by the combination of Ag and CeO_2 particles. Moreover, the CeO_2–Ag catalyst exhibits much higher catalytic performance than the Ag(39)/CeO_2 and Ag(39)+CeO_2 catalysts, conventionally supported and mixed with the same composition respectively, in both contact modes.

Table 1

Morphology and structural properties of catalysts; BET surface area, particle size and lattice spacing

Catalyst	BET surface area (m^2/g)	Particle size (nm)		Lattice spacing (nm)		Peak intensity ratio (—) Ag(111)/CeO_2(111)
		Ag	CeO_2	Ag(111)	CeO_2(111)	
CeO_2-Ag	14.7	36	16	0.2358	0.3121	0.73
Ag(39)/CeO_2	30.1	89	21	0.2359	0.3124	0.37
Ag(10)/CeO_2	52.0	60	20	0.2359	0.3121	0.11
Ag(3.2)/CeO_2	59.2	28	20	0.2359	0.3122	0.03
Ag(1.9)/CeO_2	70.0	20	20	0.2356	0.3121	0.02
Ag(0.95)/CeO_2	78.1	n. d.[a]	20	—	0.3120	—
Ag(39)+CeO_2	49.9	47	20	0.2358	0.3120	0.85
Ag(10)+CeO_2	72.0	35	20	0.2358	0.3122	0.14
Ag(3.2)+CeO_2	77.2	31	20	0.2358	0.3122	0.05
Ag(1.9)+CeO_2	77.7	32	20	0.2359	0.3122	0.04
Ag(0.95)+CeO_2	78.0	34	20	0.2355	0.3120	0.02
Ag(39)/Al_2O_3	12.7	48	—	0.2359	—	—
CeO_2	77.8	—	20	—	0.3120	—
Ag powder	9.6	34	—	0.2359	—	—

[a] n.d. : not detected

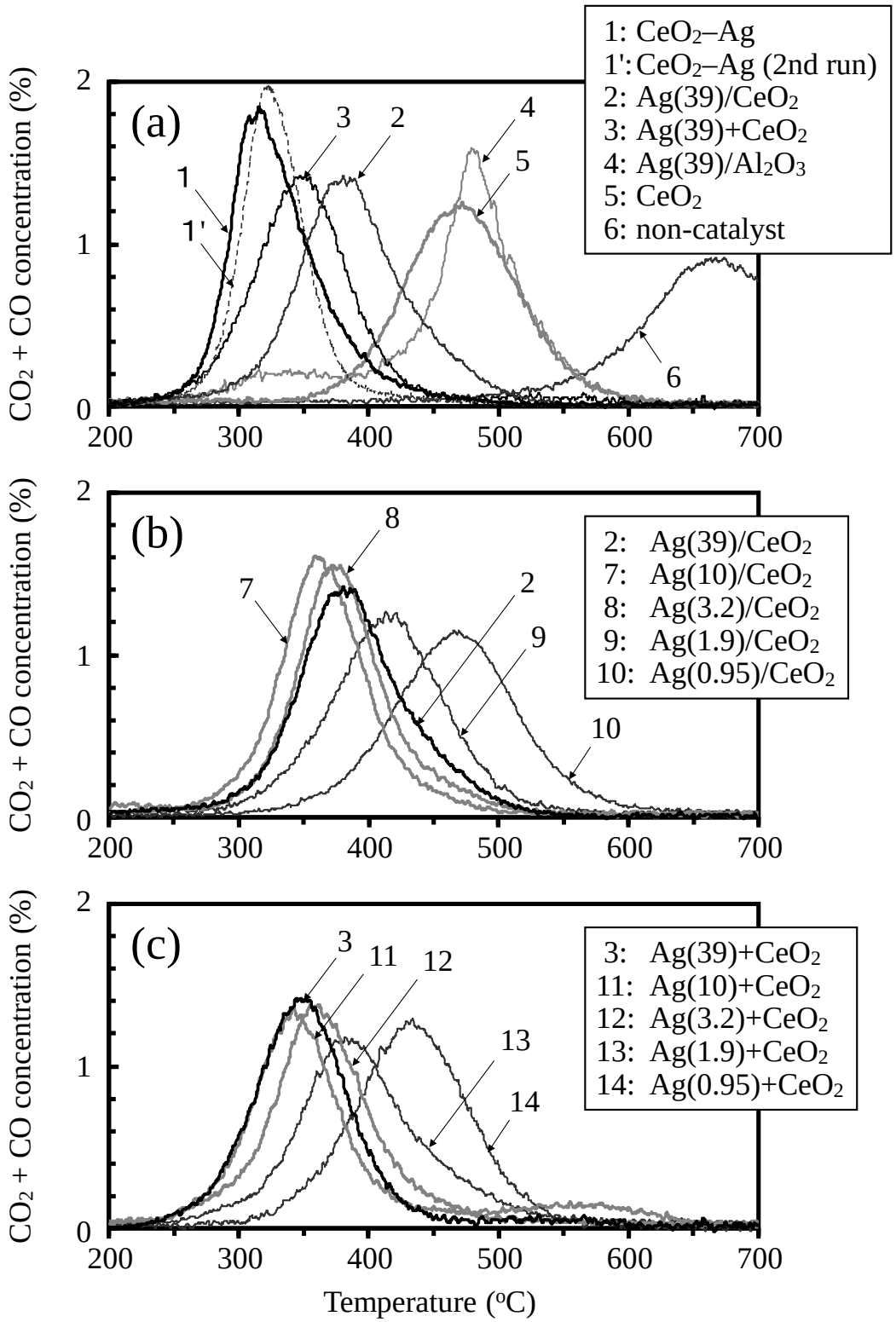

Fig. 4. (a) TPO profiles for soot oxidation in the presence and absence of CeO_2–Ag, Ag(39)/CeO_2, Ag(39)+CeO_2, Ag(39)/Al_2O_3, CeO_2 catalysts in tight contact mode. **(b)** and **(c)** TPO profiles for soot oxidation in the presence of Ag(x)/CeO_2 and Ag(x)+CeO_2 catalysts in tight contact mode.

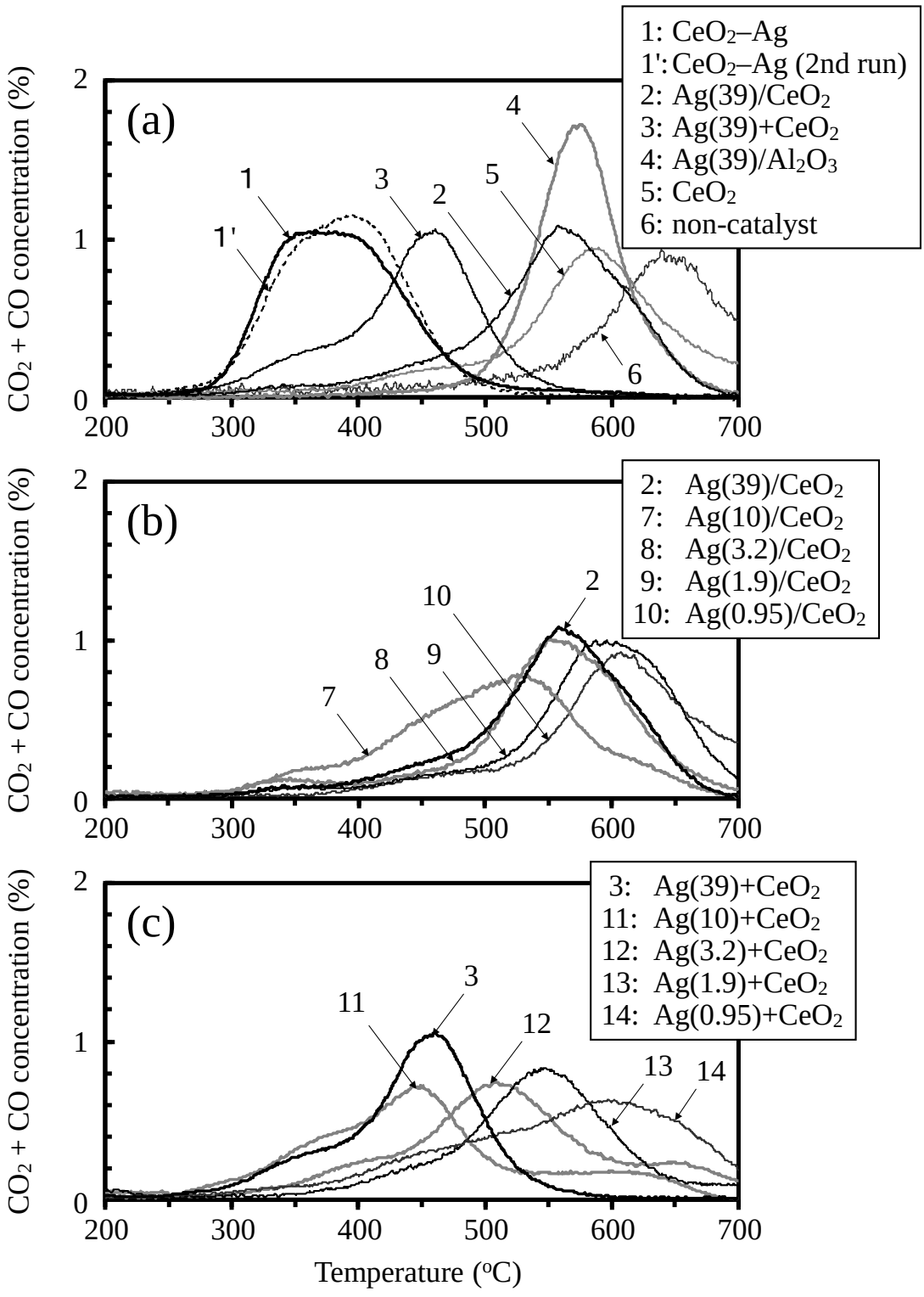

Fig. 5. (a) TPO profiles for soot oxidation in the presence and absence of CeO_2–Ag, Ag(39)/CeO_2, Ag(39)+CeO_2, Ag(39)/Al_2O_3, CeO_2 catalysts in loose contact mode. **(b)** and **(c)** TPO profiles for soot oxidation in the presence of Ag(x)/CeO_2 and Ag(x)+CeO_2 catalysts in loose contact mode.

Figs. 4b and 5b show TPO profiles for soot oxidation over Ag(x)/CeO_2 catalysts with different Ag contents in tight and loose contact modes, respectively. Figs. 4c and 5c show TPO profiles for soot oxidation over Ag(x)+CeO_2 catalysts with different Ag contents in tight and loose contact modes, respectively. The derived T_{max} values of the all catalysts in both contact modes are summarized in Table 2. For all the catalysts, the order of soot oxidation performance in tight contact mode is almost the same to that in loose contact mode. The Ag(10)/CeO_2 catalyst has the highest performance among the Ag(x)/CeO_2 catalysts, and the Ag(10)+CeO_2 catalysts has the highest performance among the Ag(x)+CeO_2 catalysts, in both contact modes. However, the Ag(10)/CeO_2 and Ag(10)+CeO_2 catalysts are both inferior in performance to the CeO_2–Ag catalyst. On the other hand, the advantage with the Ag(10)+CeO_2 catalysts is its very simple preparation procedure.

The Ag(1.9)/CeO_2 catalyst has lower performance than the Ag(1.9)+CeO_2 catalyst with the same composition in both contact modes (Table 2), while the former catalyst has smaller Ag particles (Table 1) and therefore a larger Ag surface area than the latter catalyst. The Ag(0.95)/CeO_2 and Ag(0.95)+CeO_2 catalysts exhibit the same trend in catalytic performance and Ag particle size, which suggests that smaller Ag particles do not necessarily cause higher catalytic performance for soot oxidation.

All the catalysts show lower performance for soot oxidation in loose contact mode than that in tight contact mode. The contact closeness between catalyst and soot is very important for the soot oxidation activity over a catalyst [6]. Even in the loose contact mode, the CeO_2–Ag catalyst still exhibits the highest performance among the catalysts, soot oxidation starting around 280°C and revealing its T_{max} at 376°C. Moreover, the CeO_2-Ag shows the smallest T_{max} difference between loose and tight contact modes (ΔT_{max} values in Table 2) among the all catalysts, that is, the CeO_2–Ag catalyst is the most insensitive to the physical contact mode between soot and catalyst.

Table 2

Catalytic performance for soot oxidation, and parameters from O_2-TPD, $^{18}O/^{16}O$ IE reaction and ESR experiments.

Catalyst	T_{max} (°C)		ΔT_{max} [b] (°C)	O_2 desorption (μmol/g)	IE reaction rate (μmol/g·min)	Spin density (μmol/g)
	tight contact	loose contact				
CeO_2-Ag	315	376	61	33.5	22.6	0.830
Ag(39)/CeO_2	381	563	182	9.1	9.1	0.232
Ag(10)/CeO_2	362	526	164	17.0	12.9	0.465
Ag(3.2)/CeO_2	371	550	179	9.3	7.4	—
Ag(1.9)/CeO_2	414	596	182	2.1	3.9	—
Ag(0.95)/CeO_2	466	610	144	0.5	—	—
Ag(39)+CeO_2	351	461	110	23.5	—	—
Ag(10)+CeO_2	342	443	101	25.0	—	—
Ag(3.2)+CeO_2	355	522	167	18.0	—	—
Ag(1.9)+CeO_2	384	548	164	5.0	6.4	—
Ag(0.95)+CeO_2	433	597	164	1.9	—	—
Ag(39)/Al_2O_3	480	575	95	2.0	2.7	0.091
CeO_2	462	590	128	0.0	0.6	0.002
none (soot only)	660 [c]	640 [d]	—		—	—

[b] ΔT_{max} = (T_{max} in loose contact mode) − (T_{max} in tight contact mode)

[c] T_{max} of Printex-V

[d] T_{max} of Printex-U

The TPO experiment was repeated with the used CeO_2–Ag catalyst. As illustrated in Figs. 4a and 5a corresponding to tight and loose contact modes, the TPO profile with the repeated experiment (curve 1') exhibits almost the same catalytic performance to that with the first TPO run in both contact modes. This result indicates that the soot oxidation activity of the CeO_2–Ag catalyst is almost reproducible, and the CeO_2–Ag catalyst has the potential for future actual application. It was also noted that the second spectrum slightly shifted to higher temperatures in all cases. This indicated that the CeO_2–Ag catalyst somewhat deteriorated after experienced the first test. It is assumed that the rice ball morphology of the CeO_2–Ag subtly collapses during the soot oxidation, or some unburned fine soot particles and ash generated in the first run caused bad contact between the used catalyst and fresh soot. Further investigations are necessary to clarify the involved reasons for this deactivation, as well as more efforts to improve its thermostability.

3.3. O_2-TPD

Figs. 6a-6c show O_2-TPD profiles of the CeO_2–Ag and reference catalysts. The CeO_2–Ag catalyst exhibits O_2 desorption between 200 and 450 °C, corresponding to the light-off of soot oxidation below 300 °C over the CeO_2-Ag catalyst (Figs. 4a and 5a). O_2 desorption is also observed from the Ag(x)/CeO_2, Ag(x)+CeO_2 and Ag(39)/Al_2O_3 catalysts in the same temperature range, but not for the CeO_2 catalyst.

The amounts of O_2 desorption from the catalysts between 200 and 450 °C are summarized in Table 2. The CeO_2–Ag catalyst exhibits the largest O_2 desorption among all the catalysts. Fig. 7 reveals an excellent correlation between the T_{max} values for TPO in tight and loose contact modes, respectively, as a function of the amounts of O_2 desorption from O_2-TPD over all the catalysts. These results strongly suggest that active oxygen species for soot oxidation correspond to the adsorbed oxygen species on the catalyst from gaseous O_2, which is desorbed in the temperature range between 200 and 450 °C.

The O_2-TPD experiment was also repeated with the used CeO_2–Ag catalyst. As indicated in Figs. 6a, almost the same O_2-TPD spectra of the CeO_2–Ag catalyst were gained in first and second runs. This result demonstrates that the gaseous oxygen could be adsorbed onto the CeO_2–Ag catalyst, and activated to active oxygen species in a reproducible way.

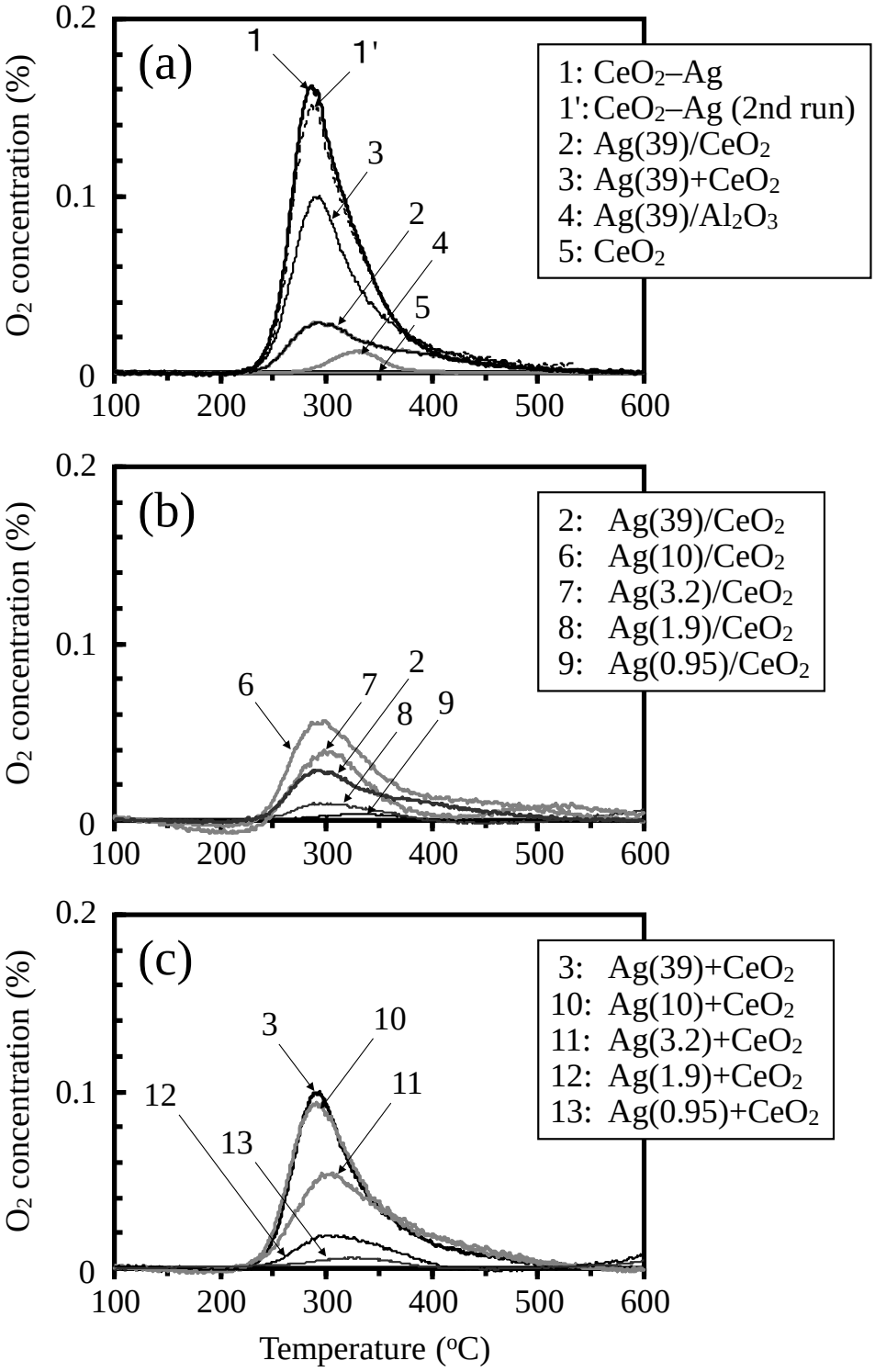

Fig. 6. (a) O_2-TPD profiles of CeO_2–Ag, Ag(39)/CeO_2, Ag(39)+CeO_2, Ag(39)/Al_2O_3, CeO_2 catalysts. **(b)** and **(c)** O_2-TPD profiles of Ag(x)/CeO_2 and Ag(x)+CeO_2 catalysts.

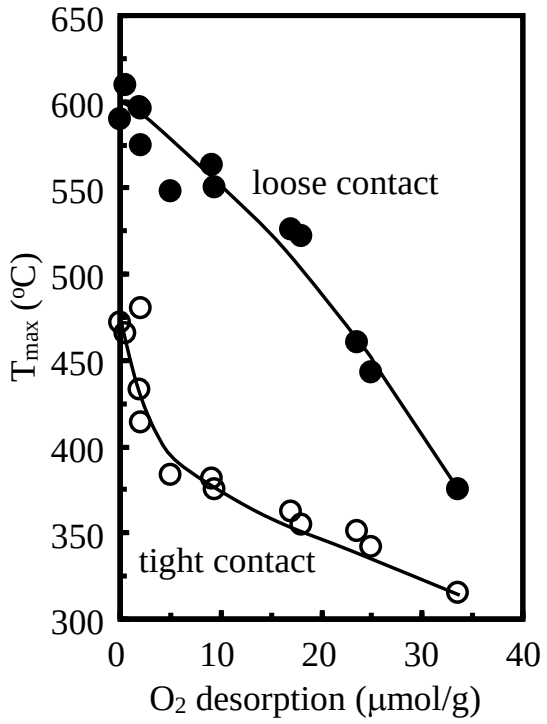

Fig. 7. T_{max} value from TPO experiments in tight and loose contact modes as a function of the amount of O_2 desorption determined from O_2-TPD experiments.

3.4. $^{18}O/^{16}O$ IE reaction

The IE reaction as an informative technique was employed to characterize oxygen mobility over the catalysts [29,30] in this study. As shown in Fig. 8a, the partial pressures of three oxygen molecules, P_{36} ($^{18}O_2$), P_{34} ($^{18}O^{16}O$) and P_{32} ($^{16}O_2$), evolve during the $^{18}O/^{16}O$ IE reaction over the CeO_2–Ag catalyst at 300 °C. The $^{18}O_2$ molecules in the gas phase adsorb and decompose on the catalyst surface, then exchange and desorb to $^{18}O^{16}O$ and $^{16}O_2$ molecules into the gas phase. Figs. 8b and 8c show IE reaction profiles against reaction time over the CeO_2–Ag and reference catalysts derived by Eq. (2). At 300°C, the IE reaction proceeds the fastest over the CeO_2–Ag catalyst, apparently occurs over the Ag(x)/CeO_2, Ag(x)+CeO_2 and Ag(39)/Al_2O_3 catalysts, but is detectable over the CeO_2 catalyst, indicating that the co-existence or inter-particle contact of Ag particle and CeO_2 is truly necessary for the IE reaction or oxygen migration.

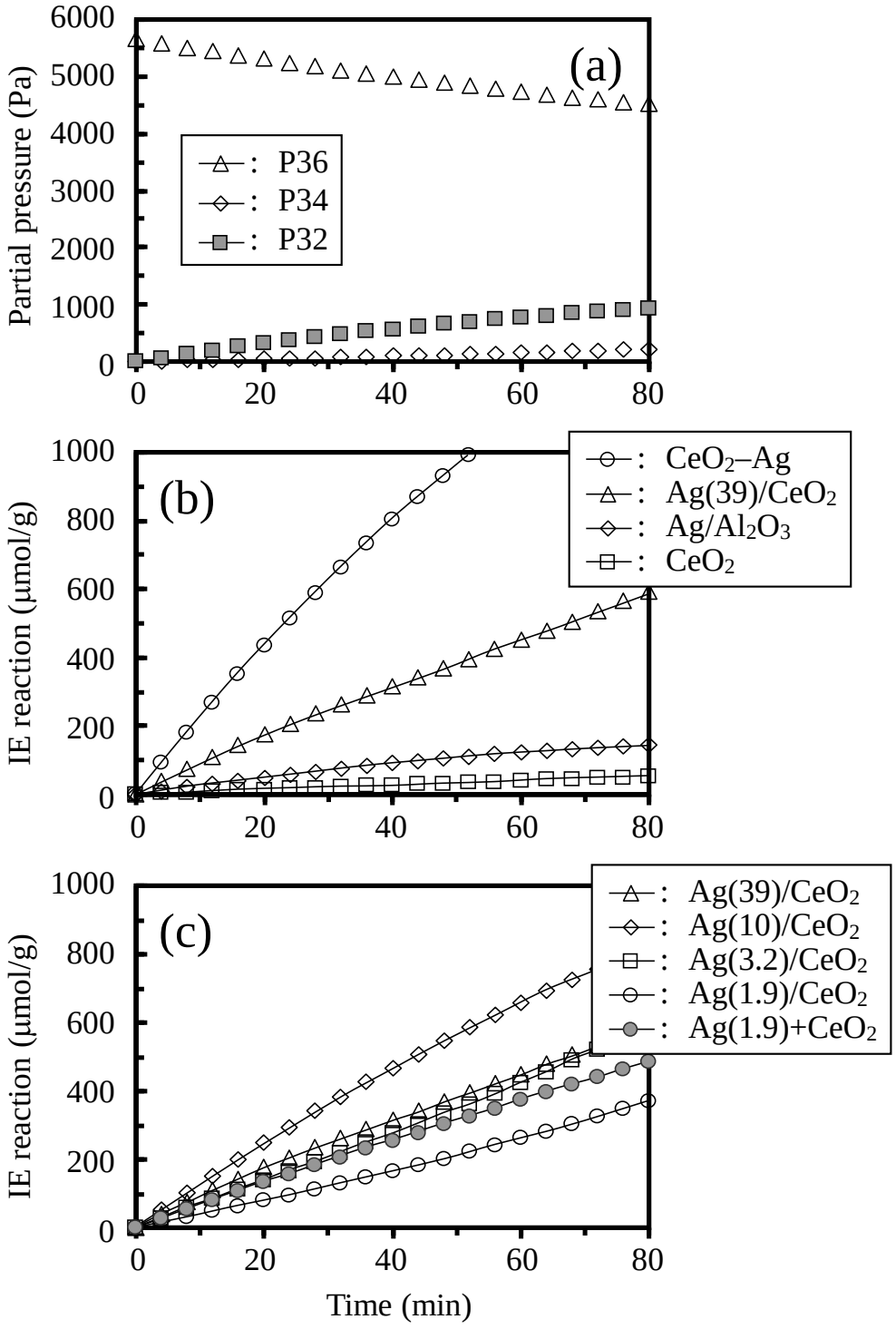

Fig. 8. (a) Partial pressure evolution of $^{18}O_2$, $^{18}O^{16}O$ and $^{16}O_2$ molecules for the IE reaction over the CeO_2–Ag catalyst at 300 ° C . **(b)** IE reaction profiles of CeO_2–Ag, Ag(39)/CeO_2, Ag(39)/Al_2O_3, CeO_2 catalysts. **(c)** IE reaction profiles of Ag(x)/CeO_2 and Ag(x)+CeO_2 catalysts.

The initial IE reaction rates by Eq. (3) are summarized in Table 2. The CeO_2–Ag catalyst shows higher IE reaction rate than the Ag(x)/CeO_2, Ag(x)+CeO_2, Ag(39)/Al_2O_3 and CeO_2 catalysts. The IE reaction rates or migration rate closely associates with oxygen species adsorbing and migrating on Ag surface, the interface between Ag and CeO_2, and the surface and bulk of CeO_2. These results above reveal that the active oxygen species are potentially mobile from the gaseous O_2 onto the Ag surface through adsorption, and actively exchangeable with the oxygen in CeO_2, bridged by the interface between the Ag and the CeO_2 particles of the catalysts. As the result, the CeO_2–Ag catalyst with the unique "rice-ball" morphology exhibits the fastest oxygen migration via the interface between the Ag and the CeO_2 particles among all the catalyst samples.

Fig. 9 shows a good correlation between the IE reaction rates for the $^{18}O/^{16}O$ IE reaction and the amounts of O_2 desorption from O_2-TPD measurements.

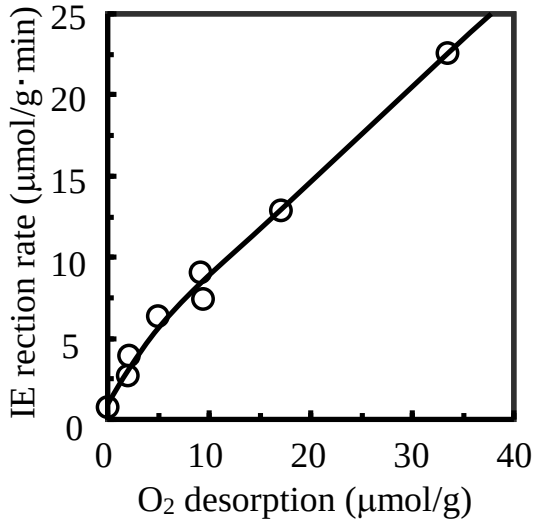

Fig. 9. IE reaction rates for the $^{18}O/^{16}O$ IE reaction versus the amount of O_2 desorption determined from O_2-TPD experiments.

3.5. ESR

When CeO_2–Ag catalyst is exposed to He flow at 200 °C after a pretreatment (exposure to O_2 flow at 600 °C for 30 min, cooling to room temperature under the same gas flow and exposure to He flow for 30 min at room temperature), no ESR signals of oxygen species were observed. However, when exposed to 3% H_2/N_2 flow at 200 °C for 2 min after the same pretreatment, ESR signals with $g_{//} = 2.046$, $g_{//} = 2.037$ and $g_{\perp}$ =

2.010 were observed, as shown in Fig. 10. These signals are all attributed to superoxide (O_2^-) species bonded to Ce cations [31,32]. ESR analyses of other catalysts using the same procedure also provide signals with the same g values. Among all of the catalysts shown in Fig. 9, the CeO_2–Ag catalyst shows the highest ESR signal intensity.

The spin densities of O_2^- species over the catalysts are listed in Table 2. Fig. 11 shows a linear correlation between the spin densities of O_2^- species from ESR and the amount of O_2 desorption from O_2-TPD with a slope of 0.024, which indicates that some part of the adsorbed oxygen species on the catalyst under oxidative conditions are transformed into the O_2^- species on the CeO_2 surface under weak reductive conditions.

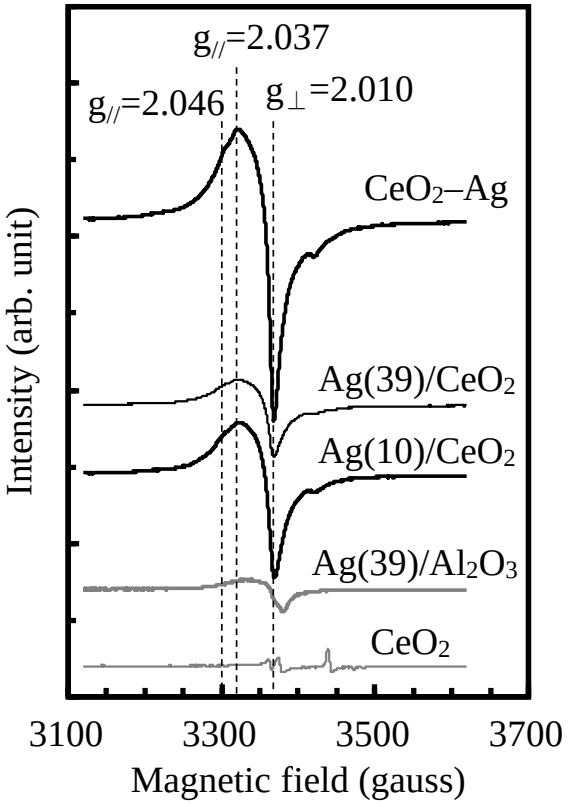

Fig. 10. ESR spectra of CeO_2–Ag, Ag(39)/CeO_2, Ag(10)/CeO_2, Ag(39)/Al_2O_3, CeO_2 catalysts.

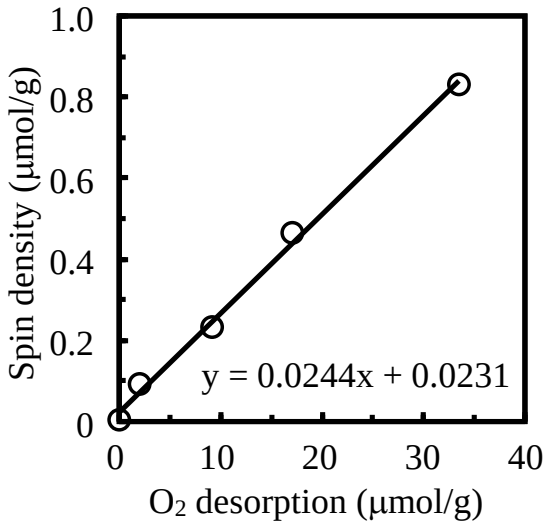

Fig. 11. Spin densities of O_2^- species versus the amount of O_2 desorption from O_2-TPD experiments.

4. Discussion

4.1. Effect of rice-ball morphology on the formation of active oxygen species for soot oxidation

The CeO_2–Ag catalyst with a rice-ball morphology exhibits higher performance for soot oxidation than any of the conventional supported Ag(x)/CeO_2, Ag(x)+CeO_2 mixed, Ag(x)/Al_2O_3 and CeO_2 catalysts, irrespective of the Ag content and the tight or loose mode of the soot-catalyst contact. An excellent correlation between soot oxidation performance and the amount of O_2 desorption from O_2-TPD (Fig. 7) strongly suggests that active oxygen species for soot oxidation correspond to the oxygen species adsorbed on the catalyst from gaseous O_2 and desorbed from 200 to 450 °C. That is, the amount of O_2 desorption from O_2-TPD is parallel to the amount of the active oxygen species formed on the catalyst. Therefore, the increased performance of the CeO_2–Ag catalyst is closely relevant to the promoted formation of the active oxygen species compared to the other catalysts. In this section, we explore the reasons for the ease and extent of active oxygen species formation over the CeO_2–Ag catalyst.

It was reported that atomic oxygen species on Ag surfaces desorb as molecular O_2 around 300 °C [33-36]. There is no O_2 desorption in the O_2-TPD spectrum of CeO_2 catalyst, Therefore, the atomic oxygen species are very likely formed on the Ag surface by adsorption from gaseous O_2, and activated to participate into soot oxidation as active oxygen species. On the other hand, the Ag(39)/CeO_2 catalyst has a much larger amount

of O_2 desorption from O_2-TPD than the Ag(39)/Al_2O_3 catalyst, while the former has larger Ag particles and consequently a smaller Ag surface than the latter (Tables 1 and 2). This suggests that a synergistic effect from the Ag–CeO_2 combination contributes to the formation of active oxygen species on the Ag surface. This synergistic effect is caused by the interface between Ag and CeO_2 particles, not merely the physical factor of Ag dispersion on the supporting material [31].Thus, the interface between Ag and CeO_2 particles plays a crucial role in catalytic soot oxidation. A good correlation is obtained between the amount of active oxygen species formed on the Ag surface and the rate of oxygen migration via the interface between Ag and CeO_2 particles (Fig. 9). Lippits et al. reported that the interaction between Ag and CeO_2 has a significant influence on the activity for the selective oxidation of ammonia to nitrogen, possibly due to an improved supply of active oxygen from the CeO_2 to Ag particles [37]. Therefore, it is reasonable to conclude that the larger interface between Ag and CeO_2 particles leads to increased formation of active oxygen species on the Ag surface possibly due to a faster supply of oxygen from the CeO_2 to Ag particles and the stabilization of oxygen on the Ag surface [26].

Next we consider the effect of Ag particle size on the formation of active oxygen species for soot oxidation. With respect to the interface between Ag and CeO_2 particles, small Ag particles loaded on the CeO_2 surface are expected to create a large interface area; however, the Ag(1.9)/CeO_2 catalyst with smaller Ag particles has lower O_2 desorption from O_2-TPD compared to the Ag(1.9)+CeO_2 catalyst with larger Ag particles (Table 1, 2). The Ag(0.95)/CeO_2 catalyst, with a Ag particle size too small to be determined by XRD, and the Ag(0.95)+CeO_2 catalyst exhibit the same trend between the formation of active oxygen species and the Ag particle size, which indicates that small Ag particles of 20 nm or less are unfavorable for the formation of the active oxygen species on their surfaces.

Many authors have reported catalytic size effects over supported Ag catalysts for some reactions, such as ethylene epoxidation, propylene epoxidation, and methane oxidation [38-43]. Bal'zhinimaev, using Ag/Al_2O_3 and Ag/SiO_2 catalysts with the average Ag particle sizes between 15 and 2000 nm, showed that the specific rate of ethylene epoxidation drastically increased by more than one order of magnitude with an increase in the size of the Ag particles from 20 to 50 nm and a further slight increase with further increase in the size of the Ag particles [38]. Bal'zhinimaev demonstrated that nucleophilic oxygen species, formed via dissociative chemisorption of O_2 molecules, and electrophilic oxygen species, formed from nucleophilic oxygen species, play cooperative roles in the reaction. Nucleophilic oxygen species are formed on a

regular surface region, which is obtained by large Ag particles. Both nucleophilic and electrophilic oxygen species are atomic oxygen species adsorbed on the Ag surface. Therefore, it is very likely that the formation of active oxygen species for soot oxidation is also favored by large Ag particles greater than a certain size. On the other hand, Ag particles that are too large are expected to impede the formation of active oxygen species, due to their small surface area and small interface area formed with CeO_2 particles. The Ag(10)/CeO_2 catalyst with larger Ag particles (60 nm) has less O_2 desorption than the Ag(10)+CeO_2 catalyst with smaller Ag particles (35 nm) (Tables 1 and 2). Therefore, it may be that active oxygen species for soot oxidation is formed most effectively on Ag particles with sizes in the range between 30 and 40 nm.

A large interface between moderately large Ag particles (probably >30 nm) and CeO_2 particles can be achieved by the deposition of fine CeO_2 particles that are much smaller than Ag particles on the Ag surface, that is, a rice-ball morphology. The amount of active oxygen species formed on the Ag surface in the CeO_2–Ag catalyst is 67 μmol-oxygen atoms/g derived from the O_2 desorption (Table 2). The number of exposed Ag atoms in the CeO_2–Ag catalyst, as derived from the Ag particle size (36 nm) from XRD measurements is 52 μmol-Ag atoms/g (Table 1). This number might be underestimated, because XRD measurement detects larger Ag particles preferentially in the case of a size distribution of Ag particles. Thus, we may say that the number of exposed Ag atoms is comparable to the amount of the active oxygen species formed on the Ag surface. Therefore, these results suggest that the active oxygen species for soot oxidation is effectively formed on most of the exposed Ag atoms and an extremely large interface of the Ag surface with CeO_2 particles results from the rice-ball morphology of the CeO_2–Ag catalyst.

It is concluded that the rice-ball morphology of the CeO_2–Ag catalyst is optimal for the formation of active oxygen species for soot oxidation, because it satisfies the requirement for both moderately large Ag particles (ca. 30 to 40 nm) and an extremely large interface area with CeO_2 particles.

4.2. Effect of rice-ball morphology on the migration of active oxygen species for soot oxidation

The soot used in this study cannot physically contact the Ag particles in the center of the CeO_2–Ag catalyst particles, because the particle size (ca. 100 nm) is too large, and soot oxidation proceeds efficiently on the CeO_2 surface surrounding the spherical agglomerate. Therefore, it is supposed that the active oxygen species generated on the Ag surface from gaseous O_2 migrates to soot particles on the CeO_2 surface during soot

oxidation. In this section, we investigate the migration of the active oxygen species for soot oxidation over the CeO_2-Ag catalyst.

ESR analyses show that some atomic oxygen species adsorbed on the Ag surface from gaseous O_2 under oxidative conditions are transformed into O_2^- species on the CeO_2 surface under weak reductive conditions (Fig. 11). It is known that the catalyst is exposed to local reductive conditions during soot oxidation [20]. Thus, it is likely that the active oxygen species formed on the Ag surface of the CeO_2–Ag catalyst migrate via the interface between Ag and CeO_2 particles to the CeO_2 surface, of which a certain fraction are transformed into the O_2^- species during soot oxidation. Surface mobility phenomena of active oxygen species on CeO_2-containing oxides have been invoked by many authors and considered as an elementary step of the reaction mechanisms [17,29,30,44-46]. Martin et al. reported that the reoxidation of pre-reduced CeO_2 proceeds with very mobile oxygen species and leads to an excess of oxygen uptake due, in particular, to the presence of different oxygen species, which could be superoxide (O_2^-) and peroxide (O_2^{2-}) species [46]. Krishna et al. reported that CeO_2 and rare-earth-modified CeO_2 catalysts function to increase active oxygen transfer to the soot surface, followed by chemisorption of the active oxygen to form surface oxygen complexes during soot oxidation [17]. Therefore, it is very likely that active O_n^{x-} species (n =1 or 2, x = 1 or 2) on the CeO_2 surface of the CeO_2–Ag catalyst also migrate onto the soot particles for soot oxidation. Most of the O_n^{x-} species would be O_2^-, although there remains the possibility for the presence of other oxygen species.

In general, the interface area between Ag and CeO_2 is smaller than the Ag and CeO_2 surface areas in catalysts composed of Ag and CeO_2 particles, which result in a bottleneck for the migration of oxygen species. In this case, transformation of the active oxygen species is required at the interface. Therefore, migration via the interface should be a rate determining step for the complete migration of the active oxygen species during soot oxidation. $^{18}O/^{16}O$ IE reactions reveal that the CeO_2–Ag catalyst exhibits the fastest oxygen migration via the interface (Figs. 8b and 8c). The interface area between the Ag and CeO_2 particles in the present CeO_2–Ag catalyst is extremely large; therefore, it can be concluded that the rice-ball morphology is also suitable for the fast migration of active oxygen species for soot oxidation. Two functions of the interface, faster migration and increased formation of the active oxygen species, were confirmed by the good correlation in Fig. 9.

4.3. Mechanism of soot oxidation over CeO_2–Ag catalyst

We propose a possible mechanism for soot oxidation over the CeO_2–Ag catalyst, depicted in Fig. 12, that illustrates the morphology of the catalyst. Firstly, gaseous O_2 is adsorbed on the surface of Ag particles through a synergistic effect with CeO_2 particles to form atomic oxygen species, which are the first active oxygen species for soot oxidation. The extremely large interface between Ag and CeO_2 particles and the moderately large size of the Ag particles contribute to the formation of the species. The atomic oxygen species on the Ag surface then migrate to the surface of CeO_2 particles via the interface, transforming into O_n^{x-} species (at least partly O_2^-), which is the second active oxygen species. The extremely large interface contributes to the fast migration of the species. The first and second active oxygen species exist in equilibrium during soot oxidation. Finally, the O_n^{x-} species on the CeO_2 surface, which is a mobile active oxygen species, migrates onto the soot particle surfaces through the contact surface between CeO_2 and soot particles, oxidizes the soot completely to CO_2, and finally releases into the gas phase. The mobile active oxygen species abundantly formed in the interior portion of catalyst, migrate fast out to the external surface, and efficiently access to soot particles. This results in its outstanding catalytic performance for soot oxidation, but insensitivity to the contact between catalyst and soot.

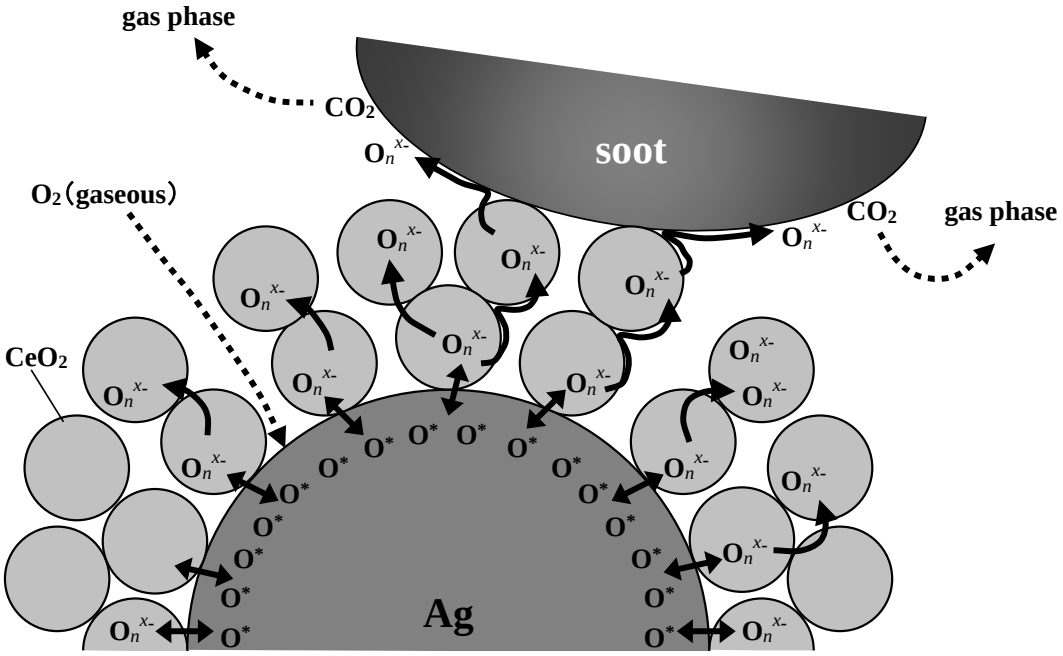

Fig. 12. Schematic mechanism for soot oxidation over the CeO_2–Ag catalyst.

Good correlations between the catalytic performance for soot oxidation and all parameters concerning the active oxygen species of catalysts in this study (Figs. 7, 9, and 11) demonstrate that the mechanism for soot oxidation over Ag(x)/CeO_2, conventional supported catalysts, and Ag(x)+CeO_2, particle mixed catalysts should be the same as that over the CeO_2–Ag catalyst, assuming that the Ag and CeO_2 particles, and their interface have the same functions. Some researchers have suggested mechanisms for soot oxidation over Ag(x)/CeO_2 catalysts; however, they require further information, such as the mobility of the active oxygen species, the respective role of Ag and CeO_2 particles, and the factors influencing the activity for soot oxidation. By employing the rice-ball morphology in a CeO_2–Ag catalyst, the configuration of Ag, CeO_2 and soot particles can be set, which assists in understanding the mechanism of soot oxidation over the Ag(x)/CeO_2 and CeO_2–Ag catalysts.

On the other hand, the CeO_2 catalyst does not desorb O_2, as determined from O_2-TPD experiments; however, it does have some catalytic performance for soot oxidation (Figs. 4a and 5a). Several researchers have studied CeO_2 and rare-earth-modified CeO_2 catalysts for soot oxidation and have proposed mechanisms for soot oxidation over these catalysts that are based on their oxygen storage and release capacities [16-21], and should therefore be different from that over the CeO_2–Ag catalyst, although such mechanisms may be involved in the case of the CeO_2–Ag catalyst.

5. Conclusion

An innovative CeO_2–Ag catalyst with a unique agglomeration morphology similar to a rice-ball, which consists of a central Ag particle agglomerate surrounded by fine CeO_2 particles, exhibits outstanding performance for soot oxidation with gaseous O_2 below 300 °C in tight and loose contact modes. The catalytic performance is higher than those of conventional Ag/CeO_2 supported catalysts and of Ag+CeO_2 mixed particle catalysts irrespective of the Ag content, in addition to those of Ag/Al_2O_3, and CeO_2 catalysts, in both contact modes. Moreover, the CeO_2–Ag catalyst is less sensitive to contact between catalyst and soot than the other reference catalysts.

The reaction mechanism and high performance for soot oxidation over the CeO_2–Ag catalyst was investigated. O_2-TPD experiments show that atomic oxygen species adsorbed weakly on the Ag surface through a synergistic effect with CeO_2 particles from gaseous O_2, which are desorbed in the temperature range between 200 and 450 °C, function as active oxygen species for soot oxidation. $^{18}O/^{16}O$ IE reaction experiments revealed that atomic oxygen species on the Ag surface can migrate to the

CeO_2 particles via the Ag/CeO_2 interface. ESR analysis indicated that some of the atomic oxygen species on the Ag surface migrate to the CeO_2 surface and transform into O_n^{x-} species (n =1 or 2, x = 1 or 2, at least partly O_2^- species) during soot oxidation. These results suggest that the O_2^- species on the CeO_2 surface also function as the active oxygen species for soot oxidation. A possible mechanism for soot oxidation was proposed, where the active oxygen species formed on the Ag surface from gaseous O_2 migrate to the CeO_2 surface via the interface, transform into O_n^{x-} species and then further migrate onto soot particles where oxidation occurs. The abundantly formed O_n^{x-} species migrate fast out to the external surface, and efficiently access to soot particles. This is the key factor for its distinguished soot oxidation performance and insensitivity to the contact between catalyst and soot.

The CeO_2–Ag catalyst shows the abundant formation of active oxygen species due to the compatibility of the moderately large Ag particles (ca. 30 to 40 nm) and the extremely large interface area between the Ag and the CeO_2 particles due to the rice-ball morphology. This catalyst also exhibits fast migration of the active oxygen species due to the extremely large interface area. Therefore, it is concluded that the rice-ball morphology of the CeO_2–Ag catalyst is optimal for the formation and migration of active oxygen species for soot oxidation.

Acknowledgements

The authors thank K. Domen at the department of chemical system engineering, the university of Tokyo, for helpful discussions.

References

[1] B.A.A.L. van Setten, M. Makkee, J.A. Moulijn, Catal. Rev. Sci. Eng. 43 (2001) 489.
[2] K. Hinot, H. Burtscher, A.P. Weber, G. Kasper, Appl. Catal. B 71 (2007) 271.
[3] B.J. Cooper, J.E. Thoss, SAE Paper 890404 (1989).
[4] K.N. Pattas, C.C. Michalopoulou, SAE Paper 920362 (1992).
[5] G. Lepperhoff, H. Luders, P. Barthe, J. Lemaire, SAE Paper 950369 (1995).
[6] J.P.A. Neeft, M. Makkee, J.A. Moulijn, Appl. Catal. B 8 (1996) 57.
[7] C. Badini, G. Saracco, V. Serra, Appl. Catal. B 11 (1997) 307.
[8] G. Saracco, C. Badini, N. Russo, V. Specchia, Appl. Catal. B 21 (1999) 233.
[9] G. Neri, G. Rizzo, S. Galvagno, A. Donato, M.G. Musolino, R. Pietropaolo, Appl. Catal. B 42 (2003) 381.
[10] H. An, C. Kilroy, P.J. McGinn, Catal. Today 98 (2004) 423.
[11] C.A. Querini, L.M. Cornaglia, M.A. Ulla, E.E. Miro, Appl. Catal. B 20 (1999) 165.

[12] M.L. Pisarello, V. Milt, M.A. Peralta, C.A. Querini, E.E. Miro, Catal. Today 75 (2002) 465.

[13] R. Jimenez, X. Garcia, C. Cellier, P. Ruiz, A.L. Gordon, Appl. Catal. A 314 (2006) 81.

[14] D. Fino, N. Russo, G. Saracco, V. Specchia, J. Catal. 217 (2003) 367.

[15] B.A.A.L. van Setten, C.G.M. Spitters, J. Bremmer, A.M.M. Mulders, M. Makkee, J. A. Moulijn, Appl. Catal. B 42 (2003) 337.

[16] A. Bueno-Lopez, K. Krishna, M. Makkee, J.A. Moulijn, J. Catal. 230 (2005) 237.

[17] K. Krishna, A. Bueno-Lopez, M. Makkee, J.A. Moulijn, Appl. Catal. B 75 (2007) 189.

[18] K. Krishna, A. Bueno-Lopez, M. Makkee, J.A. Moulijn, Appl. Catal. B 75 (2007) 210.

[19] E. Aneggi, M. Boaro, C. de Leitenburg, G. Dolcetti, A. Trovarelli, Catal. Today 112 (2006) 94.

[20] E. Aneggi, M. Boaro, C. de Leitenburg, G. Dolcetti, A. Trovarelli, J. Alloys Compd. 408-412 (2006) 1096.

[21] E. Aneggi, C. de Leitenburg, G. Dolcetti, A. Trovarelli, Catal. Today 114 (2006) 40.

[22] P. Palmisano, N. Russo, P. Fino, D. Fino, C. Badini, Appl. Catal. B 69 (2006) 85.

[23] T. Masui, K. Minami, K. Koyabu, N. Imanaka, Catal. Today 117 (2006) 187.

[24] E. Aneggi, J. Llorca, C. de Leitenburg, G. Dolcetti, A. Trovarelli, Appl. Catal. B 91 (2009) 489.

[25] M. Machida, Y. Murata, K. Kishikawa, D. Zhang, K. Ikeue, Chem. Mater. 20 (2008) 4489.

[26] K. Shimizu, H. Kawachi, A. Satsuma, Appl. Catal. B 96 (2010) 169.

[27] S.R. Seyedmonir, D.E. Strohmayer, G.J. Guskey, G.L. Geoffroy, M.A. Vannice, J. Catal. 93 (1985) 288.

[28] T. Kayama, K. Yamazaki, H. Shinjoh, J. Am. Chem. Soc. 132 (2010) 13154.

[29] F. Dong, A. Suda, T. Tanabe, Y. Nagai, H. Sobukawa, H. Shinjoh, M. Sugiura, C. Descorme, D. Duprez, Catal. Today 90 (2004) 223.

[30] F. Dong, A. Suda, T. Tanabe, Y. Nagai, H. Sobukawa, H. Shinjoh, M. Sugiura, C. Descorme, D. Duprez, Catal. Today 93-95 (2004) 827.

[31] X. Zang, K.J. Klabunde, Inorg. Chem. 31 (1992) 1706.

[32] X. Li, A. Vannice, J. Catal. 151 (1995) 87.

[33] L. Gang, B.G. Anderson, J. van Grondelle, R.A. van Santen, Appl. Catal. B 40 (2003) 101.

[34] C.T. Campbell, Surf. Sci. 157 (1985) 43.
[35] S.N. Trukhan, V.P. Ivanov, B.S. Bal'zhinimaev, Kinet. Catal. 38, (1997) 565.
[36] G.W. Busser, O. Hinrichsen, M. Muhler, Catal. Lett. 79 (2002) 49.
[37] M.J. Lippits, A.C. Gluhoi, B.E. Nieuwenhuys, Catal. Today 137 (2008) 446.
[38] B.S. Bal'zhinimaev, Kinet. Catal. 40 (1999) 795.
[39] A. Takahashi, N. Hamakawa, I. Nakamura, T. Fujitani, Appl. Catal. A 294 (2005) 34.
[40] G.I.N. Waterhouse, G.A. Bowmaker, J.B. Metson, Appl. Catal. A 265 (2004) 85.
[41] L. Kundakovic, M. Flytzani-Stephanopoulos, Appl. Catal. A 183 (1999) 35.
[42] J.C. Wu, P. Harriott, J. Catal. 39 (1975) 395.
[43] X.E. Verykios, F.P. Stein, R.W. Coughlin, J. Catal. 66 (1980) 368.
[44] C. Li, Y. Song, Y. Chen, Q. Xin, X. Han, W. Li, Stud. Surf. Sci. Catal. 112 (1997) 439.
[45] D. Duprez, Stud. Surf. Sci. Catal. 112 (1997) 13.
[46] D. Martin, D. Duprez, J. Phys. Chem. 100 (1996) 9429.

Chapter 6

Remote oxidation of PM separated by ash deposition via PM oxidation catalyst

Abstract

One of the main issues of catalyzed diesel particulate filter is ash deposition onto catalyst coated on the filter. The effects of ash deposition on the catalysis of soot oxidation with gaseous oxygen were determined using multi-layered samples composed of a catalyst, an ash material and soot particles deposited on a thin cordierite plate in sequence. Catalysts composed of silver and ceria were used to enhance the oxidation of soot particles separated from the catalyst by ash deposits of either alumina or calcium sulfate. The effectiveness of remote soot oxidation was found to extend across an ash thickness of more than 50 μm for both ash materials, although a catalyst composed only of ceria did not show any catalytic performance for remote soot oxidation. Using an $^{18}O/^{16}O$ isotopic exchange reaction and electron spin resonance techniques, a possible mechanism for this phenomenon was proposed, whereby a superoxide ion (O_2^-) species generated on the catalyst surface first migrates to the ash surface and then to the soot particles, which it subsequently oxidizes.

Keywords; Soot oxidation, Ash deposition, Remote catalysis, Silver, Ceria

1. Introduction

Emission control technologies for nitrogen oxides (NO_x) and particulate matter (PM; mainly ‘soot’) is strongly required for clean diesel-powered vehicles. Recently development in diesel particulate filter (DPF) technology is the washcoating of the base filter element with mixture of catalytic agents or so called catalyzed diesel particulate filter (C-DPF), which is regarded as the most promising solution, especially for removal of PM in exhausts [1].

Many types of catalysts and technologies for the C-DPF based on different principles have been reported so far. They can be classified broadly into two categories depending on whether utilizing NO_x in exhausts or not for soot oxidation. In the category utilizing NO_x, which possesses higher oxidation ability than gaseous O_2, continuously regenerating trap (CRT) system, where NO is oxidized to NO_2 on a platinum catalyst and this NO_2 oxidizes soot trapped in the DPF at temperatures from 200 to 450 °C, has been developed by Johnson Matthey [2]. Teraoka et al. reported that

perovskite-type and spinel-type oxides showed higher catalytic activity for simultaneous NO_x–soot removal than simple metal oxides [3,4]. Diesel particulate–NO_x reduction (DPNR) system, which is capable of simultaneous abatement of PM and NO_x in diesel exhausts by using surface nitrate species generated from gaseous NO, has been developed by Toyota [5,6]. Recently, Makkee et al. and Bueno-López et al. have reported that rare-earth modified CeO_2 and ceria–zirconia catalysts present greater activity than pure CeO_2 for soot oxidation by NO_x/O_2 [7,8]. However, the above category utilizing NO_x depends on the amount of NO_x in the exhausts. A new trend in diesel engines to decrease NO_x emission could restrict their application [6]. The category utilizing only O_2, not using NO_x, for soot oxidation would be preferred for the next generation of catalysts and technologies. In this category, many researchers have reported molten salt catalysts, which can wet the soot and therefore decrease the soot oxidation temperature [9−11]. Moreover, CeO_2-based catalysts have been reported to have good activity for soot oxidation with O_2 [12−14]. Recently, Machida et al. and Shimizu et al. have reported that Ag loading onto CeO_2 enhances the activity for soot oxidation with O_2 [15,16]. Aneggi et al. have reported that the addition of Ag to ZrO_2 and Al_2O_3 results in very active catalysts for soot oxidation by O_2 [17].

As an alternative to catalysts washcoated on DPFs, organometallic fuel additives, also known as fuel-borne catalysts (FBCs), lead to the formation of catalyst-doped soot during combustion in the engine, which lowers the soot oxidation temperature in the DPF [18]. As a matter of fact, the PSA Peugeot fuel additive system for passenger cars has been commercialized in the market since 2000, and there seems no operating problem.

One of the main issues of the C-DPF is ash deposition onto catalysts coated on the filter. PM is composed of mainly soot, soluble organic fraction (SOF), sulfates, and slightly inorganic metal materials (ash). Ash generally is generated from lubricant oil additives, engine cleaning detergents, trace metals in diesel fuels, engine wear metals and corrosion products [1]. Although soot and SOF are oxidized over the catalysts, ash could remain as fine particles during regeneration process. After repetitive regenerations, the ash would deposit as a layer on the filter walls, and subsequent soot would be trapped on the ash layer. As a result, the ash layer form a barrier separating the soot from the catalyst coated on the DPF walls. In soot oxidation by O_2 over catalyst, contact between the catalyst and the soot is necessary, since the reaction processes take place at the three-phase boundary between the two solids and the gaseous O_2. Therefore, even just a thin ash layer may interrupt the contact between the catalyst and the soot, and the catalytic performance of C-DPF for soot oxidation could decrease drastically.

Catalytic soot oxidation with gaseous O_2 is basically a solid-catalyzed gas–solid reaction. This heterogeneous catalysis is very challenging since it has an inherent drawback: loss of contact between the solid catalyst and the solid reactant as unreactive inorganic materials (ash) are deposited onto the catalyst surface. Therefore, it is very meaningful to verify scientifically if remote catalytic soot oxidation can actually occur when a physical barrier of ash deposit exists between the catalyst and the solid soot, because the oxygen species need to diffuse and transfer throughout the above disjunctive space and still remain active onto the soot particles. Meanwhile, this information is also very valuable for the development of PM removal technology, which closely relates to tolerance for ash deposition and longevity of the whole system. Unfortunately, how the ash deposit exactly affects the activity of catalytic soot oxidation and the related information are not available in the publications so far.

An innovative CeO_2–Ag catalyst exhibited exceptional performance of soot oxidation by gaseous O_2 in our previous research [19]. This catalyst has a unique agglomeration morphology with diameter of about 100 nm, consisting of metallic Ag particles in the center surrounded by fine CeO_2 particles, called ‘rice-ball morphology’. We concluded that the compatibility of the moderately large Ag particles (ca. 30–40 nm) and the extremely large interface between the Ag and CeO_2 particles due to this morphology causes its excellent catalytic performance for soot oxidation [20]. As a consecutive study leading to actual application, we managed to prepare multi-layered samples composed of a catalyst, an ash material of varied thickness and soot, all deposited in sequence on a thin cordierite plate, and then verify if the gaseous oxygen can actually oxidize the solid soot and how exactly the activity varies on the ash-deposited CeO_2–Ag catalyst on a quantitative base. The involved reaction mechanism was further elucidated by use of an isotopic ^{18}O tracer technique to characterize the migration of oxygen species, and electron spin resonance (ESR) to specify the oxygen species. Hopefully, we can obtain some valuable information and hints for the development of a soot oxidation catalyst for C-DPF with a high tolerance for ash deposition.

2. Experimental

2.1. Catalyst preparation

The CeO_2–Ag catalyst was prepared using a coprecipitation-based method. A 150 mL portion of an aqueous solution of $AgNO_3$ (Toyo Chemical Industrial, 29.63 g) and $Ce(NO_3)_3{\cdot}6H_2O$ (Wako Pure Chemical Industries, 50.49 g) was rapidly added (in less than one second) to a dilute ammonia solution (35.6 g of a 25% ammonia solution

diluted with 100 mL of water) using a rotary stirrer operating at 350 rpm, at room temperature. The mixture was stirred for 1 min and the coprecipitate was then uniformly heated by steam in an autoclave at 120 °C for 10 min and subsequently separated by centrifugation and calcined at 500 °C for 5 h in air. The Ag content of the obtained CeO_2–Ag catalyst was 39 wt.%. The CeO_2 catalyst was obtained by the calcination of a commercial CeO_2 powder (Rhodia, BET surface area 150 m^2/g) at 600 °C for 50 h, generating a final BET surface area of 78 m^2/g. A Ag/CeO_2 catalyst in which the silver content was 10 wt.% was prepared by impregnation of the CeO_2 catalyst with an aqueous $AgNO_3$ solution followed by calcination at 500 °C for 5 h in air. This catalyst was found to exhibit higher catalytic performance for soot oxidation than the Ag/CeO_2 catalyst with 39 wt.% silver content [20]. A more detailed description of the catalyst preparation processes is given elsewhere [19].

An ^{18}O-exchanged CeO_2–Ag catalyst was prepared by introducing 5650 Pa of pure $^{18}O_2$ (99.2% ^{18}O, ICON) to the CeO_2–Ag catalyst at 500 °C for 1 h followed by evacuating the sample at the same temperature in a recirculated reactor (ca. 100 cm^3) used in a previous study [21]. This sequence was repeated eight times. The ^{18}O-exchange ratio in the catalyst was calculated by analyzing $^{18}O^{16}O$ and $^{16}O_2$ molecules released from the catalyst into the gas phase using a quadrupole mass spectrometer (Q-MS) coupled to the recirculated reactor and was found to be more than 96%.

2.2. Multi-layered sample preparation

Multi-layered samples consisting of a catalyst, an ash material of varied thickness and soot deposited on a cordierite plate were employed to examine remote catalytic soot oxidation (Fig. 1). It is well known that ash spans a wide range in composition, depending on factors such as engine type, driving conditions, fuel additives, lubricant oil, and metallurgy of the exhaust lines. It generally consists of one or more the following components; sulfates, phosphates or other oxides of calcium, zinc and magnesium, as well as oxides of metals such as iron, copper, chromium, nickel and aluminum [1]. To avoid the contact between the catalyst and the soot, alumina and calcium sulfate are chosen as ash materials, because they are inert materials and should have no catalytic performance for soot oxidation.

A commercial Al_2O_3 powder (α-Al_2O_3, Wako Pure Chemical Industries, BET surface area 7.8 m^2/g) was used as the ash material without treatment. A $CaSO_4$ powder with a BET surface area of 3.2 m^2/g obtained by the calcination of a commercial $CaSO_4 \cdot 0.5H_2O$ powder (Wako Pure Chemical Industries, 3.6 m^2/g) at 700 °C for 5 h

was also used as an ash material. A carbon black powder (Degussa, Printex V, 85 m^2/g) was employed as model soot. Separate ethanol dispersions of the catalyst powder, the ash material and the soot were obtained by adding 0.2 g of the desired material to 50 mL of ethanol and agitating in an ultrasonic bath. As the initial step in forming a test specimen, several drops of the ethanol dispersion of the catalyst were placed onto a square cordierite plate (1 mm thick and 15 mm in length) which was then dried at 110 °C for 1 h to evaporate the ethanol. This sequence was repeated until the concentration of catalyst on the plate reached the targeted value of 1.4 mg/cm^2. The same procedure was subsequently performed by applying an ash solution in ethanol until various targeted weights were deposited, based on the desired thickness of the ash layer. Last, the soot dispersion in ethanol was applied in the same manner to a concentration of 0.3 mg/cm^2, following which the sample was dried at 110 °C for 16 h to completely remove residual ethanol. Multi-layered samples without catalysts were also prepared and tested as references.

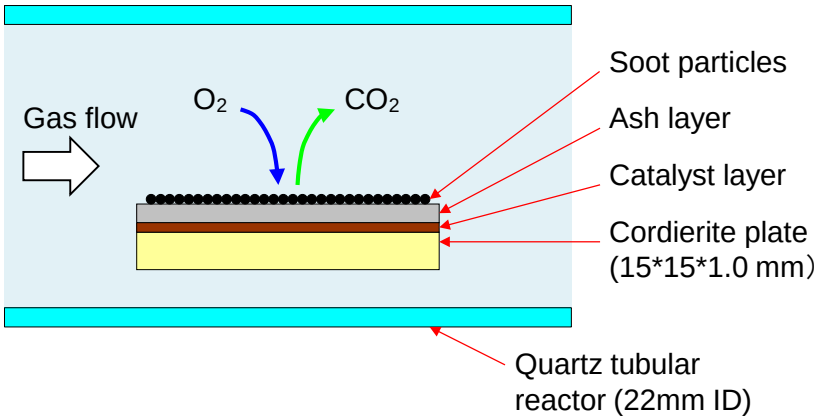

Fig. 1. Schematic of a test specimen consisting of a catalyst layer, an ash layer and a soot particle layer, all deposited on a square cordierite plate. The sample is installed in a quartz tubular reactor on a quartz bead bed.

2.3. Catalytic performance evaluation

The catalytic performance of each multi-layered test specimen for remote soot oxidation was evaluated by temperature-programmed oxidation (TPO) of the specimen (Fig. 1). Specimens were placed inside a quartz tubular reactor (22 mm ID). A thermocouple was positioned in contact with the bottom of the sample to monitor the reaction temperature and a 10% O_2/He atmosphere flowed at a rate of 60 mL/min. TPO profiles for soot oxidation were typically recorded at a heating rate of 20 °C/min over

the range of 30 to 810 °C. The concentrations of CO_2, CO and O_2 in the effluent gas flow were analyzed online using a quadrupole mass spectrometer (Q-MS, Ulvac, RG-102).

Some preliminary experiments to examine the diffusion's influence was conducted by varying the oxygen flow rate, oxygen concentration, and flow direction (from side, top or bottom of the multi-layered sample). The catalytic performances of multi-layered samples with CeO_2–Ag catalyst turned out nearly the same, that is, no apparent influence from the diffusion (including the back diffusion and reverse flow) was detected. For the cordierite plate was very dense, oxygen could not penetrate from the bottom of the cordierite plate to the catalyst layer. The multi-layered samples are exposed or surrounded by the same atmosphere (10% O_2/He). Under the above reaction condition, the soot oxidation is fundamentally determined by the adsorption and activation of oxygen on the catalyst surface, and the migration of the activated oxygen species across the ash layer to the soot particles, not by the oxygen diffusion in the gas phase, although theoretically the oxygen diffusion's influence could not completely denied.

The apparent activation energy of the soot oxidation reaction was determined by the Ozawa method [22] using the following expression:

$$\log \alpha = -0.4567\, E_a/RT_x + \text{constant}$$

where α is the applied heating rate, T_x is the temperature corresponding to a given percentage of carbon conversion and E_a is the apparent activation energy in kJ/mol. E_a can be estimated from the slope of the least-squares straight line fit to a plot of $\log \alpha$ versus $1/T_x$. Heating rates of 10, 20, 30 and 40 °C/min were used to obtain the necessary data to calculate apparent activation energy.

2.4. Catalyst characterization

BET surface areas were measured by single-point N_2 adsorption at −196 °C using an automatic surface area analyzer (Microdata, MS4232II) after pretreatment at 200 °C for 20 min.

Elemental distribution in the multi-layered samples was measured by electron probe microanalysis (EPMA) using a JEOL JXA-8200. The ash layers were peeled from the multi-layered samples and fixed in an epoxy resin (Struers, EpoFix), which was then cut to allow examination of the cross section. The elemental compositions of the ash layers were determined with an energy dispersive X-ray analyzer (EDX).

Electron spin resonance (ESR) analysis was conducted using a Bruker ESP350E spectrometer operating at 9.47 GHz. The multi-layered samples could not be directly analyzed by ESR owing to their size, and so test specimens consisting of mixtures of the catalyst and the ash material were instead prepared to simulate multi-layered samples with an ash layer thickness of approximately 100 μm. To prepare these specimens, the catalyst and ash powders were first separately pressed into pellets 180–210 μm in diameter, then combined in a weight ratio of 1:1, mixed by shaking in a bottle and finally pressed together into pellets 710–1000 μm in diameter. The obtained samples incorporated an interface between the catalyst and the ash material, with each continuous portion at a distance of about 100 μm from the interface. Samples of pure catalyst and ash materials were also pressed into pellets 710–1000 μm in diameter and analyzed as reference specimens.

During ESR analysis, a 20 mg portion of the sample was placed in a 3.5 mm diameter quartz ESR tube attached to a high-vacuum stopcock which allowed pre-treatment and adsorption of various gases. After the pre-adsorption of 20% O_2/N_2 at 600 °C for 30 min, the test sample was cooled to room temperature, purged with N_2 for 30 min and finally exposed to a 3% H_2/N_2 flow at 30 mL/min for 3 min at 250 °C, during which time its ESR spectrum was recorded at 20 K. Spin density was determined from the double integration of derivative ESR signals and by comparison with the weak pitch sample.

3. Results and discussion

3.1. Configuration of multi-layered samples

Fig. 2a shows a microscope image of the cross section of a multi-layered sample incorporating the CeO_2–Ag catalyst and an Al_2O_3 ash layer. It can be seen that the brown catalyst layer (CeO_2–Ag), the white ash layer (Al_2O_3) and black soot particles were all deposited on the cordierite plate in an orderly fashion and it is also evident that there is no contact between the catalyst and the soot. Fig. 2b shows the cross section of a multi-layered sample with the CeO_2–Ag catalyst and a $CaSO_4$ ash layer. Although the $CaSO_4$ ash layer exhibits some voids, the general structure of this sample is otherwise similar to that of the Al_2O_3 specimen. The porosities of the Al_2O_3 and $CaSO_4$ layers were determined to be 36 and 22%, respectively, indicating that they would permit the diffusion of gaseous reactants and products.

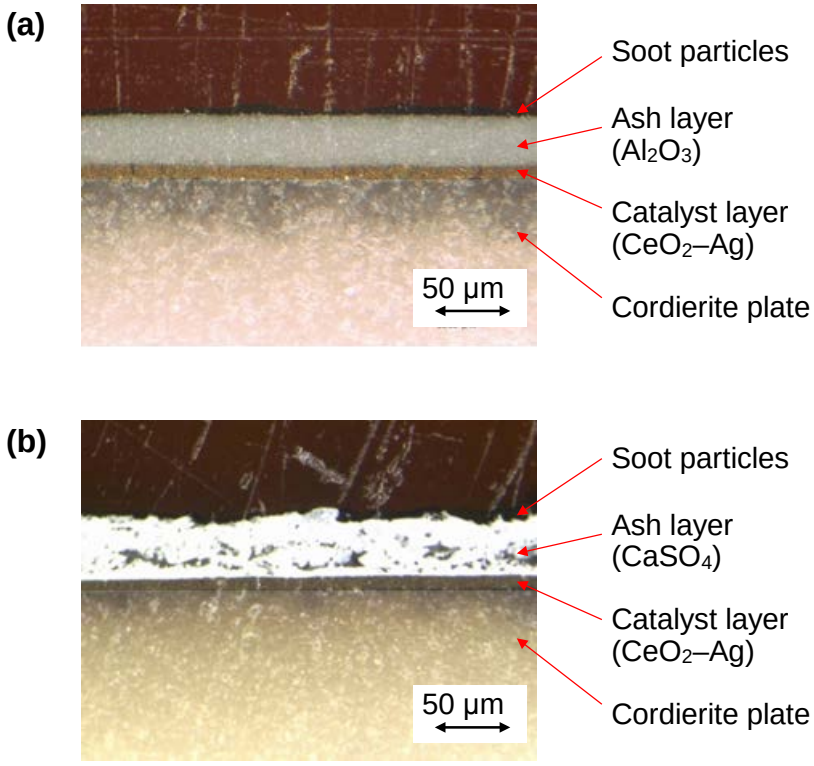

Fig. 2. Microscope images of the cross sections of **(a)** a multi-layered sample with an Al_2O_3 ash layer and a CeO_2–Ag catalyst layer and **(b)** a multi-layered sample with a $CaSO_4$ ash layer and a CeO_2–Ag catalyst layer.

The multi-layered samples were exposed to temperatures of up to 810 °C during catalytic performance evaluation by TPO. Electron probe microanalysis images of a multi-layered sample incorporating the CeO_2–Ag catalyst and an Al_2O_3 ash layer before and after TPO are presented in Figs. 3a and 3b. The Ag content in the Al_2O_3 ash layer was 0.077 wt.%, which indicates that only a very small quantity of silver migrated to the ash layer during TPO analysis at 810 °C. Fortunately, the addition of 0.1 wt.% silver to the Al_2O_3 ash is not sufficient to impart any activity for soot oxidation to the ash layer and hence any observed soot oxidation can still be considered to have occurred remotely via the catalyst layer.

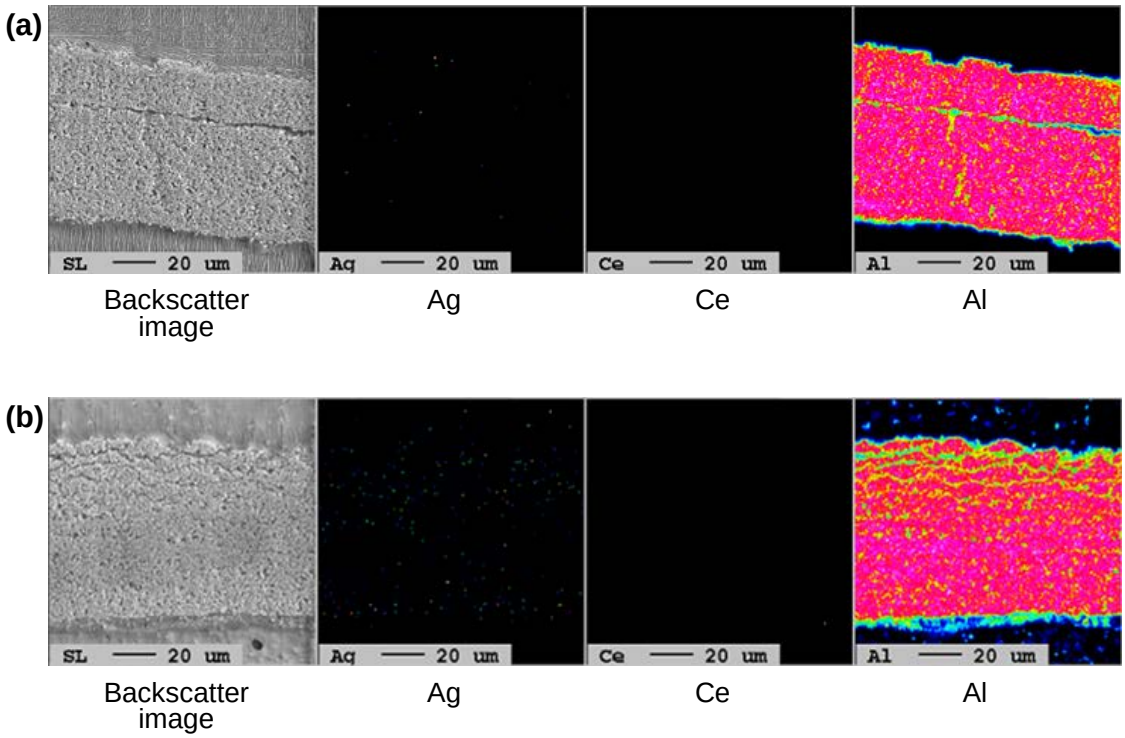

Fig. 3. EPMA micrographs showing Ag, Ce and Al (with corresponding backscatter images) in the Al_2O_3 ash layers of multi-layered samples **(a)** before and **(b)** after TPO trials at temperatures up to 810 ^oC.

3.2. Catalytic performance for remote soot oxidation

Figs. 4a and 4b show TPO profiles for soot oxidation acquired using a 10% O_2/He gas flow with Al_2O_3 and $CaSO_4$ layers, respectively, deposited on the CeO_2–Ag catalyst. With both ash materials, the application of an ash layer of 25 or 50 μm allowed soot oxidation to occur via the CeO_2–Ag catalyst at temperatures below those required in the absence of a catalyst. The CeO_2–Ag catalyst therefore clearly exhibits catalytic performance for remote soot oxidation, since in these samples it has no direct contact with the soot particles. The temperature corresponding to 50% conversion of the soot (T_{50}) was used as a measure of catalyst performance and is plotted as a function of the Al_2O_3 and $CaSO_4$ ash layer thicknesses in Figs. 5a and 5b, respectively. By comparing the T_{50} values for soot oxidation without the catalyst, the effect of remote oxidation by the CeO_2–Ag catalyst is found to extend to a thickness of more than 50 μm for both ash materials. The soot particles spontaneously oxidized at temperatures above 600 °C and so the remote oxidation activity of the CeO_2–Ag catalyst appears to be lost around 100 μm of ash thickness. However, it should be noted that the CeO_2–Ag catalyst also lowers the temperature required for the oxidation of soot when separated by an ash layer more

than 50 µm in thickness, and such lowered temperatures can have some significant benefits when treating PM in diesel exhaust gases with catalyzed diesel particulate filters, as noted above [1].

Figs. 6a and 6b show the apparent activation energies as a function of the deposition thickness of the Al_2O_3 and $CaSO_4$ layers, respectively, for soot oxidation with the CeO_2–Ag catalyst. Based on comparisons with the apparent activation energy for soot oxidation without the catalyst, these results suggest that the remote oxidation activity of the CeO_2–Ag catalyst extends to a thickness of more than 50 µm for both ash materials, consistent with the results obtained from the T_{50} values.

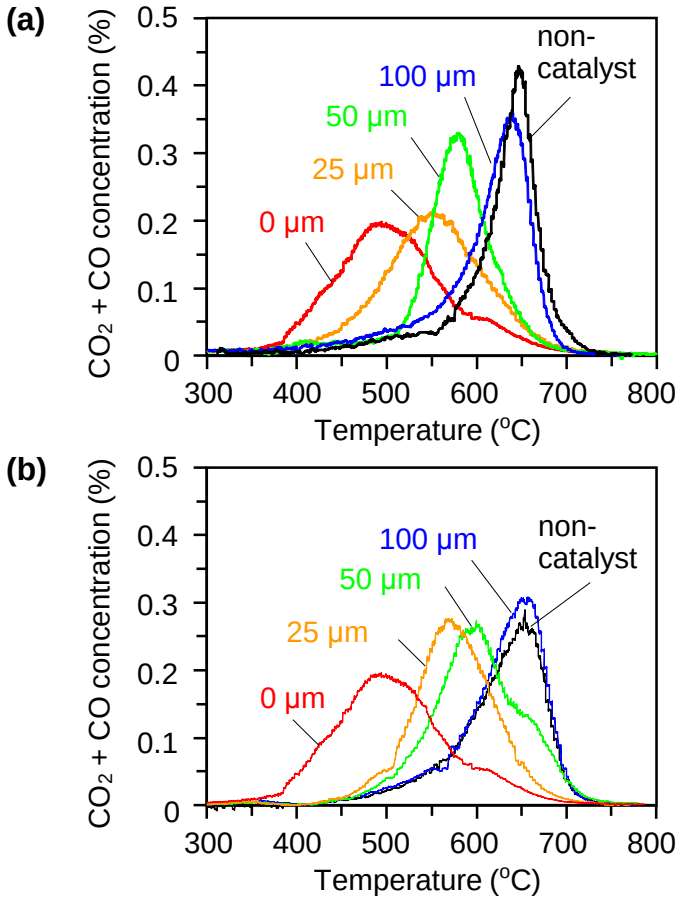

Fig. 4. TPO profiles for soot oxidation using **(a)** Al_2O_3 and **(b)** $CaSO_4$ ash layers of varying thicknesses deposited on a CeO_2–Ag catalyst. The values (in micrometers) in the figures denote the ash layer thicknesses.

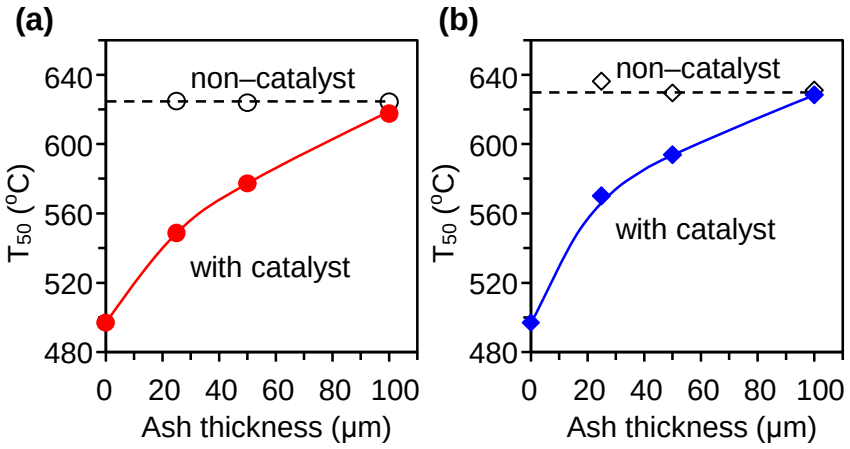

Fig. 5. Catalytic performance during soot oxidation as indicated by T_{50} as a function of the **(a)** Al_2O_3 and **(b)** $CaSO_4$ ash layer thickness over a CeO_2–Ag catalyst.

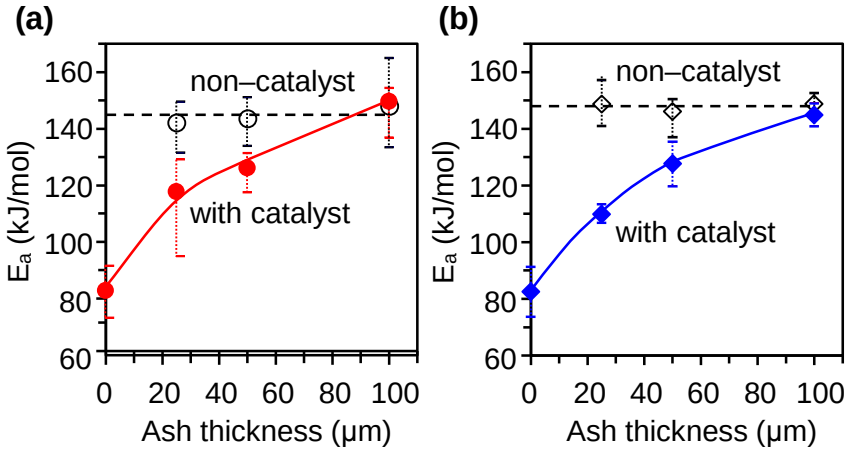

Fig. 6. Apparent activation energies during soot oxidation as a function of the **(a)** Al_2O_3 and **(b)** $CaSO_4$ ash layer thickness over a CeO_2–Ag catalyst.

To identify the oxygen source in this remote catalytic soot oxidation, oxygen isotopic tracer analysis was conducted during TPO assessments of multi-layered samples containing CeO_2–Ag catalyst which incorporated ^{18}O atoms (more than 96%) together with an Al_2O_3 ash layer of 50 μm. Fig. 7a shows the generation of $^{18}O_2$ and $^{18}O^{16}O$ molecules at temperatures between 350 and 600 °C during the TPO process. This result indicates that gaseous oxygen is adsorbed, dissociates on the catalyst and is exchanged with oxygen in the catalyst [21]. Fig. 7b shows that the production of $C^{18}O_2$

and $C^{18}O^{16}O$ is greater than that of $C^{16}O_2$ over a similar temperature range, demonstrating that oxygen derived from the catalyst has a higher activity for soot oxidation than excess gaseous oxygen. Oxygen species activated on the catalyst therefore dominate the process of soot oxidation through the ash layers at temperatures above 350 °C, validating our contention that remote soot oxidation occurs via the CeO_2–Ag catalyst.

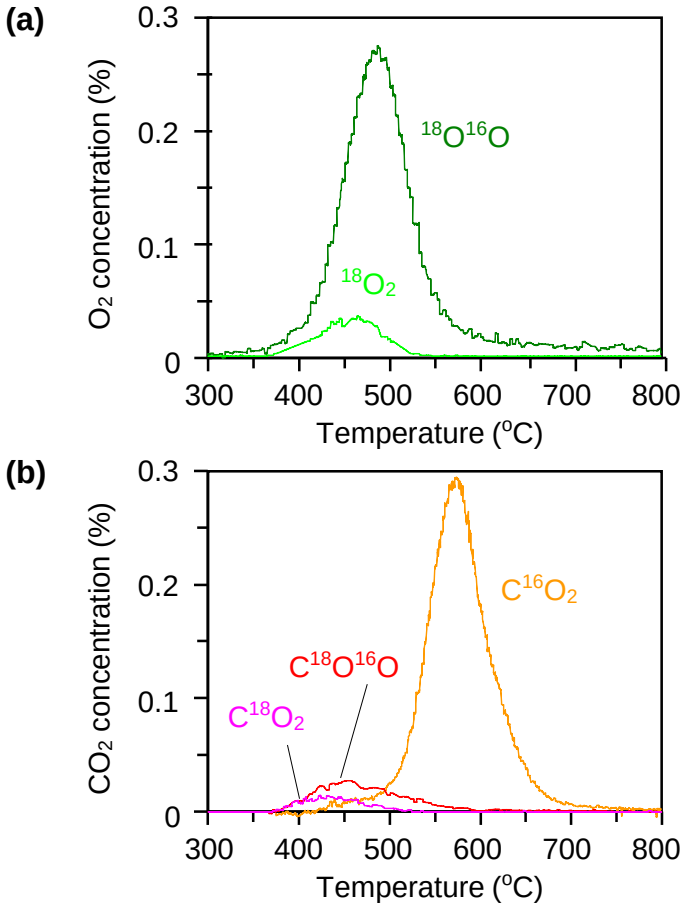

Fig. 7. Generation of **(a)** O_2 and **(b)** CO_2 species, respectively, from a multi-layered sample with an ^{18}O-exchanged CeO_2–Ag catalyst and an Al_2O_3 ash layer of 50 µm during TPO trials.

Figs. 8a and 8b show the TPO profiles for soot oxidation over an ash layer deposited on Ag/CeO_2 and CeO_2 catalysts, respectively. Remote catalytic oxidation of soot was observed in the samples with the Ag/CeO_2 catalyst but not in those with the CeO_2 catalyst, even in the case of a 15 µm ash deposit. This suggests that remote soot

oxidation requires a catalyst composed of both Ag and CeO_2. The catalytic performances indicated by the T_{50} values as a function of the thickness of the deposited ash layer for the CeO_2–Ag, Ag/CeO_2 and CeO_2 catalysts are shown in Fig. 9. The effect of remote oxidation by the Ag/CeO_2 catalyst was found to extend over a thickness of more than 50 μm, however, it was not as active as that of the CeO_2–Ag catalyst. The observation that the CeO_2 catalyst loses its catalytic performance as a result of increased ash deposition confirms the absence of any contact between the catalyst and the soot particles, a confounding effect which might have occurred during sample preparation as soot particles penetrated the ash layer.

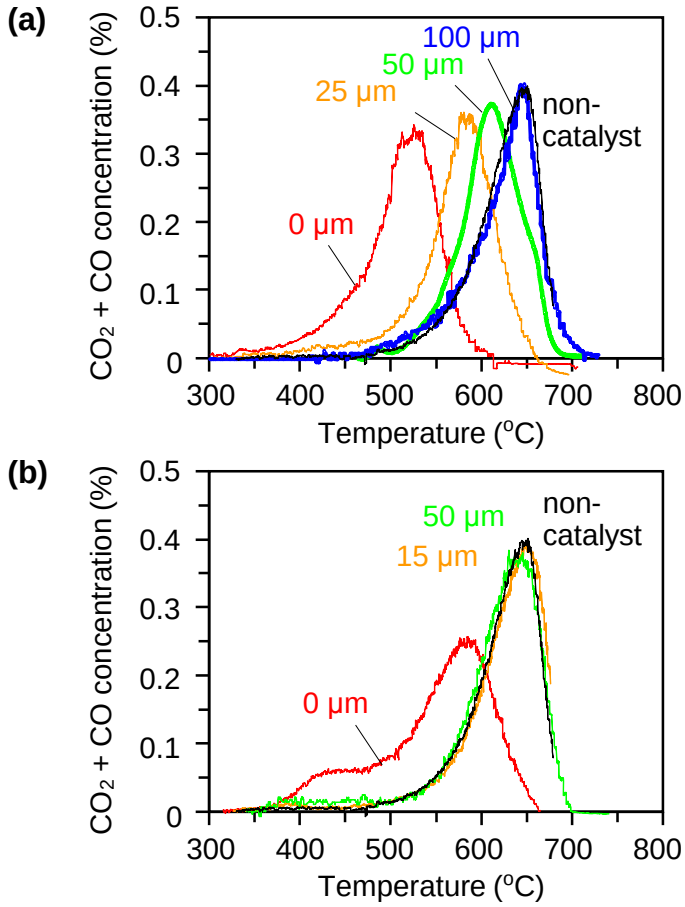

Fig. 8. TPO profiles for soot oxidation on Al_2O_3 layers of varying thicknesses deposited on **(a)** Ag/CeO_2 and **(b)** CeO_2 catalysts. The values (in micrometers) in the figures denote the ash layer thicknesses.

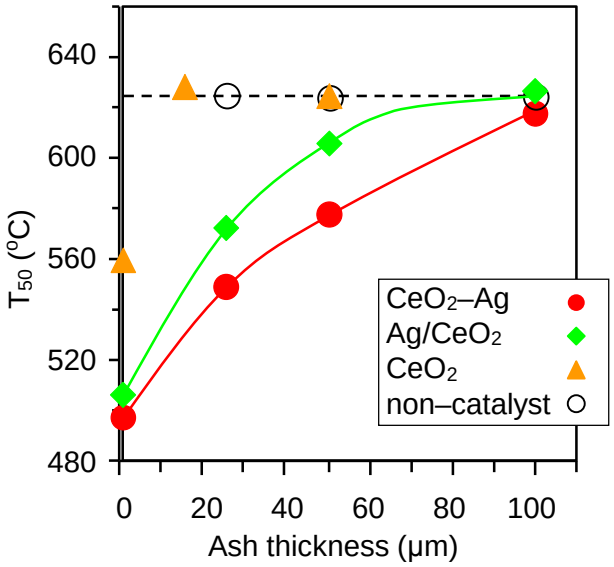

Fig. 9. Catalytic performance indicated by T_{50} as a function of Al_2O_3 ash layer thicknesses over CeO_2–Ag, Ag/CeO_2 and CeO_2 catalysts.

3.3. Active oxygen species by ESR

Utilizing oxygen temperature-programmed desorption and ESR techniques, we found that the oxygen species adsorbed on the Ag surface under oxidative conditions are transformed into superoxide (O_2^-) species on the CeO_2 surface under weak reductive conditions and that the increased formation of the O_2^- species leads to a higher catalytic performance for soot oxidation [20]. The compatibility of the moderately large Ag particles (ca. 30–40 nm) and the extremely large interface between the Ag and CeO_2 particles in the CeO_2–Ag catalyst leads to the abundant formation of the adsorbed oxygen species and the fast transformation into the O_2^- species. It is known that a catalyst in contact with the soot is exposed to local reductive conditions during soot oxidation [13]. We therefore proposed a mechanism for soot oxidation in which the active oxygen species formed on the Ag surface from gaseous O_2 migrate to the CeO_2 surface via the interface, transform into O_2^- species, and then further migrate onto soot particles where oxidation occurs. The spin densities of the O_2^- species formed on the CeO_2–Ag, Ag/CeO_2 and CeO_2 catalysts under weak reductive conditions following oxidation were determined to be 0.83, 0.47 and 0.002 μmol/g, respectively [20]. This result is in good agreement with the catalytic performances for remote soot oxidation observed in this study. It has been reported that the oxidation of soot in the absence of contact with the catalyst generates CO through the formation of surface oxygen complexes [23]. About 35% of the oxidized soot on the multi-layered samples

without a catalyst was transformed into CO, whereas almost all of the oxidized soot (more than 95%) on the samples with a catalyst was converted to CO_2, irrespective of the thickness of the ash layer (for layers of 100 μm or less). Catalysts in the vicinity of, but not in direct contact with the soot can also experience local reductive conditions generating CO [13]. It is therefore very likely that the O_2^- species formed on the catalyst contribute to remote soot oxidation. It is noteworthy that the CeO_2 catalyst, which generates almost no O_2^- species, showed no catalytic performance for remote soot oxidation, even though it was active for the oxidation of CO. The oxidation of CO resulting from the soot via the catalyst and the subsequent elevation of the catalyst temperature by an exothermic effect cannot explain this result.

To further explore the role of the O_2^- species in remote soot oxidation, an ESR analysis was conducted using a mixture of the CeO_2–Ag catalyst and Al_2O_3 ash material which simulated a multi-layered sample and the results obtained were compared with those produced by pure, unmixed samples. The pure CeO_2–Ag sample showed ESR signals at $g_1 = 2.041$ and $g_2 = g_3 = 2.010$ when exposed to weak reductive conditions following oxidative conditions, as shown in Fig. 10a. These signals are all attributed to the O_2^- species on the CeO_2 surface [24,25]. The mixture of CeO_2–Ag and Al_2O_3 shows the same ESR signals (Fig. 10c) when subjected to the same procedure, although its spin density is approximately 25% that of the pure CeO_2–Ag sample (Table 1). This suggests that the O_2^- species on the catalyst diffuses through the interface between the catalyst and the ash material. The pure Al_2O_3 sample shows an ESR signal with $g = 2.008$ and a low spin density, as shown in Fig. 10b and Table 1, and is attributed to the O_2^- species on the Al_2O_3 surface [26]. Subtracting the spectrum of the pure CeO_2–Ag sample from that of the mixed CeO_2–Ag and Al_2O_3 sample also produces a spectrum similar to that of pure Al_2O_3 (Fig. 10d) although its spin density is higher (approximately 160% greater) than that of the pure Al_2O_3 sample (Table 1). These results, combined with the data obtained concerning the O_2^- species on the CeO_2 surface, strongly suggest that the O_2^- species on the catalyst migrates to the ash surface. The smaller total amount of the O_2^- species in the mixture compared with that in the pure CeO_2–Ag sample implies that some O_2^- is released from the ash material. Therefore, we can conclude that the O_2^- species formed on the catalyst migrates to the ash material and subsequently to the soot particles, where it oxidizes the soot (Fig. 11). We may also conclude that increased formation of the O_2^- species leads to higher performance for remote soot oxidation.

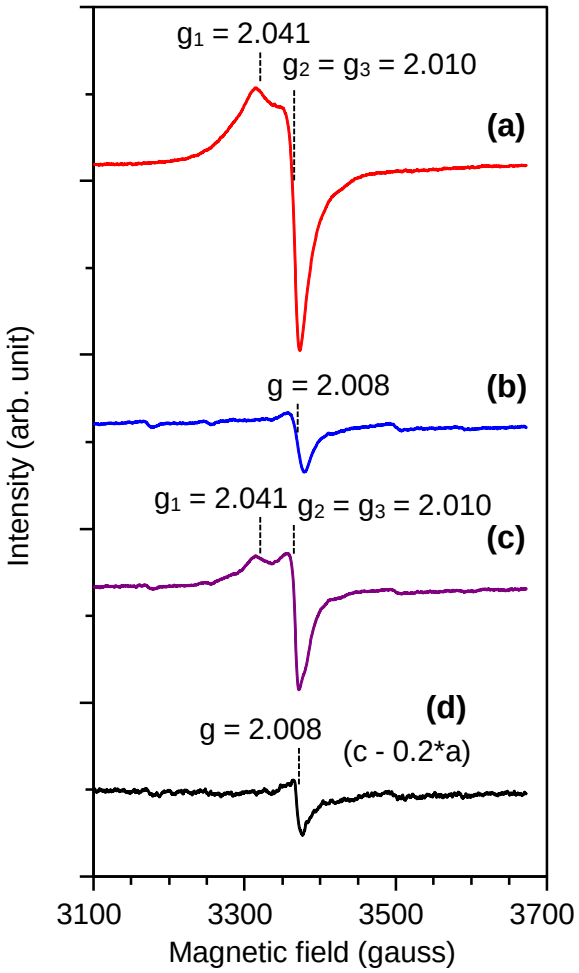

Fig. 10. ESR spectra of **(a)** pure CeO_2–Ag, **(b)** pure Al_2O_3 and **(c)** mixed CeO_2–Ag and Al_2O_3 samples. **(d)** ESR spectrum obtained by subtracting the spectrum of a pure CeO_2–Ag sample from that of a mixed CeO_2–Ag and Al_2O_3 sample.

Table 1. ESR signals, identified species and spin density values

Sample	ESR signals	Species	Spin density (μmol/g)
CeO_2–Ag catalyst	$g_1 = 2.041$ $g_2 = g_3 = 2.010$	O_2^- on CeO_2	0.830
Al_2O_3 ash	g = 2.080	O_2^- on Al_2O_3	0.050
Mixture of CeO_2–Ag catalyst and Al_2O_3 ash	$g_1 = 2.041$ $g_2 = g_3 = 2.010$	O_2^- on CeO_2	0.217
	g = 2.080	O_2^- on Al_2O_3	0.080

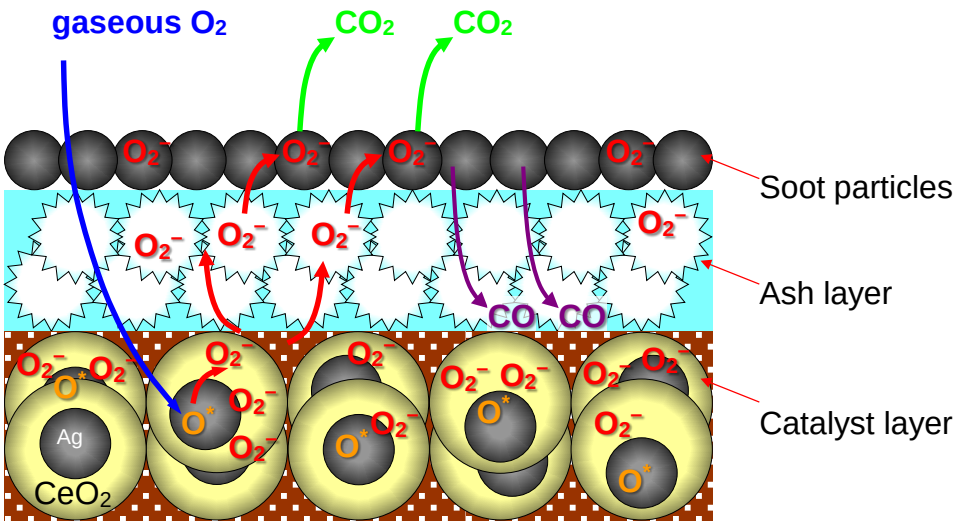

Fig. 11. Schematic mechanism for remote catalytic soot oxidation over a catalyst composed of Ag and CeO_2.

3.4. Mechanism and Characteristics of remote soot oxidation

The phenomenon in which active species initially adsorbed or formed on one surface are transported to another surface is well-known and is typically referred to as 'spillover' [27]. Hydrogen spillover in particular has been applied in many reactions and used to explain many interesting results, and is notable for its ability to occur over relatively long distances of several millimetres [28]. In contrast, considerably less attention has been paid to oxygen spillover [29,30]. Delmon et al. have discussed the importance of spillover oxygen in selective catalytic oxidation reactions [31] and other researchers have also studied this effect [32,33]. In these studies, oxygen spillover was observed on oxides of multi-valent metals, such as bismuth, molybdenum, antimony, iron and cerium, implicating oxygen anions (O^{2-}) as the spillover species. The distance over which oxygen spillover occurred was found to be limited to the size of the catalyst powders in multi-component catalysts, i.e. several micrometres.

However, ash materials with catalyzed diesel particulate filter are typically sulfates, phosphates or other oxides of calcium, zinc and magnesium originated from lubricant oil additives, instead of predominantly multi-valent metal oxides [1]. Moreover, these ash materials sometimes deposit in layers with thicknesses of several tens of micrometres. As a result, conventional oxygen spillover is not a useful mechanism when the catalyst and solid reactant are separated by ash deposition. Recently, remote photocatalytic oxidations have been reported, wherein the active oxygen species, such

as OH* and H_2O_2, migrate to solid reactants several millimetres away from the catalyst [34,35]. This effect, however, requires the application of external light energy to function. More recently, the platinum-catalyzed oxidation of soot separated by a SiO_2 layer was reported, and a transport mechanism for activated oxygen via the gas phase was tentatively proposed by Zeng et al. [36,37]. Their work indicated that soot could be catalytically oxidized only when the gas flowed through the layers in the sequence of catalyst, SiO_2 and soot. This is really different from the actual working condition of soot oxidation with an ash-deposited C-DPF. On the other hand, Roessner et al. reported that adsorbed hydrogen species could migrate (spillover) no matter how the gas flowed [38]. With reference to the above research, and the mechanism described in our previous study, we can speculate that the adsorbing activated oxygen species migrated and finally transferred onto the solid soot surface, nearly having nothing to do with the gas flow direction. Although further investigation is necessary, we believe that remote catalytic soot oxidation is ultimately determined by the mobility and activity of the adsorbed O_2^- species, as illustrated in Fig. 11. The phenomenon revealed in this research represents a new catalytic effect, suggesting a new promising solution to the challenging problem of ash deposition, that is, adopting the catalysts composed of Ag and CeO_2 to supply adequate O_2^- species with high mobility and activity onto the soot separated by ash deposits in C-DPF system [20].

4. Conclusions

Multi-layered samples consisting of a catalyst, an ash material of varied thickness and soot deposited on a cordierite plate were prepared and employed to examine remote catalytic soot combustion. The results demonstrated that the soot oxidation proceeds without direct contact between the catalyst and the soot without any external light or electric energy. A CeO_2–Ag catalyst prepared by the coprecipitation-based method and a Ag/CeO_2 catalyst prepared by impregnation exhibited catalytic performance for the remote oxidation of soot separated by the deposition of alumina or calcium sulphate, whereas a CeO_2 catalyst did not. The remote oxidation effect extended to more than 50 μm for both of the CeO_2–Ag and Ag/CeO_2catalysts, with higher effect on the CeO_2–Ag catalyst. Based on the results of ESR experiments, we proposed a mechanism for this phenomenon, in which a superoxide ion (O_2^-) species generated on the catalyst surface first migrates to the ash surface and then to the soot particles which it subsequently oxidizes.

At this point, the above phenomenon has not been found in the published reports so far, and the catalysts composed of Ag and CeO_2 exhibit superior performance with

regard to O_2^- species formation. These results also show that catalyzed diesel particulate filters containing these catalysts would have a significant tolerance for ash deposition and hence show great potential for incorporation into future clean diesel-powered vehicles.

Acknowledgement

We thank Dr. Y. Ikuta for helpful discussions regarding the mechanism of remote soot oxidation.

References

[1] B. A. A. L. van Setten, M. Makkee, J. A. Moulijn, Catal. Review 43 (2001) 489–564.

[2] B. J. Cooper, J.E. Those, SAE paper 890404, 1989.

[3] Y. Teraoka, K. Nakano, S, Kagawa, W. F. Shangguan, Appl. Catal. B 5 (1995) L181–L185.

[4] W. F. Shangguan, Y. Teraoka, S. Kagawa, Appl. Catal. B 8 (1996) 217–227.

[5] K. Nakatani, S. Hirota, S. Takeshima, K. Itoh, T. Tanaka, K. Dohmae, SAE paper 2002-01-0957, 2002.

[6] D. Fino, Sci. Technol. Adv. Mater. 8 (2007) 93–100.

[7] K. Krishna, A. Bueno- López, M. Makkee, J.A. Moulijn, Appl. Catal. B 75 (2007) 201–209.

[8] I. Atribak, A. Bueno-López, A. García-García, J. Catal. 259 (2008) 123–132.

[9] J.P.A. Neeft, M. Makkee, J.A. Moulijn, Appl. Catal. B 8 (1996) 57–78.

[10] G. Saracco, C. Badini, N. Russo, V. Specchia, Appl. Catal. B 21 (1999) 233–242.

[11] G. Neri, G. Rizzo, S. Galvagno, A. Donato, M.G. Musolino, R. Pietropaolo, Appl. Catal. B 42 (2003) 381–391.

[12] K. Krishna, A. Bueno-Lopez, M. Makkee, J.A. Moulijn, Appl. Catal. B 75 (2007) 189–200.

[13] E. Aneggi, M. Boaro, C. de Leitenburg, G. Dolcetti, A. Trovarelli, J. Alloys Compd. 408-412 (2006) 1096–1102.

[14] P. Palmisano, N. Russo, P. Fino, D. Fino, C. Badini, Appl. Catal. B 69 (2006) 85–92.

[15] M. Machida, Y. Murata, K. Kishikawa, D. Zhang, K. Ikeue, Chem. Mater. 20 (2008) 4489–4494.

[16] K. Shimizu, H. Kawachi, A. Satsuma, Appl. Catal. B 96 (2010) 169–175.

[17] E. Aneggi, J. Llorca, C. de Leitenburg, G. Dolcetti, A. Trovarelli, Appl. Catal. B 91 (2009) 489–498.
[18] G. Lepperhoff, H. Luders, P. Barthe, J. Lemaire, SAE Paper 950369, 1995.
[19] T. Kayama, K. Yamazaki, H. Shinjoh, J. Am. Chem. Soc. 132 (2010) 13154–13155.
[20] K. Yamazaki, T. Kayama, F. Dong, H. Shinjoh, J. Catal. 282 (2011) 289–298.
[21] F. Dong, A. Suda, T. Tanabe, Y. Nagai, H. Sobukawa, H. Shinjoh, M. Sugiura, C. Descorme, D. Duprez, Catal. Today 90 (2004) 223–229.
[22] T. Ozawa, J. Thermal Anal. 7 (1975) 601–617.
[23] S. G. Chen, R. T. Yang, F. Kapteijn, J. A. Moulijn, Ind. Eng. Chem. Res. 32 (1993) 2835–2840.
[24] X. Zhang, K. J. Klabunde, Inorg. Chem. 31 (1992) 1706–1709.
[25] X. Li, A. Vannice, J. Catal. 151 (1995)87–95.
[26] D. Bruce Losee, J. Catal. 50 (1977) 545–548.
[27] W. C. Conner, J. L. Falconer, Chem. Rev. 95 (1995) 759–788.
[28] J. F. C. Candau, W. C. Conner, J. Catal. 106 (1987) 378–385.
[29] J. M. Parera, E. M. Traffano, J. C. Musso, C. L. Pieck, Stud. Surf. Sci. Catal. 17 (1983) 101–108.
[30] E. Baumgarten, A. Schuck, Appl. Catal. 37 (1988) 247–257.
[31] L–T. Weng, B. Delmon, Appl. Catal. A 81 (1992) 141–213.
[32] Y. Morooka, Stud. Surf. Sci. Catal. 77 (1993) 95–103.
[33] C. Descorme, D. Duprez, Appl. Catal. A 202 (2000) 231–241.
[34] T. Tatsuma, S. Tachibana, A. Fujishima, J. Phys. Chem. B 105 (2001) 6987–6992.
[35] W. Kubo, T. Tatsuma, J. Am. Chem. Soc. 128 (2006) 16034–16035.
[36] L. Zeng, T. Turek, A. P. Weber, Chem. Ing. Tech. 83 (2011) 1276–1281.
[37] L. Zeng, A. P. Weber, Chem. Ing. Tech. 84 (2011) 295–300.
[38] F. Roessner, U. Mroczek, A. Hagen, Stud. Surf. Sci. Catal. 77 (1993) 151–158..

Chapter 7

Improved tolerance for ash deposition of catalyzed PM filter

Abstract

Oxidation behavior of particulate matter (PM) in catalyzed diesel particulate filters (CDPFs) was investigated in the presence of ash through small-scale catalytic performance evaluation and visualization measurement. In the absence of ash, a CeO_2–Ag CDPF reduces the PM oxidation temperature by approximately 100 °C when compared with a CDPF with a Pt/Al_2O_3 catalyst or a bare diesel particulate filter. The catalytic performance of the CeO_2–Ag CDPF decreases in the presence of ash. However, this decrease is observed until the ash reaches 40g/L in weight or 100 μm in thickness. An electron spin resonance analysis suggests that this remote PM oxidation is caused by the migration of superoxide species generated by the CeO_2–Ag catalyst.

Keywords; Particulate matter oxidation, Soot oxidation, Silver, Ceria, Catalyzed diesel particulate filter, Ash deposition, Remote oxidation

1. Introduction

The use of catalyzed diesel particulate filters (CDPFs) is regarded as the most promising method of reducing particulate matter (PM, mainly soot) emissions from diesel engines [1,2]. However, ash, which is generated primarily from lubricant oil, is deposited on the filter, where it forms a barrier between PM and filter's catalyst, often decreasing its catalytic performance. An innovative CeO_2–Ag catalyst was recently developed, which consists of Ag particles in the center surrounded by fine CeO_2 particles (Fig. 1). This catalyst exhibits exceptional catalytic performance in PM oxidation [3,4]. In addition, a visualization measurement system was developed; by this system, filtration and oxidation behavior of PM secondary particles in the diesel particulate filter (DPF) wall can be observed directly using actual diesel engine exhaust gas [5]. However, this system has not been utilized yet for the measurement for PM oxidation in ash-deposited CDPFs. In the present study, PM oxidation behavior in CDPFs with deposited ash is studied through small-scale catalytic performance evaluation and the recently proposed visualization measurement system.

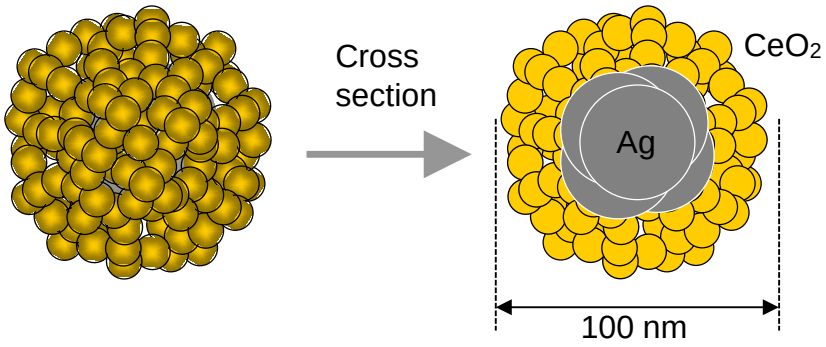

Fig. 1. Schematic of CeO_2–Ag catalyst [3,4].

2. Experimental

2.1. Catalyzed diesel particulate filter preparation

A CeO_2–Ag catalyst was prepared using a coprecipitation method by adding an aqueous solution of $AgNO_3$ and $Ce(NO_3)_3$ to an NH_3 solution [3,4]. The CeO_2–Ag CDPF was created by coating full-scale (2.0 L and 10.5 L) cordierite DPF substrates (porosity 65%, mean pore size 25 μm) with the obtained coprecipitate. The coating amount was CeO_2(46 g/L)–Ag(29 g/L). In addition, a Pt/Al_2O_3 CDPF was prepared by coating the same DPF substrates with an Al_2O_3 colloidal solution and impregnating with a $Pt(NO_2)_2(NH_3)_2$ solution. The coating amount was Pt(1.0 g/L)/Al_2O_3(60 g/L). Both CDPFs were aged at 650 °C for six hours in air and used for the two examinations as follows.

2.2. Small-scale catalytic performance evaluation

For the ash deposition treatment, ash was deposited on full-scale CDPFs from an engine bench system under two conditions with various lubricant-oil ash levels, fuel sulfur contents, and operating times (Table 1). During the ash deposition treatment PM trapped on the CDPFs was periodically removed by oxidation at high temperatures (620 °C, 640 °C). Small-scale CDPFs (35 mL) containing various amounts of deposited ash (1.5–65 g/L) were extracted from different locations in the full-scale CDPFs and plugged with a ceramic to be alternately used as filters. Simulated PM was generated using a combustion aerosol standard system (CAST) and fed to a CDPF with an airflow of 20 L/min. To investigate the influence of ash deposition on the filter's performance, PM was trapped on the ash-deposition side of the CDPF wall and on the opposite side from ash deposition. The amount of trapped PM was approximately 2.0 g/L. The catalytic performance in PM oxidation in small-scale CDPFs was evaluated through

temperature-programmed oxidation (TPO) at a heating rate of 20 °C/min in a gas flow containing 10% O_2 and 10% H_2O balanced with N_2 at 30 L/min after pretreatment at 500 °C for 15 min in a N_2 gas flow.

Table 1. Conditions of ash deposition treatment.

Condition	CDPF volume (L)	Lubricant-oil	Fuel sulfur content (ppm)	Treating temperature (°C)	Operating time (h)
Standard	10.5	Standard	5−7	500 − 620	500
Accelerating	3.0	High Ca content	50	350 − 640	76

2.3. Visualization measurement

Test pieces of 10 x 15 x 25 mm were cut from the above full-scale CDPFs, plugged with a ceramic to be used as a filter, and equipped with a glass window. A portion of the diesel engine's exhaust gas was led to a visualization measurement system's apparatus, where the pieces were placed (Fig. 2) [5]. An α-Al_2O_3 powder was used as simulated ash to replicate the impact of actual ash on the catalytic performance of a CDPF. The α-Al_2O_3 powder dispersed in air was added to the exhaust gas and led to the test pieces until a deposited ash layer reached a given thickness on the CDPF wall. Thereafter, PM in the exhaust gas from the diesel engine was trapped in the test pieces at 300 °C and oxidized at a given temperature in the exhaust gas flow, from which PM was previously removed using a DPF.

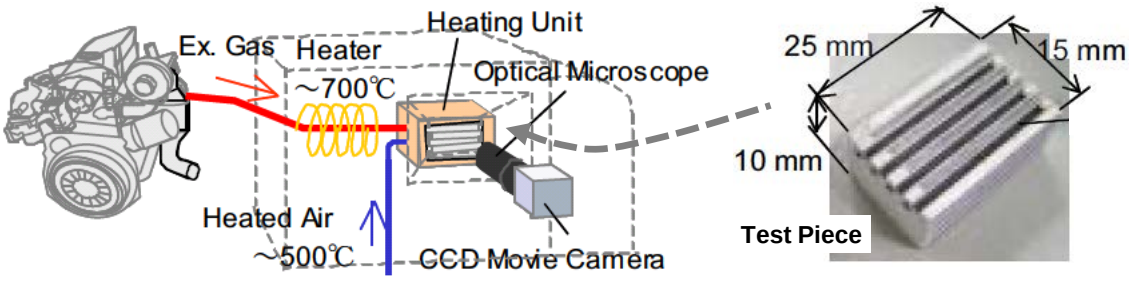

Fig.2. Visualization measurement system [5].

2.4. Electron spin resonance analysis

For electron spin resonance (ESR) analysis, 20 mg of a sample was placed in a 3.5-mm-diameter quartz ESR tube, which allowed the pretreatment and adsorption of various gases. In accordance with the previously proposed methodology [4], after the preadsorption of 20% O_2/N_2 at 600 °C for 30 min, the test sample was cooled to room temperature, purged with N_2 for 30 min, and finally exposed to a 3% H_2/N_2 flow at 30 mL/min for 3 min at 250 °C. The ESR spectrum was recorded at 20 K.

3. Results and discussion

3.1. PM oxidation in CDPF before ash deposition

Figure 3 presents TPO profiles of PM oxidation in CeO_2–Ag and Pt/Al_2O_3 CDPFs in the absence of ash deposition, as well as in a bare DPF. PM is oxidized in the CeO_2–Ag CDPF at lower temperatures than in the bare DPF. The temperature corresponding to 80% conversion of trapped PM (T_{80}; 80% PM oxidation temperature), which is derived from the TPO profile, is used as a catalytic performance measure. Lower T_{80} values indicate higher catalytic performance. The CeO_2–Ag CDPF (560 °C) decreases T_{80} by approximately 110 °C when compared with the bare DPF (665 °C). On the contrary, the Pt/Al_2O_3 CDPF exhibits almost the same T_{80} (660 °C) as the bare DPF.

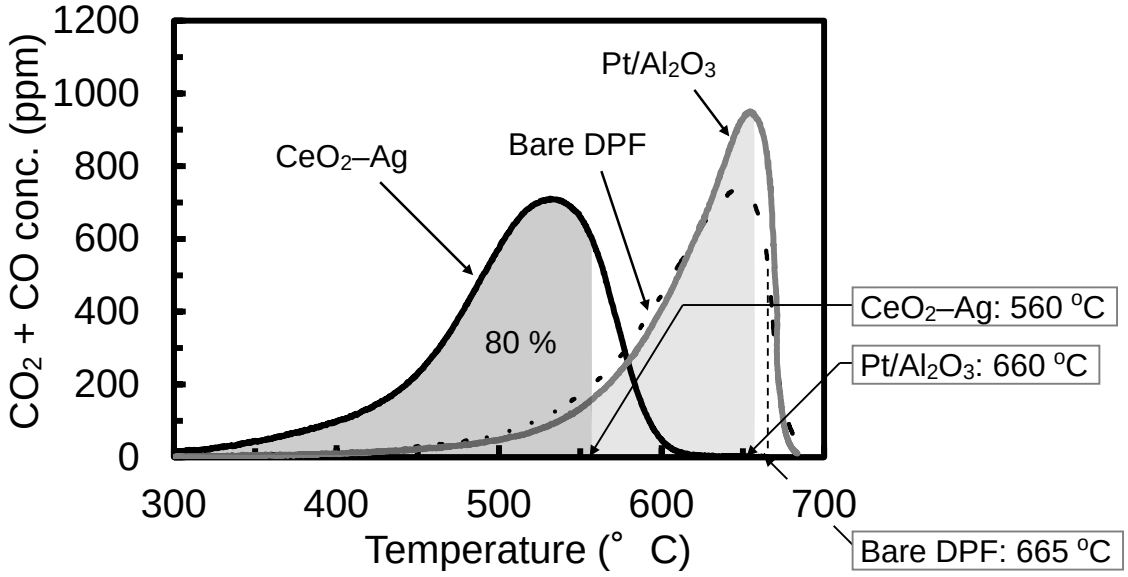

Fig. 3. PM oxidation behavior in CDPFs.

3.2. PM oxidation in CDPF after ash deposition

Figure 4 presents a TPO profile of PM oxidation in the CeO_2–Ag CDPF containing 13 g/L actual deposited ash (black line). PM is oxidized in this CDPF at lower temperatures than in the bare DPF. This result demonstrates that the CeO_2–Ag CDPF exhibits high catalytic performance even when a certain amount of ash is deposited on the catalyst. Figure 4 also shows a TPO profile of PM oxidation in the CeO_2–Ag CDPF, on which PM is trapped on the opposite side of ash deposition (gray line), as well as on the same side (black line). The difference between these two TPO profiles reflects the influence of ash deposition because there is no difference in the filter's catalytic performance between the two sides. Using several CeO_2–Ag CDPFs, a relation between the amount of ash deposited and catalytic performance (T_{80}) is obtained (Fig. 5). When PM is trapped on the opposite side of ash deposition, the T_{80} value remains almost constant, regardless of the amount of ash deposited. Thus, when PM is trapped on the ash-deposition side, an increase in the T_{80} value corresponds to the difference between the catalyst and PM by ash deposition. The catalytic performance of the CeO_2–Ag CDPF decreases in the presence of ash. However, this decrease is observed until ash deposition reaches 40 g/L. Over this threshold, the T_{80} value remains constant and almost equal to the value for the bare DPF. Therefore, it is concluded that the CeO_2–Ag CDPF sufficiently catalyzes the PM oxidation reaction as long as the deposited ash does not exceed 40 g/L in weight.

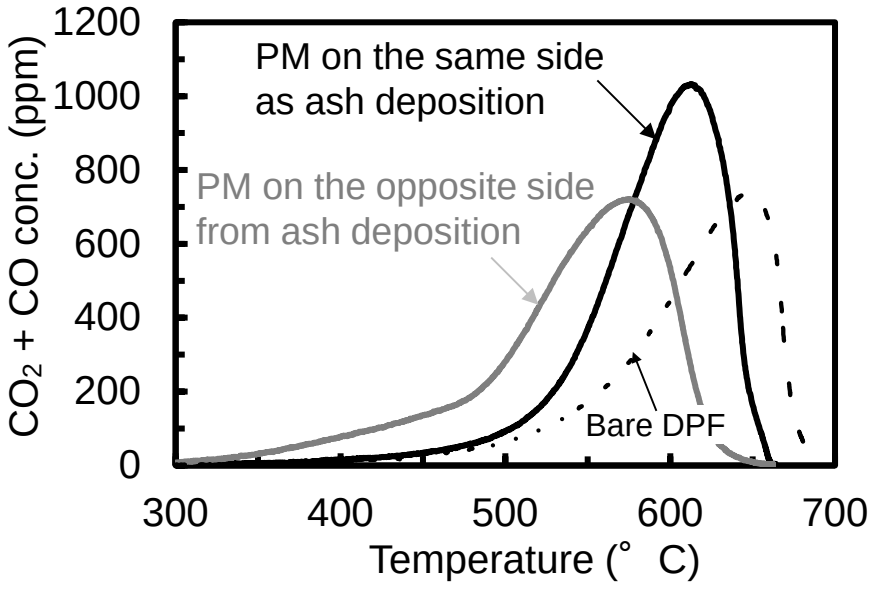

Fig. 4. PM oxidation behavior in CeO_2–Ag CDPFs after ash deposition.

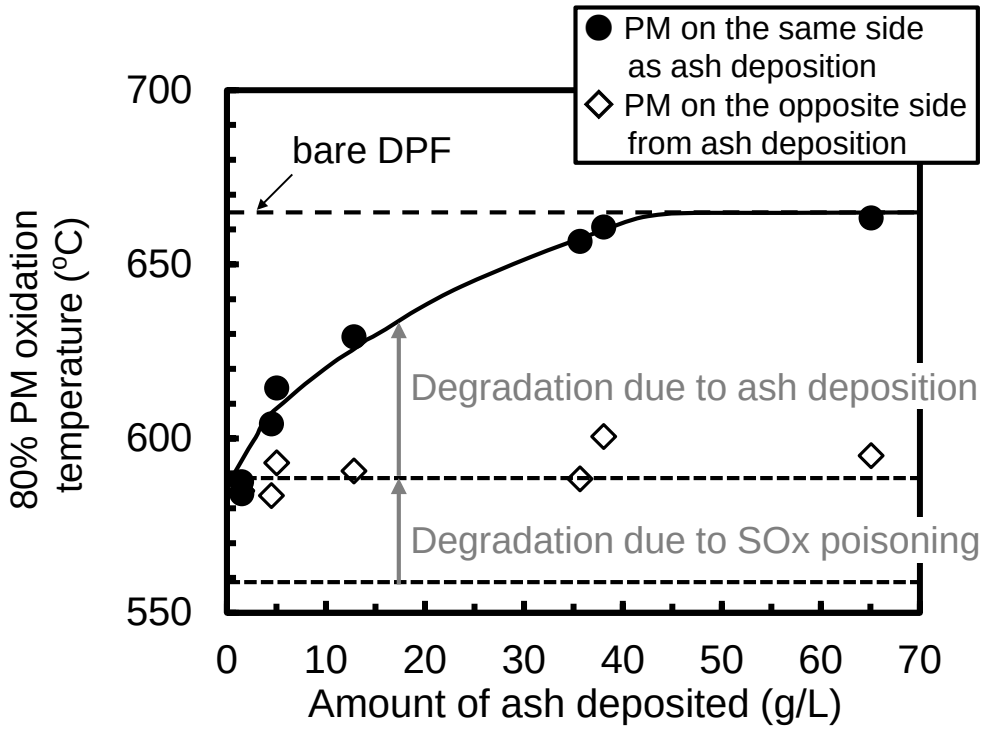

Fig. 5. Catalytic performance for PM oxidation in CeO_2–Ag CDPFs after ash deposition.

The T_{80} value of PM trapped on the opposite side of ash deposition (approximately 590 °C) is slightly greater than that before ash deposition using the engine bench system (560 °C). This decrease in catalytic performance is probably a result of sulfur poisoning originating from the diesel fuel's sulfur content and is almost constant, regardless of the amount of ash deposited, and much lower than the decrease due to ash deposition.

3.3. Visualization of PM oxidation process

A visualization measurement system directly displays PM oxidation behavior in a CeO_2–Ag CDPF after ash deposition (Fig. 6). A CDPF wall containing the CeO_2–Ag catalyst (gray), an ash layer (white), and a PM-trapped layer (black) are clearly discerned. After a certain time interval while a portion of the diesel exhaust gas, from which PM was previously removed using a DPF, is led to the test pieces at 630 °C, the thickness of the PM-trapped layer appears to be reduced, whereas that of the ash layer remains unchanged. If the ash layer and PM-trapped layer have equal thicknesses on the test pieces' DPF walls and PM bulk density is even, then the PM oxidation rate is the decreasing rate of the PM-trapped-layer's thickness. In the present study, PM oxidation

rates were determined at several observation points with different ash-layer thicknesses from a photographic image at a given temperature. As an example, Fig. 6 presents PM oxidation rates on the ash layer in the range of 50–100 μm at multiple observation points. Similarly, PM oxidation rates on the ash layer in other ranges (below 50 μm and above 100 μm) were obtained from other images.

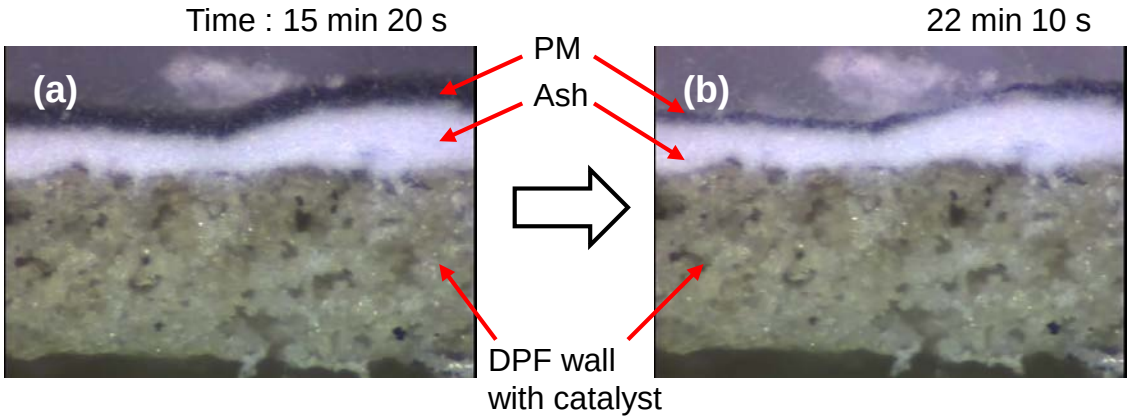

Fig. 6. PM oxidation process in CDPFs in the presence of ash deposition at (a) 15 min 20s and (b) 22 min 10 s after feeding a portion of the diesel exhaust gas at 630 ^{o}C.

Figure 7 presents the relation between the PM oxidation rate and ash-layer's thickness in the CeO_2–Ag and Pt/Al_2O_3 CDPFs at 630 °C, 550 °C, and 500 °C. Under all conditions, the PM oxidation rate in CeO_2–Ag CDPF is equal to or greater than that in the Pt/Al_2O_3 CDPF. Especially at 630 °C, the PM oxidation rate in CeO_2–Ag CDPF is approximately twice that in the Pt/Al_2O_3 CDPF when the thickness of the ash layer is below 50 μm.

The PM oxidation rate in the CeO_2–Ag CDPF decreases until the thickness of the ash layer reaches approximately 100 μm and becomes constant when the thickness exceeds 100 μm at 630 °C. This result indicates that the CeO_2–Ag CDPF promotes PM oxidation on the ash layer until that point. On the contrary, the Pt/Al_2O_3 CDPF promotes PM oxidation until the thickness of the ash layer reaches approximately 50 μm at the same temperature. Therefore, the catalytic performance of the CeO_2–Ag CDPF extends twice as much as that of the Pt/Al_2O_3 CDPF at 630 °C. The CeO_2–Ag CDPF promotes PM oxidation on the ash layer until its thickness reaches 30 μm at 550 °C and 500 °C, whereas the Pt/Al_2O_3 CDPF promotes PM oxidation on the ash

layer until its thickness reaches 20 μm at 550°C, but not at 500°C. Higher temperatures improve the filter's catalytic performance with ash deposition.

Using full-scale CeO_2–Ag and Pt/Al_2O_3 CDPFs, on which actual ash was deposited from an engine bench system for the small-scale catalytic performance evaluation (section 2.2), reveals a correlation between the amount of ash deposited and thickness of the ash layer, regardless of engine operating conditions (Fig. 8). For example, 40 g/L deposited ash corresponds to 100 μm layer thickness. This suggests that the extent of the catalytic performance of the CeO_2–Ag CDPF estimated through the small-scale evaluation approach is in accordance with the visualization measurement system's assessments. As a result, the CeO_2–Ag CDPF allows the remote oxidation of PM separated by an ash layer that is under 40g/L in weight or 100 μm in thickness.

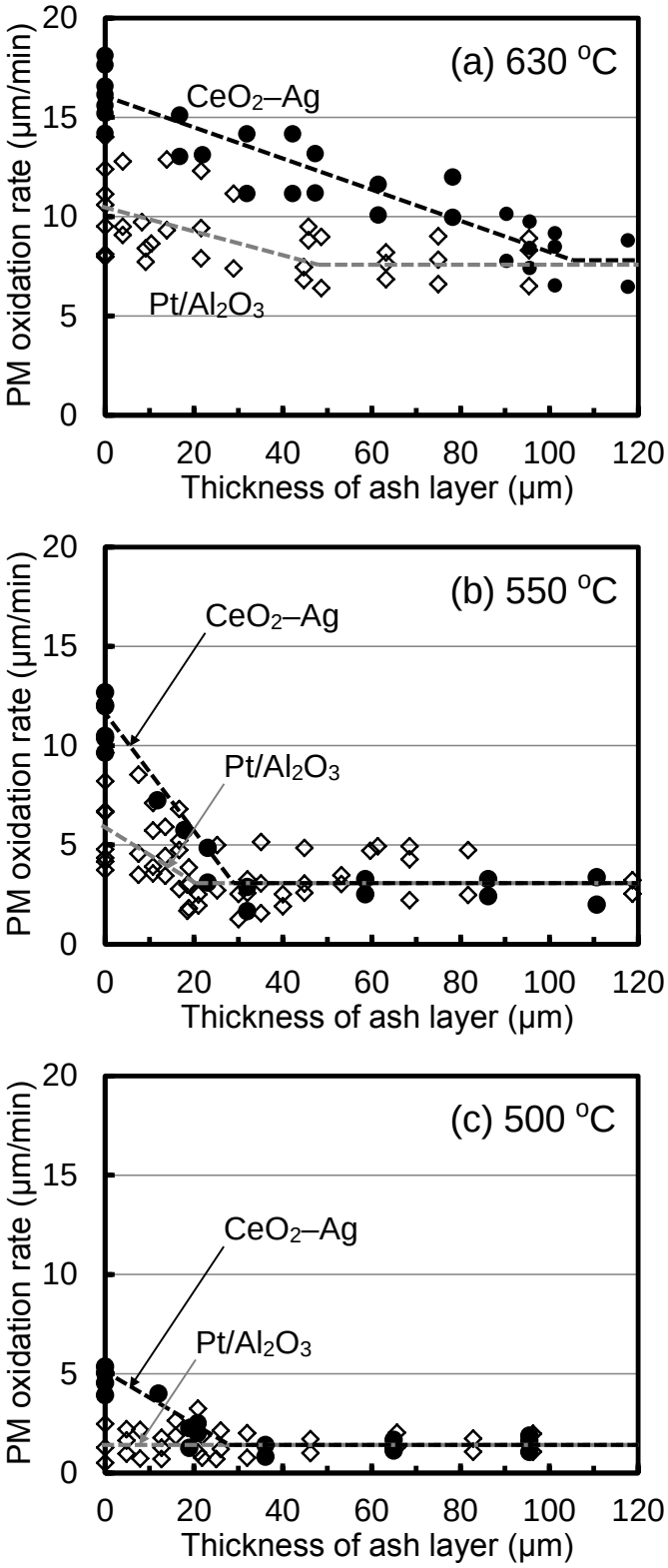

Fig. 7. PM oxidation rates in CDPFs after ash deposition.

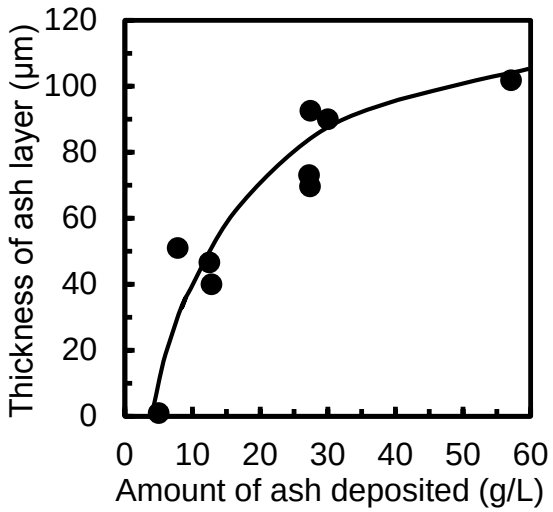

Fig. 8. Amount of ash deposited and ash-layer thickness.

3.4. PM oxidation mechanism

The present small-scale evaluation and visualization measurement results reveal that the PM oxidation reaction is catalyzed in CeO_2–Ag CDPFs even in the presence of ash. However, catalytic PM oxidation with gaseous O_2 is, basically, a solid-catalyzed gas–solid reaction. In this reaction, contact between the catalyst and PM is necessary because reaction processes occur at a three-phase boundary between the two solids (catalyst and PM) and gaseous O_2. Hence, the presented observations here cannot be readily explained. The five explanations that are hypothesized and examined are as follows.

(1) PM passes through the ash layer onto the catalyst, where it is oxidized.
(2) The ash-layer thickness on the CDPF wall is not even. Consequently, a portion of the catalyst's surface is exposed. PM migrates over the catalyst's surface and is oxidized there.
(3) Soluble organic fraction (SOF) in the PM vaporizes and is oxidized on the catalyst's surface, resulting in a local temperature increase, which further promotes PM oxidation.
(4) CO formed through non-catalyzed PM oxidation [6] at temperatures over approximately 450 °C (Fig. 1) is oxidized on the catalyst's surface, resulting in a local temperature increase, which promotes PM oxidation.

(5) An active oxygen species that is generated on the catalyst's surface migrates onto the ash layer, then onto PM, and oxidizes PM.

Regarding hypothesis (1), a very small amount of PM penetrating the ash layer is actually observed and quantified through a scanning electron microscopy/energy-dispersive X-ray spectroscopy (SEM/EDX) analysis. Even if this PM quantity migrates on the CDPF wall during the visualization measurement at the same speed as gas flow (1.47 cm/min), the decreasing rate of the PM-trapped-layer's thickness corresponds to 0.023 μm/min; this value is exponentially lower than that presented in Fig. 7. Therefore, PM passing through the ash layer does not contribute to PM oxidation.

As for hypothesis (2), it was directly confirmed that the deposited ash layer covered the catalyst's surface thoroughly in the test pieces for the visualization measurement system, at least when the maximum thickness of the ash layer exceeds 10 μm. Then, hypothesis (2) is not supported in the case of the ash layer over 10 μm.

After SOF is vaporized through a pretreatment at 500 °C for 15 min in a N_2 gas flow during the small-scale evaluation procedure, the CeO_2–Ag CDPF with deposited ash exhibits high catalytic performance for PM oxidation. Thus, hypothesis (3) is not supported for the CeO_2–Ag CDPF. On the other hand, the Pt/Al_2O_3 CDPF with deposited ash presents high catalytic performance only through visualization using actual PM that contains SOF. This result suggests that hypothesis (3) can be applied only to the Pt/Al_2O_3 CDPF.

As for hypothesis (4), the catalytic performance for CO oxidation over the CeO_2–Ag CDPF was almost equal or lower compared to that for the Pt/Al_2O_3 CDPF at temperatures over approximately 450 °C, resulting in an equal or less local temperature increase. On the contrary, the catalytic performance for PM oxidation over the CeO_2–Ag CDPF is higher, then hypothesis (4) is not supported for the increased catalytic performance for PM oxidation over the CeO_2–Ag CDPF compared to the Pt/Al_2O_3 CDPF. Therefore, although the catalytic performance of the Pt/Al_2O_3 CDPF with ash may be explained by hypotheses (3) or (4), the performance of the CeO_2–Ag CDPF with ash must be attributed to another scenario, possibly that corresponding to hypothesis (5).

Zeng et al. recently reported a platinum catalyst with catalytic performance for the oxidation of soot separated by an inert SiO_2 layer [7,8]. Their study indicated that soot is catalytically oxidized only when the gas (20% O_2/N_2) flows through layers in the sequence as follows: catalyst, SiO_2, and soot. However, it is not oxidized in the reverse

sequence. Furthermore, they tentatively proposed a transport mechanism for activated oxygen through the gas phase. However, this is considerably different from actual working conditions of PM oxidation in a CDPF with deposited ash. In addition, in the above examinations, the CeO_2–Ag CDPF exhibits catalytic performance for PM oxidation independent of ash deposition even when the gas flows through layers in the sequence as follows: PM, ash, and catalyst. This phenomenon indicates that active oxygen species generated on the catalyst migrates in the reverse direction from the gas flow. Roessner et al. reported that adsorbed hydrogen species on a Pt/Al_2O_3 surface can migrate (spillover) to a H-ZSM-5 surface contrary to the flow direction in an isomerization reaction of cyclohexane [9]. Therefore, it is very likely that the catalytic performance for PM oxidation in the CeO_2–Ag CDPF with ash is attributed to the adsorbed active oxygen species, which can diffuse (spillover) on the surface of the catalyst and ash, instead of the activated gaseous oxygen.

Using oxygen-temperature-programmed desorption and ESR, we found previously that the oxygen species adsorbed on the Ag surface under oxidative conditions is transformed into superoxide (O_2^-) on the CeO_2 surface under weak reductive conditions and that the increased O_2^- formation leads to a higher catalytic performance for PM oxidation in the CeO_2–Ag catalyst [4]. Based on this mechanism for PM oxidation, the adsorbed O_2^- species is expected to contribute to the reaction in the CeO_2–Ag CDPF with deposited ash. ESR analysis was implemented to explore the role of the O_2^- species in this phenomenon. The CDPF samples for the small-scale evaluation and visualization measurement could not be directly analyzed by ESR because of their sizes. Thus, a mixture of a pelletized CeO_2–Ag catalyst and a pelletized simulated ash (α-Al_2O_3) (Table 2) was used instead to simulate the CeO_2–Ag CDPF with deposited ash. To prepare this sample, the catalyst and ash powders were first separately pressed into pellets 180-210 μm in diameter, then combined in a weight ratio of 1:1, mixed by shaking in a bottle and finally pressed together into pellets 710-1000 μm in diameter. The obtained sample incorporated an interface between the catalyst and the ash, with each continuous portion at a distance of about 100μm from the interface. In agreement with a previous report [4], the ESR spectrum was recorded after exposure to an oxidative atmosphere, followed by a weak reductive atmosphere. The obtained results are compared with those produced for pure, unmixed samples. Table 1 presents the ESR signals, the identified species, and the spin density values. The spin density value was obtained per unit weight of the catalyst for O_2^- on CeO_2 surface or per unit weight of the simulated ash for O_2^- on Al_2O_3 surface. A certain amount of O_2^- is formed on the CeO_2 surface ($g_1 = 2.041$ and $g_2 = g_3 = 2.010$) of the pure CeO_2–Ag catalyst. It is also

formed in a mixture of CeO_2–Ag and ash. However, the O_2^- amount is approximately 25% that of the pure CeO_2–Ag sample. A small amount of O_2^- is formed on the Al_2O_3 surface (g = 2.080) in the case of the pure simulated ash. The O_2^- species on the Al_2O_3 surface is formed in the mixture of CeO_2–Ag and ash, and its amount exceeds (approximately 60% greater) that of pure ash. These results strongly suggest that the O_2^- species formed on the catalyst's surface migrates onto the ash surface through their interface at contact (Fig. 9). Therefore, a new mechanism for PM oxidation in the CeO_2–Ag CDPF with deposited ash is proposed. The O_2^- species generated on the CeO_2–Ag catalyst first migrates (surface diffusion) to the ash surface, then to PM, and oxidizes PM, regardless of the gas-flow direction.

Table 2. ESR signals, identified species, and spin density values.

Sample		ESR signals	Species	Spin density (μmol/g)
CeO_2–Ag catalyst	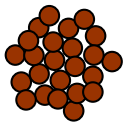	g_1= 2.041 g_2= g_3= 2.010	O_2^- on CeO_2	0.830
Ash (α-Al_2O_3)	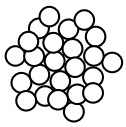	g= 2.080	O_2^- on Al_2O_3	0.050
Mixture of CeO_2–Ag and ash	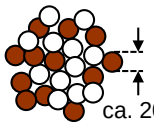	g_1= 2.041 g_2= g_3= 2.010 g= 2.080	O_2^- on CeO_2 O_2^- on Al_2O_3	0.217 0.080

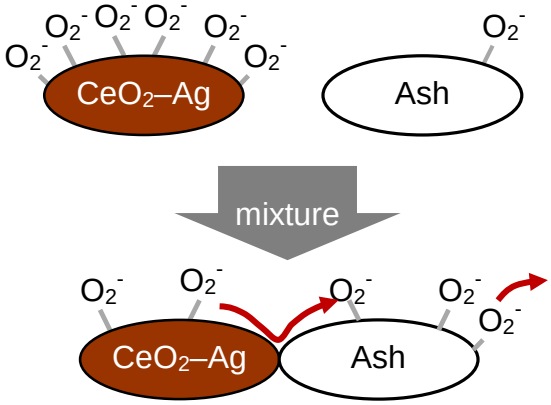

Fig. 9. O_2^- species migration on the catalyst to the ash surface.

4. Conclusion

PM oxidation in CDPFs with deposited ash is investigated through small-scale performance evaluation and visualization measurement. In addition, the results of an ESR analysis are used to provide a new mechanism to explain this behavior.

In the absence of ash, a CeO_2–Ag CDPF reduces the 80% PM-trapped conversion temperature by approximately 100 °C when compared with a bare DPF or a Pt/Al_2O_3 CDPF. The catalytic performance of the CeO_2–Ag CDPF diminishes when ash is deposited but only until the amount of deposited ash reaches 40g/L. The visualization measurement directly shows that the CeO_2–Ag CDPF promotes the oxidation of PM on the ash layer up to approximately 100 μm of ash-layer thickness at 630 °C. Therefore, the CeO_2–Ag CDPF enables the remote oxidation of PM, which is separated by an ash layer of under 40g/L in weight or 100 μm in thickness. On the other hand, the Pt/Al_2O_3 CDPF promotes PM oxidation up to a threshold of 50 μm in ash thickness, half of that for the CeO_2–Ag CDPF. The increased activity of the CeO_2–Ag CDPF compared to the Pt/Al_2O_3 CDPF increases its threshold tolerance to ash deposition at lower temperatures.

The results of the ESR analysis indicate that the amount of O_2^- species in the CeO_2–Ag catalyst decreases significantly after contact with the ash. In addition, a small amount of O_2^- species on ash increases after contact with the CeO_2–Ag catalyst, suggesting the migration of O_2^- species from the CeO_2–Ag catalyst to ash. Therefore, a mechanism for remote PM oxidation by the CeO_2–Ag catalyst is proposed, in which the O_2^- species generated on the catalyst's surface first migrates to the ash surface and then to the PM to oxidize PM.

The catalytic performance for remote PM oxidation in the CeO_2–Ag catalyst demonstrates its significant tolerance for ash deposition and its great potential for incorporation into future clean diesel-powered vehicles.

References

[1] B. A. A. L. van Setten, M. Makkee, J. A. Moulijn, Catal. Rev. 43 (2001) 489.
[2] T. V. Johnson, SAE technical paper 2008-01-0069 (2008).
[3] T. Kayama, K. Yamazaki, H. Shinjoh. J. Am. Chem. Soc. 132 (2010) 13154.
[4] K. Yamazaki, T. Kayama, F. Dong, H. Shinjoh, J. Catal. 282 (2011) 289.
[5] S. Daido, N. Takagi, SAE paper 2009-01-1473 (2009).
[6] S. G. Chen, R. T. Yang, F. Kapteijn, J. A. Moulijn, Ind. Eng. Chem. Res. 32 (1993) 2835.
[7] L. Zeng, T. Turek, A. P. Weber, Chem. Ing. Tech. 83 (2011)1276.
[8] L. Zeng, A. P. Weber, Chem. Ing. Tech. 84 (2011) 295.
[9] F. Roessner, U. Mroczek, A. Hagen, Stud. Surf. Sci. Catal. 77 (1993) 151.

Chapter 8

Summary and general conclusion

1. Summary of each chapter

Chapter 2: Improved resistance to sulfur poisoning of NO_x storage-reduction catalyst

The NO_x storage-reduction catalysis under oxidizing conditions in the presence of SO_2 has been investigated on Pt/Ba/Fe/Al_2O_3, Pt/Ba/Co/Al_2O_3, Pt/Ba/Ni/Al_2O_3 and Pt/Ba/Cu/Al_2O_3 catalysts compared with Pt/Ba/Al_2O_3 catalyst. The NO_x purification activity of Pt/Ba/Fe/Al_2O_3 catalyst was the highest of all the catalysts after an aging treatment. That of the aged Pt/Ba/Co/Al_2O_3 and Pt/Ba/Ni/Al_2O_3 catalysts was essentially the same as that of the aged Pt/Ba/Al_2O_3 catalyst, while that of the aged Pt/Ba/Cu/Al_2O_3 catalyst was substantially lower than the others.

The Fe-compound on the aged Pt/Ba/Fe/Al_2O_3 catalyst has played a role in decreasing the sulfur content on the catalyst after exposure to simulated reducing gas compared with the Pt/Ba/Al_2O_3 catalyst without the Fe-compound. XRD and EDX show that the Fe-compound inhibits the growth in the size of $BaSO_4$ particles formed on the Pt/Ba/Fe/Al_2O_3 catalyst under oxidizing conditions in the presence of SO_2 and promotes the decomposition of $BaSO_4$ and desorption of the sulfur compound under reducing conditions.

Chapter 3: Improved thermal durability of NO_x storage-reduction catalyst

The NO_x purification activity through storage-reduction (NSR activity) over a Pt/Ba/(Al_2O_3-CeO_2-Fe_2O_3) catalyst was investigated in comparison with a Pt/Ba/(Al_2O_3-CeO_2) catalyst. Two kinds of reducing agents, C_3H_6 and CO, were used for the measurement of the NSR activity. There was no difference in the NSR activity between these two fresh catalysts. After thermal aging at 1123 K, however, the aged Pt/Ba/(Al_2O_3-CeO_2-Fe_2O_3) catalyst was found to show a higher NSR activity in the case of using CO as a reducing agent than did the aged Pt/Ba/(Al_2O_3-CeO_2) catalyst, although there was no difference in the NSR activity in the case of using C_3H_6 as a reducing agent between these two aged catalysts. Reaction analysis of a simple binary gas system showed that the Fe-compound weakened the CO self-poisoning for the CO-O_2 reaction and the CO-NO_x reaction under reducing conditions, probably by provision of oxygen to the CO from Fe_2O_3 or/and Fe in a Pt-Fe alloy. The weaker CO self-poisoning for the CO-NO_x reaction leads to a greater ability to reduce stored NO_x

on the catalysts by CO under reducing conditions, causing a higher NSR activity in the case of using CO as a reducing agent after thermal aging.

Chapter 4: Improved three-way catalytic performance of NO_x storage-reduction catalyst

The three-way catalytic (TWC) performance of NO_x storage-reduction catalyst (NSR catalyst) was investigated over a Pt/Ba/(Al_2O_3-CeO_2-Fe_2O_3) catalyst and compared with a Pt/Ba/(Al_2O_3-CeO_2) catalyst. For fresh catalysts, the TWC performances of these catalysts were almost equal. However, after thermal aging at 1123K, the TWC performance of the aged former catalyst was higher than that of the aged latter one.

X-ray diffraction measurements showed that there is no difference in the Pt and CeO_2 particle size between the aged Pt/Ba/(Al_2O_3-CeO_2-Fe_2O_3) catalyst and aged Pt/Ba/(Al_2O_3-CeO_2) catalyst. However, the thermogravimetric analysis showed that the oxygen storage-release capacity (OSC) of the aged former catalyst was far greater than that of the aged latter one. Therefore, the Fe-compound on a Pt/Ba/(Al_2O_3-CeO_2-Fe_2O_3) catalyst has been proved to increase the OSC of the aged catalyst, resulting in high TWC performance after thermal aging.

Chapter 5: Improved catalytic performance for PM oxidation in loose contact mode

A CeO_2–Ag catalyst with a 'rice-ball' morphology, consisting of Ag particles in the center surrounded by fine CeO_2 particles, exhibits exceptional catalytic performance for soot oxidation by O_2 below 300 °C. The reaction mechanism over this catalyst were studied by O_2 temperature-programmed desorption (O_2-TPD), $^{18}O/^{16}O$ isotopic exchange (IE) reaction and electron spin resonance (ESR) techniques. It is speculated that adsorbed oxygen species on the Ag surface migrate to the CeO_2 surface via the Ag/CeO_2 interface to form O_n^{x-} species (at least partly O_2^-) and further migrate onto the soot particles. Due to morphological compatibility of the moderately large Ag particles (ca. 30–40 nm) and the extremely large interfacial area with the CeO_2 particles, the formation and migration rates of the oxygen species on the CeO_2–Ag catalyst are efficiently promoted, resulting in its distinguished catalytic performance and relative insensitivity to the contact mode of the soot-catalyst mixture.

Chapter 6: Remote oxidation of PM separated by ash deposition via PM oxidation catalyst

One of the main issues of catalyzed diesel particulate filter is ash deposition onto

catalyst coated on the filter. The effects of ash deposition on the catalysis of soot oxidation with gaseous oxygen were determined using multi-layered samples composed of a catalyst, an ash material and soot particles deposited on a thin cordierite plate in sequence. Catalysts composed of silver and ceria were used to enhance the oxidation of soot particles separated from the catalyst by ash deposits of either alumina or calcium sulfate. The effectiveness of remote soot oxidation was found to extend across an ash thickness of more than 50 μm for both ash materials, although a catalyst composed only of ceria did not show any catalytic performance for remote soot oxidation. Using an $^{18}O/^{16}O$ isotopic exchange reaction and electron spin resonance techniques, a possible mechanism for this phenomenon was proposed, whereby a superoxide ion (O_2^-) species generated on the catalyst surface first migrates to the ash surface and then to the soot particles, which it subsequently oxidizes.

Chapter 7: Improved tolerance for ash deposition of catalyzed PM filter

Oxidation behavior of particulate matter (PM) in catalyzed diesel particulate filters (CDPFs) was investigated in the presence of ash through small-scale catalytic performance evaluation and visualization measurement. In the absence of ash, a CeO_2–Ag CDPF reduces the PM oxidation temperature by approximately 100 °C when compared with a CDPF with a Pt/Al_2O_3 catalyst or a bare diesel particulate filter. The catalytic performance of the CeO_2–Ag CDPF decreases in the presence of ash. However, this decrease is observed until the ash reaches 40g/L in weight or 100 μm in thickness. An electron spin resonance analysis suggests that this remote PM oxidation is caused by the migration of superoxide species generated by the CeO_2–Ag catalyst.

2. General Conclusion

- The addition of an Fe_2O_3 to a NO_x storage-reduction (NSR) catalyst improved its NO_x removal activity after sulfur poisoning.
- The addition of an Fe_2O_3 to a NSR catalyst also improved its NO_x removal activity when using CO as a reducing agent and its three-way catalytic performance after thermal aging.
- The Fe_2O_3 in the NSR catalysts played important roles; (1) suppressing a poisoning of reductant (HC, CO) and/or sulfur-compounds onto Pt surface during desulfation treatment, resulting in improved resistance to sulfur poisoning, and (2) suppressing a CO-poisoning during reduction of stored NO_x, resulting in improved thermal durability.
- An innovative CeO_2–Ag catalyst with a unique morphology exhibited an outstanding performance for PM oxidation with gaseous O_2 even in loose contact mode and a high insensitivity to the contact with PM.
- The CeO_2–Ag catalyst in catalyzed particulate filters promoted the oxidation of PM separated by an ash deposited layer of under 40 g/L in weight or 100μm in thickness. This phenomenon demonstrates the remote PM oxidation via catalyst.
- O_2-TPD, $^{18}O/^{16}O$ isotopic exchange reaction analysis and ESR data suggested that mobile activated oxygen species (mainly O_2^- species) generated on the CeO_2–Ag catalyst played important roles; (1) creating contact between PM and catalyst and (2) migration onto ash surface and further onto PM particles to oxidize them.

List of publications

Chapter 2: Improved resistance to sulfur poisoning of NOx storage-reduction catalyst

[1] Effect of the addition of transition metals to Pt/Ba/Al_2O_3 catalyst on the NO_x storage-reduction catalysis under oxidizing conditions in the presence of SO_2. K. Yamazaki, T. Suzuki, N. Takahashi, K. Yokota, M. Sugiura, Applied Catalysis B: Environmental 30 (2001) 459–468.

Chapter 3: Improved thermal durability of NOx storage-reduction catalyst

[2] The performance of NO_x storage-reduction catalyst containing Fe-compound after thermal aging. K. Yamazaki, N. Takahashi, H. Shinjoh, M. Sugiura, Applied Catalysis B: Environmental 53 (2004) 1–12.

Chapter 4: Improved three-way catalytic performance of NOx storage-reduction catalyst

[3] Three-way catalytic performance of NOx storage-reduction catalyst containing Fe-compound after thermal aging. K. Yamazaki, N. Takahashi, H. Shinjoh, M. Sugiura, Advances in Technology of Materials and Materials Processing Journal 4 (2002) 80–83.

Chapter 5: Improved catalytic performance for PM oxidation in loose contact mode

[4] A mechanistic study on soot oxidation over CeO_2–Ag catalyst with ‘rice-ball’ morphology. K. Yamazaki, T. Kayama, F. Dong, Hirofumi Shinjoh, Journal of Catalysis 282 (2011) 289–298.

Chapter 6: Remote oxidation of PM separated by ash deposition via PM oxidation catalyst

[5] The remote oxidation of soot separated by ash deposits via silver–ceria composite catalysts. K. Yamazaki, Y. Sakakibara, F. Dong, Hirofumi Shinjoh, Applied Catalysis A: General 476 (2014) 113–120.

Chapter 7: Improved tolerance for ash deposition of catalyzed PM filte

[6] アッシュ堆積時における触媒付ディーゼル微粒子捕集フィルター上の PM 酸化挙動解析, 山崎清, 榊原雄二, 大道重樹, 大河原誠治, 自動車技術会論文集 vol.46 (2015 年) p.65–70.

[7] Particulate matter oxidation over ash-deposited catalyzed diesel particulate filters. K. Yamazaki, Y. Sakakibara, S. Daido, S. Okawara, Topics in Catalysis 59 (2016) 1076–1082.